

# Tracing the Reionization-Epoch Intergalactic Medium with Metal Absorption Lines

Benjamin D. Oppenheimer<sup>1</sup>, Romeel Davé<sup>1</sup>, Kristian Finlator<sup>1</sup>

<sup>1</sup>*Astronomy Department, University of Arizona, Tucson, AZ 85721*

28 May 2018

## ABSTRACT

Intergalactic medium (IGM) metal absorption lines observed in  $z \gtrsim 6$  spectra offer the opportunity to probe early feedback processes, the nature of enriching sources, and the topology of reionization. We run high-resolution cosmological simulations including galactic outflows to study the observability and physical properties of 5 ions (C II, C IV, O I, Si II, Si IV) in absorption between  $z = 8 \rightarrow 5$ . We apply three cases for ionization conditions: Fully neutral, fully reionized, and a patchy model based on the flux from the nearest galaxy. We find that our simulations can broadly fit available  $z \sim 5 - 6$  IGM metal-line data, although all observations cannot be accommodated with a single ionization condition. Variations in O I absorbers among sight lines seen by Becker et al. (2006) suggest significant neutral IGM patches down to  $z \sim 6$ . Strong C IV absorbers at  $z \sim 6$  may be the result of ionization by the galaxy responsible for that enrichment, although the identification of the neighboring galaxy will have to wait to confirm this. Our outflows have typical speeds of  $\sim 200$  km/s and mass loading factors of  $\sim 6$ . Such high mass loading is critical for enriching the IGM to the observed levels while sufficiently curtailing early star formation to match the observed rest-frame UV luminosity function. The volume filling factor of metals increases during this epoch, but only reaches  $\sim 1\%$  for  $Z > 10^{-3} Z_{\odot}$  by  $z = 5$ . Detectable absorbers generally trace inhomogeneously-distributed metals residing outside of galactic halos. C IV is an ideal tracer of IGM metals at  $z \sim 5 - 6$ , with dropping global ionization fractions to either higher or lower redshifts. This results in a strongly increasing global C IV mass density ( $\Omega(\text{C IV})$ ) from  $z = 8 \rightarrow 5$ , in contrast to its relative constancy from  $z = 5 \rightarrow 2$ . Our simulations do not support widespread early IGM enrichment from e.g. Population III stars, as this would overpredict the numbers of weak C IV absorbers in the latest data. High- $z$  absorbers arise from metals mostly on their first outward journey, at distances 5-50 physical kpc, and often exhibit broad profiles ( $\delta v > 200$  km s<sup>-1</sup>) as a result of outflowing peculiar velocities in the strongest systems. The galaxies responsible for early IGM enrichment have typical stellar masses of  $10^{7.0-8.5} M_{\odot}$ , and star formation rates  $\lesssim 1 M_{\odot}/\text{yr}$ . Future facilities will be able to study the high- $z$  galaxy-absorber connection in detail, revealing a wealth of information about feedback processes in the reionization epoch.

**Key words:** intergalactic medium, galaxies: formation, galaxies: high-redshift, early Universe, cosmology: theory, methods: numerical

## 1 INTRODUCTION

The Universe undergoes its last major transition at  $z \sim 6$  as the first stars and early galaxies finish the process of reionizing the previously neutral intergalactic medium (IGM). Observations have only recently cracked the  $< 1$  Gyr Universe with the discovery of galaxies tracing early star formation (Bunker et al. 2004; Dickinson et al. 2004; Yan & Windhorst 2004; Bouwens et al. 2006), quasars pro-

viding ionizing photons (Fan et al. 2001, 2003), and the complete absorption by the IGM of all Lyman- $\alpha$  photons, i.e. the Gunn & Peterson (1965) trough, in  $z > 6$  quasar spectra (Fan et al. 2002).

A new type of high- $z$  observation is the recent detection of metal-line absorbers in the most distant quasar spectra, probing the nucleosynthetic products of early star formation. Becker et al. (2006, hereafter BSRS) surveyed 9  $z > 5.5$  quasars and found 4 O I systems in the most distant ob-

ject in their sample, J1148+5251. Ryan-Weber et al. (2006), Simcoe (2006), & Ryan-Weber et al. (2009) discovered multiple C IV absorbers at similar redshifts ( $z \sim 6$ ). Despite the metals presumably being formed within galaxies, these absorbers are most readily explained as arising in the diffuse IGM. But such absorbers are rare and perhaps highly inhomogeneous: For instance, Becker et al. (2009) finds no C IV along four lines of sight (LOSs) observed at higher signal-to-noise ( $S/N$ ) between  $z = 5.3 - 6.0$ .

The simple fact that metals exist in the early IGM begs the question, how did they get there? Population III (i.e. metal-free) and early stars have been proposed to enrich a significant volume of the early Universe, as early haloes harboring primordial galaxies have small physical scales and shallow potential wells (e.g. Madau et al. 2001; Greif et al. 2007; Wise & Abel 2008). The relatively invariant amount of C IV absorption between  $z \approx 2 - 5$  (Songaila 2001) and extended to  $z \sim 6$  (Ryan-Weber et al. 2006; Simcoe 2006) has been interpreted to mean that the majority of IGM metals were injected at  $z > 6$  (e.g. Scannapieco et al. 2002). But the most recent data set from Becker et al. (2009) and Ryan-Weber et al. (2009) shows a decline of a factor of  $\sim 4\times$  at  $z > 5.3$  compared to  $z < 4.7$ , suggesting that IGM metallicity is increasing at early epochs, assuming typical ionization conditions do not evolve much. Furthermore,  $z \sim 3$  C IV absorbers are spatially correlated with Lyman Break Galaxies (LBGs), suggesting ongoing enrichment (Adelberger et al. 2003, 2005), although these measurements are also consistent with metals being injected by dwarf galaxies at  $z = 6 - 12$  coupled with subsequent growth of clustering (Porciani & Madau 2005).

Oppenheimer & Davé (2006, hereafter OD06) explored C IV absorbers in cosmological hydrodynamic simulations, employing various heuristic prescriptions for galactic outflows to enrich the  $z \sim 2 - 6$  IGM. They determined that prescriptions based on momentum-driven winds were best able to reproduce C IV observations. OD06 also showed that an increasing ionization correction for C IV, from both cosmic evolution and energy injection from outflows, could mask a comparable increase of  $\sim \times 10$  in the true IGM metallicity from  $z \sim 6 \rightarrow 2$ . Hence widespread early enrichment from some exotic stellar population is not required to explain the relatively invariant C IV absorption over this redshift range.

Another important question is, how do early galaxies relate to the IGM metal-line absorbers at  $z > 6$ ? Davé, Finlator, & Oppenheimer (2006, hereafter DFO06) explored reionization-epoch galaxies in the simulations of OD06, finding that strong outflows are required to match the observed luminosity function (LF) of  $z \sim 6$   $i$ -band dropouts (Bouwens et al. 2006). Finlator et al. (2007) further found that the star formation histories from outflow simulations can reproduce broad-band spectral energy distributions (SEDs) of galaxies such as the lensed  $z \sim 6.7$  galaxy Abell 2218 KESR (Kneib et al. 2004). The success of these models lies in the high mass loading of early galactic superwinds, which pushes the majority of high- $z$  metals nucleosynthesized in massive stars into the IGM (Davé & Oppenheimer 2007, Oppenheimer & Davé 2008, hereafter OD08). Typically, many times more mass is driven out of galaxies than forms into stars. Hence if our models are correct, observations of IGM metal-line absorbers may

be the best way to account for the majority of metals in the  $z \gtrsim 6$  Universe.

Finally, what can IGM metal-line absorbers reveal about the topology of reionization? Fifth year data from the *Wilkinson Microwave Anisotropy Probe* (WMAP, Hinshaw et al. 2008) indicate the Universe was reionized at  $z \sim 11 \pm 1.4$  if it proceeded instantaneously. Numerical simulations suggest that reionization is a protracted process whereby individual sources create H II bubbles at  $z > 10$  that propagate outward until overlap by  $z \gtrsim 6$  (e.g. Gnedin 2000; Furlanetto & Oh 2005; Iliev 2006; Lidz et al. 2007; Finlator et al. 2009). Observations of H I absorption are divided over when reionization ends, with Fan et al. (2006) showing a discontinuity in the IGM ionization rate at  $z \sim 6$  suggesting individual ionization bubbles have finally finished overlapping, while Becker et al. (2007) finds that the Ly $\alpha$  optical depth distribution shows no evidence of a sudden end to reionization at this epoch. Metal lines provide an additional handle on how reionization progresses, allowing the bulk of cosmic volume to be probed in absorption despite a fully saturated Gunn-Peterson trough.

In this paper we consider the above questions by studying  $z = 5 - 8$  metal-line absorbers in cosmological hydrodynamic simulations that incorporate our favored momentum-driven wind model. In this wind model, the outflow speed and mass loss rate are tied to galaxy mass using a heuristic prescription as expected for momentum-driven winds (Murray, Quatert, & Thompson 2005). This wind model has enjoyed a number of successes when compared to a wide range of observations at  $z \lesssim 6$ ; most relevant is that it fairly uniquely matches observations of  $z \sim 2 - 5$  C IV absorbers (OD06). The scaling of wind speed with galaxy velocity in this model follows the relation observed in local starburst outflows (e.g. Martin 2005a; Rupke et al. 2005). We note that such scalings may arise from other physical scenarios besides momentum (or radiation) driven outflows (e.g. Dalla Vecchia & Schaye 2008); here we merely employ the scalings, without reference to the underlying physical driving mechanism.

We employ state-of-the-art GADGET-2 cosmological hydrodynamic simulations with a quarter billion particles run to  $z = 5$ ; we describe details in §2. The salient predicted galaxy and IGM properties are examined in §3, and compared to our findings in DFO06. In §4 we consider various cases for the ionization background, including the extreme cases of fully reionized and fully neutral, as well as a background with a variable intensity intended to represent ionized bubbles around individual star forming sources. §5 presents a plethora of simulated observations which are compared to available  $z > 5$  metal-line observations, as well as predictions for comparison with future data. We then study the physical and environmental parameters of simulated absorbers in §6, with a focus on how absorbers relate to galaxies and when they were injected into the IGM. §7 provides a summary. Throughout we use Asplund et al. (2005) abundances when calibrating metallicities relative to solar.

## 2 SIMULATIONS

We employ our modified version of the N-body + Smoothed Particle Hydrodynamics code GADGET-2 (Springel 2005) to

run three high-resolution  $2 \times 512^3$  particle simulation to explore the high redshift Universe. Our simulations self-consistently enrich the IGM via galactic outflows. A complete description of our code, including our wind model, can be found in §2 of OD06 with further modifications described in §2 of OD08; however we also provide some of the fundamental details involving star formation, enrichment, and feedback here.

## 2.1 Star Formation & Chemical Production

Star formation (SF) is modeled using a subgrid recipe where each gas particle above a critical density is treated as a set of cold clouds embedded in a warm ionized medium, similar to the interstellar medium (ISM) of our own Galaxy Springel & Hernquist (2003a). Gas particles eligible for SF undergo instantaneous self-enrichment from Type II supernovae (SNe). The instantaneous recycling approximation of Type II SNe energy to the warm ISM phase self-regulates SF resulting in convergence in star formation rates (SFRs) when looking at higher resolutions. The SFR is scaled to fit the disk-surface density-SFR observed in the local Universe by Kennicutt (1998)<sup>1</sup>.

Star formation below  $10 M_{\odot}$ , assumed not to result in Type II SNe, is decoupled from their high mass counterparts using a Monte Carlo algorithm that spawns star particles. The metallicity of a star particle remains fixed once formed; however, since Type II SNe enrichment is continuous while stars are formed stochastically, every star particle invariably has a non-zero metallicity.

## 2.2 Chemical Yields

The chemical yields at high redshift are dominated by Type II SNe, for which we use the metallicity-dependent yields from Chieffi & Limongi (2004) as described in OD08. These yields vary less than 15% for the 4 species we track (carbon, oxygen, silicon, & iron) as long as  $Z > 10^{-6}$ , which applies to effectively all SF in our cosmological simulation. We do not consider exotic enrichment yields from zero metallicity, Pop III, or very massive stars (VMSs, e.g. Heger & Woosley 2002, 2008), and assume a Chabrier (2003) initial mass function (IMF) throughout. Although it may be that such exotic stars have an effect on the IGM particularly in terms of metal-line ratios (e.g. Aguirre et al. 2004, 2008), the yields used here provide a standard baseline for comparison. The baseline yields are  $[O/C]=0.27$  and  $[Si/O]=-0.16$  if we consider the Chieffi & Limongi (2004)  $Z = 10^{-3}$  yields assuming Asplund et al. (2005) abundances; the carbon mass yield ejected by SNe is  $3.0 \times 10^{-3}$  the total stellar mass in a Chabrier IMF. The integrated gas-phase abundance ratios of the  $z = 6$  d16n256vzw simulation box are  $[O/C]=0.23$  and  $[Si/O]=-0.13$  reflecting the Chieffi & Limongi (2004) yields inputted in our simulations.

To allow the reader to scale our results to a different set of theoretical Type II SNe yields we provide Table 1 listing the integrated yields assuming a Chabrier (2003) IMF slope with  $\beta = 0.18$ , where  $\beta$  is the stellar IMF mass

fraction in the range indicated in the second column<sup>2</sup>. We have interpolated the published yields to  $Z = 10^{-3}$  (i.e.  $0.08 Z_{\odot}$ ) using their various metallicity models, because this is near the median stellar metallicity at  $z = 6$  ( $Z_{stellar}(z = 6) = 1.48 \times 10^{-3}$ ). There exists little spread for the oxygen and silicon yields between Chieffi & Limongi (2004), Woosley & Weaver (1995), and Portinari et al. (1998) despite different SNe mass progenitor ranges. 38% less carbon is produced from the Woosley & Weaver (1995) yield models, which is significant when we consider a measurement such as  $\Omega(C\text{IV})$  (§5.2.3).

We note that there may be reasons to favor a more top-heavy or bottom-light IMF at high redshifts (e.g. Davé 2008, i.e.  $\beta$  increases). However, since our simulations are well-matched to observed  $z \sim 6$  rest-UV LFs (as we will show in §3), and since metals mostly come from the same massive stars responsible for UV emission, our total metal production should be reasonably well-constrained. Along these lines we show the yields using the 30 – 120  $M_{\odot}$  from Portinari et al. (1998) in Table 1; silicon appears to be significantly under-produced in SNe ejecta. For comparison we include yields from Heger & Woosley (2008) from zero metallicity stars. These yields show less difference relative to Chieffi & Limongi (2004) than the top-heavy Portinari et al. (1998) (except for oxygen), perhaps indicating just how hard it is to clearly identify the nucleosynthetic signatures of Pop III stars.

## 2.3 Feedback Model

The implementation of winds follows Springel & Hernquist (2003a), using a Monte Carlo ejection mechanism governed by two parameters, the outflow velocity  $v_{wind}$  and the mass loading factor  $\eta$ , where the mass loading factor is defined as the outflow mass rate ( $\dot{M}_{wind}$ ) in units of the galaxy’s SFR, i.e.  $\dot{M}_{wind} = \eta \times \text{SFR}$ . The wind model we employ here follows scalings of  $v_{wind}$  and  $\eta$  expected for momentum-driven winds; this fairly uniquely matches a broad range of observations including IGM enrichment between  $z = 6 \rightarrow 1.5$  traced by C IV (OD06) and at  $z < 0.5$  traced by O VI (Oppenheimer & Davé 2009), the LFs of  $z = 6$  galaxies (DFO06), the galaxy mass-metallicity relations (Finlator & Davé 2008), and the enrichment and entropy levels in intragroup gas (Davé et al. 2008). The scalings depend on galaxy velocity dispersion ( $\sigma$ ):

$$v_{wind} = 3\sigma\sqrt{f_L - 1}, \quad (1)$$

$$\eta = \frac{\sigma_0}{\sigma}, \quad (2)$$

where  $f_L$  is the luminosity factor, which is the luminosity of the galaxy in units of the critical (or sometimes called Eddington) luminosity of the galaxy, and  $\sigma_0$  provides a normalization for the mass loading factor. Here we randomly select  $f_L = [1.05, 2]$  for each SPH particle we kick, following observations of local starbursts by Rupke et al. (2005), and we take  $\sigma_0 = 150 \text{ km s}^{-1}$ .  $\sigma$  is estimated from the galaxy’s mass following Mo et al. (1998), where the mass is obtained from an on-the-fly friends-of-friends galaxy finder.

<sup>1</sup> Even if this scaling is not applicable at  $z > 5$ , the accretion rate determines the SF as we argue in §3.2.

<sup>2</sup>  $\beta = 0.18$  for a Chabrier IMF for stars 10 – 100  $M_{\odot}$ , which we assume are the stars that undergo Type II SNe.

**Table 1.** Type II Supernovae Yields<sup>a</sup>

Reference	Mass Range	$Z$	[C/H]	[O/H]	[Si/H]	[O/C]	[Si/O]
<b>Chieffi &amp; Limongi (2004)<sup>b</sup></b>	13-35 $M_{\odot}$	$10^{-3}$	0.13	0.40	0.24	0.27	-0.16
Woosley & Weaver (1995)	12-40 $M_{\odot}$	$10^{-3}$	-0.08	0.39	0.25	0.47	-0.14
Portinari et al. (1998)	10-120 $M_{\odot}$	$10^{-3}$	-0.05	0.43	0.17	0.48	-0.26
Portinari et al. (1998)	30-120 $M_{\odot}$	$10^{-3}$	-0.21	0.35	-1.54	0.56	-1.89
Heger & Woosley (2008)	10-100 $M_{\odot}$	0	0.02	0.20	-0.29	0.18	-0.49
d16n256vzw $z = 6$ SPH	–	–	–	–	–	0.23	-0.13

<sup>a</sup> Assuming a Chabrier IMF slope and  $\beta = 0.18$  (i.e. 18% of stellar IMF is covered by the mass range in column 2 and only this mass range contributes to Type II SNe yields.).

<sup>b</sup> We apply this set of metallicity-dependent yields in our simulations.

## 2.4 Runs

The simulations adopt the cosmological parameters based on the 5-year WMAP results (Hinshaw et al. 2008), namely  $\Omega_0 = 0.25$ ,  $\Omega_{\Lambda} = 0.75$ ,  $\Omega_b = 0.044$ ,  $H_0 = 70 \text{ km s}^{-1} \text{ Mpc}^{-1}$ ,  $\sigma_8 = 0.83$ , and  $n = 0.95$ . The value of  $\sigma_8$  slightly exceeds the favored WMAP data alone, but agrees better with the combined results including Type Ia SNe and baryonic acoustic oscillation data. A greater  $\sigma_8$  results in appreciably more SF at high- $z$ , which is important since SF drives the enriching outflows. Our runs with this cosmology are named the *d-series*; the primary run is named d16n512vzw using our standard naming convention, indicating the box spans 16 comoving  $h^{-1} \text{ Mpc}$ s with  $512^3$  each of gas and dark matter particles. The *vzw* suffix indicates our implementation of the momentum-driven wind model as described in OD08 (with one inconsequential exception: we no longer impose an upper limit due to SN energy limitations on  $v_{\text{wind}}$ ). The gas particle mass is  $5.4 \times 10^5 M_{\odot}$ , which translates to a minimum galaxy baryonic mass of  $1.7 \times 10^7 M_{\odot}$  assuming a galaxy is resolved with 32 particles (which we will demonstrate later). The softening length is set to 0.6 comoving  $h^{-1} \text{ kpc}$ .

Two more simulations, d8n512vzw and a d32n512vzw, are also run to explore numerical resolution convergence. The respective softening lengths are 0.3 and  $1.2 h^{-1} \text{ kpc}$ , and the minimum galaxy baryonic mass resolutions are  $2.1 \times 10^6$  and  $1.4 \times 10^8 M_{\odot}$ . We will show that the primary enrichers of the IGM are galaxies with masses  $\sim 10^{7-8.5} M_{\odot}$ , which are statistically sampled best in the  $16 h^{-1} \text{ Mpc}$  box.

The d16n512vzw simulation was run to  $z = 3$ , however we only consider outputs down to  $z = 5$  here. This simulation was run on the Intel 64-bit Abe Cluster at the National Center for Supercomputing Applications on 128 processors, requiring 32,500 processor hours. The d8n512vzw and d32n512vzw simulations were run only to  $z = 5.5$  and 4.5 respectively, each consuming approximately half the above processor hours. We run the Spline Kernel Interpolative DENMAX (SKID)<sup>3</sup> group finder on the  $z = 8, 7, 6$ , and 5 outputs to identify galaxies.

## 3 PHYSICAL PROPERTIES

In this section we explore key physical and observational predictions of our new simulations and relate them to find-

ings from our previous lower-resolution simulations. This is intended to demonstrate continuity with our previous works, as well as to provide a more global context for our exploration of high- $z$  metal-line absorbers. We begin by presenting the  $z = 6$  galaxy stellar mass ( $M_*$ ) function in our two simulation boxes, and relating this to earlier papers where we fit observables best with a momentum-driven wind model. We show that the  $16 h^{-1} \text{ Mpc}$  box is the best one for studying high- $z$  IGM metals, despite the fact that it is not large enough to sample the space density of the most luminous  $z \sim 6$  galaxies. Finally, we show global evolutionary trends in star formation, wind properties, and metal enrichment.

### 3.1 Galaxy Mass Function

In DFO06 we explored the properties of reionization-epoch galaxies ( $z = 9 \rightarrow 6$ ), finding that the *mzw* wind model most capable of reproducing observations (specifically Bouwens et al. 2006) compared to the constant wind (*cw*) and no wind (*nw*) cases. The *mzw* model is similar to the *vzw* model, the only difference being that the wind speed at a given  $\sigma$  is constant in *mzw* while it has a random spread in *vzw*. The key point is that  $\eta$  varies with  $\sigma$  the same way in both models, and as we showed in DFO06,  $\eta$  governs high- $z$  SF by removing gas that would otherwise form into stars. The constant wind model is that of Springel & Hernquist (2003b), with  $v_{\text{wind}} = 484 \text{ km/s}$  and  $\eta = 2$ .

We plot the stellar mass function of  $z = 6$  galaxies ( $\Phi(M_*)$ ) in Figure 1 for the d8n512vzw (orange), d16n512vzw (black), and d32n512vzw (green) simulations. We compare it to the w8n256vzw simulation (dot-dashed magenta), which is part of the w-series simulations explored in DFO06. The w8n256vzw simulation has nearly the same resolution as the d16n512vzw simulation, but uses the first-year WMAP results (Tegmark et al. 2004). This cosmology ( $\Omega_0 = 0.3$ ,  $\Omega_{\Lambda} = 0.7$ ,  $\Omega_b = 0.04$ ,  $H_0 = 70 \text{ km s}^{-1} \text{ Mpc}^{-1}$ ,  $\sigma_8 = 0.90$ ) produces almost double the stars over  $M_* = 10^{7.0-8.5} M_{\odot}$  owing to its higher  $\sigma_8$ . In the d16n512vzw simulation, we find 1.83% of baryons in galaxies and 0.13% in stars; the respective numbers in the w8n256vzw simulation are 3.10% and 0.26%.

We use  $\Phi(M_*)$  to argue that we are resolving the galaxies responsible for metal enrichment. Stellar mass can be used as a direct proxy for the integrated metal production if two conditions are met: (i) All metals (those not trapped in stellar remnants) are produced in short-lived, massive stars

<sup>3</sup> <http://www-hpcc.astro.washington.edu/tools/skid.html>

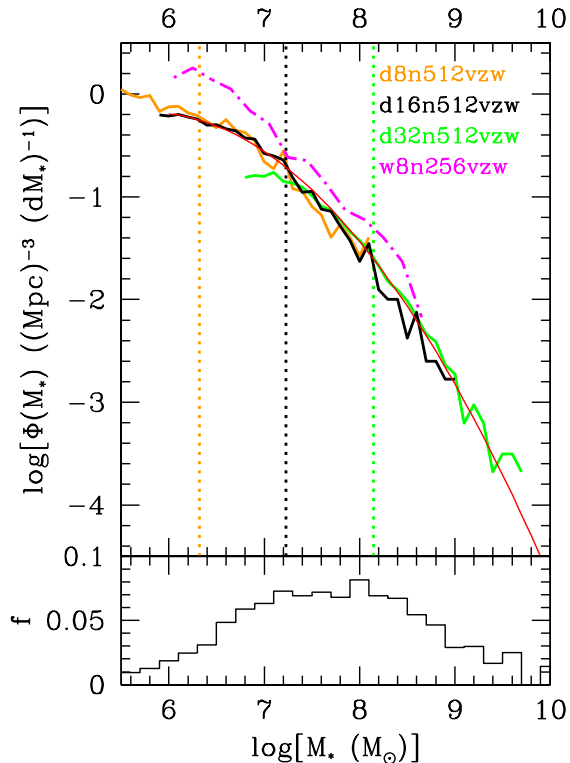


**Figure 1.** The  $z = 6$  stellar mass function of galaxies in the d8n512vzw (orange line), d16n512vzw (black line), and d32n512vzw (green line) boxes in units of  $\#/\log(dM_*)/\text{Mpc}^3$  (comoving). Corresponding dotted vertical lines show the galaxy mass resolution limit. For comparison we show the mass function of our older w8n256vzw model (dot-dashed magenta line, from DFO06), which is higher due to the different cosmology. The solid red line is a least-squares fit to our three simulations (Equation 3). We define the characteristic  $M_*$  as where the fit matches the slope of a  $\Phi \propto M_*^{-1}$  power law, which is at  $M_* = 10^{7.7} M_\odot$ . The bottom panel shows a histogram of the stellar mass. 72% of the mass is in galaxies with  $M_* = 10^{6.7-8.7} M_\odot$ .

(i.e. Type II SNe), which is a fair assumption given that longer lived stars (AGB stars) have not had time to enrich much by  $z \sim 5$ ; and (ii) stellar mass is a direct proxy for the integrated number of Type II SNe. The stellar mass contained in GADGET-2 star particles consists only of long-lived, non-SN stars, so the mass in star particles is a good record of the integrated Type II SNe contribution.

We find that a two-dimensional polynomial fit to the logarithmic stellar mass function provides a good, simple fit:

$$\log[\Phi(M_*)] = -8.70 + 2.95 \log M_* - 0.255 (\log M_*)^2. \quad (3)$$

Shown as the red line in Figure 1, this fit obtains a slope of  $-1$  at  $M_* = 10^{7.7} M_\odot$ , making this the characteristic  $M_*$  at  $z \sim 6$  where the most mass per logarithmic  $M_*$  bin is held. We cannot fit the mass function over 4 dex effectively with a Schechter function, because the high mass end does not display an exponential cutoff and the low-mass end shows a gradual turnover owing to filtering by the cosmic UV background (e.g. Thoul & Weinberg 1996; Iliiev 2007). Integrating Equation 3, we find that 72% of mass is in galaxies with  $M_* = 10^{6.7-8.7} M_\odot$ . To illustrate the stellar mass distribution, the bottom panel of Figure 1 shows the fractional

mass in each bin. The median  $M_*$  in terms of integrated mass is  $M_* = 10^{7.6} M_\odot$  for the d16n512vzw simulation, and  $M_* = 10^{7.7} M_\odot$  when including all three simulations. The d32n512vzw box is better able to account for the cosmic variance of more massive galaxies, but its mass resolution is comparable to the median stellar mass, so it cannot account for early enrichment from small galaxies. The d8n512vzw run, conversely, does not produce many galaxies above  $10^8 M_\odot$ , so it does not sample the high-mass end sufficiently. The d16n512vzw run is well-suited to resolve the relevant galaxy mass range, so we employ this run from here on in.

### 3.2 Star Formation Rate Function

A high- $z$  galaxy’s SFR is more easily measured than its stellar mass, since the former can be estimated from optical data while the latter requires near-infrared data. Our simulations predict a tight relation between SFR and  $M_*$  at  $z = 6$ , where  $\text{SFR} = 9.2 M_*^{0.94} M_\odot \text{Gyr}^{-1}$ . (4)

This nearly linear relation is similarly tight in our simulations at all redshifts (DFO06, see their Figure 4; Finlator et al. 2006; Davé 2008), with a low scatter, and is mostly insensitive to outflow model (Davé 2008). This relation arises from the dominance of smooth, filamentary cold mode gas accretion, where the SFR is regulated by the dynamical timescale for gas infall in slowly-growing halo potentials (e.g. Kereš et al. 2005); therefore the SF law we scale to (Kennicutt 1998) has little effect on the SFR, chemical production, and feedback. Mergers are a sub-dominant process for fueling galaxies, particularly at early times and in smaller galaxies (Kereš et al. 2008), which is why the scatter is small.

In Figure 2 we show our d16n512vzw simulated rest-frame 1350 Å UV luminosity function at  $z = 6$ , which is effectively a SFR function (including extinction). We compare to data from Bouwens et al. (2006) and Bouwens et al. (2007). We compute simulated galaxy luminosities by passing their SF histories through the Bruzual & Charlot (2003) population synthesis model, and applying a tophat filter around 1350 Å. Dust extinction is critical in this comparison; we apply two extinction laws to our simulated galaxies: (i) the solid line represents a constant dust extinction, where  $E(B - V) = 0.069$ , which leads to 50% flux attenuation at 1600 Å using the Calzetti et al. (2000) law (we will use this value for our local ionizing field); and (ii) the dashed line uses the metallicity-dependent extinction law calibrated from local galaxies introduced in Finlator et al. (2006) and employed in DFO06, which predicts less attenuation for the lower mass galaxies. In both cases the agreement with data is reasonable. This shows that the star formation rates, and hence metal production rates, in our simulated galaxies are plausible.

Numbers across the bottom of this figure show the median  $\log[M_*]$  corresponding to a given rest-UV magnitude. The characteristic  $M_*$  from Equation 3 corresponds to  $M_{1350\text{\AA}}^\odot = -17.1$ , which is roughly one magnitude below current detection limits. The green dotted lines indicate the magnitude range of the parent galaxies of  $z = 6$  CIV absorbers, which we identify in §6.3. Hence the originating galaxies of currently observed high- $z$  CIV systems are mostly below today’s detection thresholds.

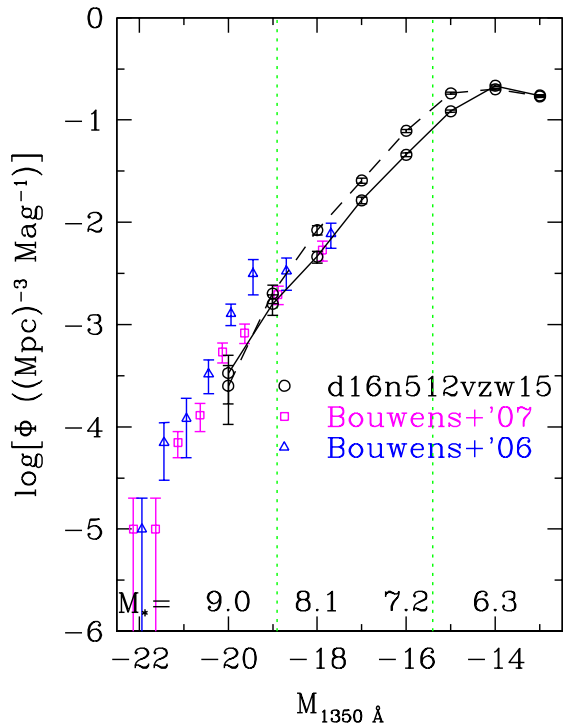


**Figure 2.** The simulated  $z = 6$  rest-UV luminosity function (1350Å magnitudes AB) from our d16n512vzw run. Solid line assumes uniform dust extinction of  $E(B - V) = 0.069$ , dashed line uses the Finlator et al. (2006) metallicity-dependent extinction. These are compared to observations from Bouwens et al. (2006) (blue triangles) and Bouwens et al. (2007) (magenta squares). The agreement is good in the overlap region. The majority of SF remains below current detection limits, which implies that the sources of high- $z$  IGM metals have yet to be detected. The range of  $M_{1350\text{Å}}$  for parent galaxies of  $z = 6$  C IV absorbers are demarcated by the dotted green lines. Median logarithmic stellar masses at a given magnitude are listed along the bottom.

### 3.3 Cosmic Star Formation

Figure 3 (top panel) shows evolution of the cosmic SFR density (SFRD) per comoving volume, indicating a rise of a factor of three over the range  $z = 8 \rightarrow 5$ . The values are in the range of data, though the observations span a large range, in part owing to differences in the adopted limiting luminosity in each case. For example, Bouwens et al. (2007) finds  $6.7\times$  more SFRD when they reduce the limiting luminosity by a factor  $7.5\times$  for the  $z$ -band dropouts ( $\langle z \rangle = 7.4$ ). Most of the  $z = 6$  stellar mass and SF in our simulations remain below the detection limits of current surveys. At  $z = 6$ , we find 31% of the SFRD arises from galaxies with  $M_* > 10^8 M_\odot$ , 39% from  $M_* = 10^{7-8} M_\odot$ , and the remaining 30% from masses below this. At  $z = 8$ , 61% of the SFRD arises in galaxies with  $M_* < 10^7 M_\odot$ . We note that Bouwens et al. (2007) examined the evolution of the cosmic SFRD and found that our momentum-driven wind model provided the best match to the observed evolution from  $z \sim 7 \rightarrow 4$ , of the models considered there.

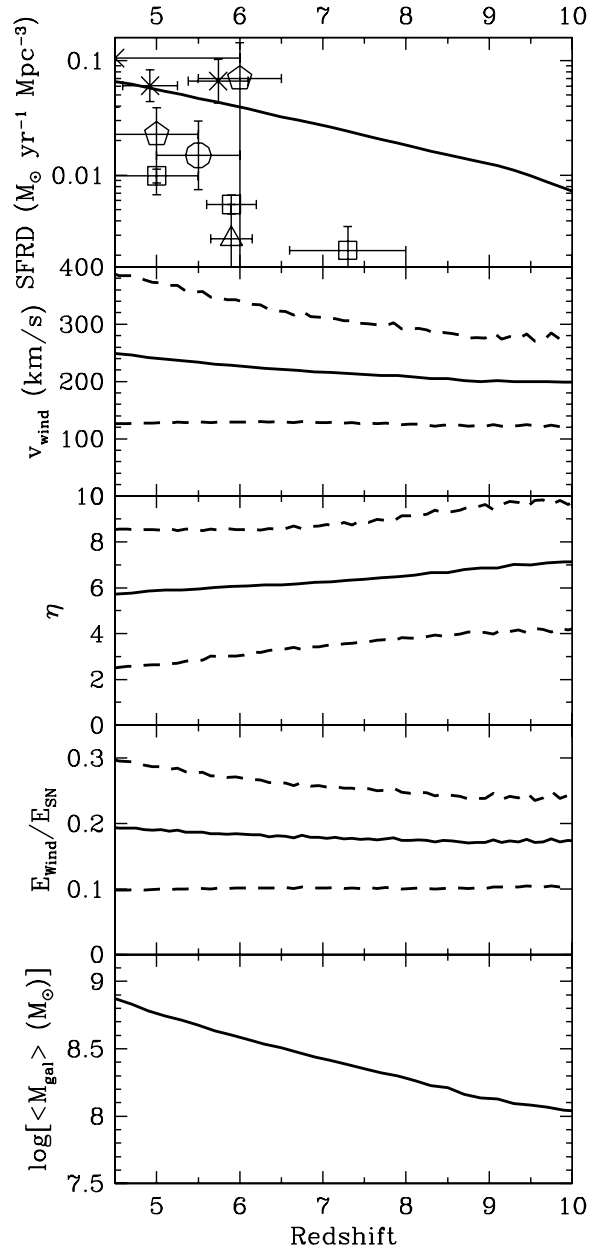


**Figure 3.** *Top:* The cosmic SFRD from all galaxies in the d16n512vzw simulation (solid line), compared to data assuming a Chabrier IMF at high redshift. Data are from the Hopkins (2004) compilation (X's), Fontana et al. (2003) (circle), Bunker et al. (2004) (triangle), Thompson et al. (2006) (pentagons), and Bouwens et al. (2008) (squares). Average wind properties (solid lines) in the next three panels show typical  $v_{\text{wind}} = 200 - 250 \text{ km s}^{-1}$  with mass loading factors  $\eta \sim 6 - 7$ . The energy in outflows is  $\approx 20\%$  of the available supernova energy at these redshifts, assuming a Chabrier IMF. One sigma dispersions are indicated by dashed lines. The baryonic mass of galaxies responsible for winds (bottom panel) increase  $6\times$  between  $z = 10 \rightarrow 4.5$  (bottom panel).

### 3.4 Winds

The adopted dependence of momentum-driven wind scalings from galaxy mass results in the median wind speed growing and median mass loading factor declining towards lower redshifts (OD08). This has direct ramifications for reionization-

era galaxies, since SFRs are attenuated by a factor of  $(1+\eta)$  relative to the no-wind case. This is because  $\frac{\eta}{1+\eta}$  of infalling gas that would otherwise be converted into stars, instead is ejected in outflows. This factor assumes that outflows do not return to galaxies, which is a fair assumption at high redshift because outflow material generally does not recycle back into galaxies within a Hubble time at these epochs (OD08).

The lower panels of Figure 3 show that high- $z$  wind properties have a relatively weak redshift dependence from  $z = 10 \rightarrow 5$ :  $v_{\text{wind}}$  increases by 20% (second panel) and  $\eta$  declines by 17% (third panel), despite an increase of  $6\times$  in the average baryonic mass of a galaxy driving the winds (bottom panel, i.e. weighted by  $\dot{M}_{\text{wind}}$ ). The reason is that  $\sigma$  is proportional to  $M_{\text{gal}} \times H(z)$ , and the declining  $H(z)$  turns out to roughly cancel the increase in  $\langle M_{\text{gal}} \rangle$  during this epoch, resulting in only modest evolution of wind properties. Fiducial values during reionization in our model are therefore  $v_{\text{wind}} \sim 200 \text{ km s}^{-1}$  and  $\eta \sim 6$ . The energy budget of momentum driven winds remains roughly 20% of the total SN energy assuming a Chabrier IMF (fourth panel). High- $z$  winds require substantial energy input, but the wind speeds are relatively mild compared to low- $z$  outflows from LIRGs and ULIRGs (e.g. Martin 2005a; Rupke et al. 2005). As before, we find that substantial mass ejection is a key feature of our wind model: the amount of material ejected at these epochs is many times that which forms into stars.

### 3.5 Metallicity Distribution

One reason why enriching the IGM is easier at high- $z$  is that the physical scale of the Universe is small. OD08 showed that in our wind model, winds propagate a similar physical distance ( $\sim 60 - 100 \text{ kpc}$ ) for all redshifts and galaxy masses; the comoving volume a galaxy can enrich therefore goes as  $(1+z)^3$ . Figure 4 illustrates the rapid growth of metallicity at IGM overdensities from  $z = 8 \rightarrow 5$ . The gradually rising  $Z - \rho$  trend in place at all four redshifts is one of the defining signatures of the momentum-driven wind enrichment. In contrast, a wind model with constant  $v_{\text{wind}}$  (e.g. Springel & Hernquist 2003b) will create a flatter metallicity-density relationship with either a sharp drop-off at lower overdensity (cf. Figure 10 of OD06) or a rise in metallicity if superwinds are even stronger (cf. Figure 8 of Cen et al. (2005)) signifying efficient enrichment of voids. Under our model the IGM metallicity grows between  $z = 8 \rightarrow 5$  by a factor of  $7\times$  at an overdensity ( $\delta \equiv \rho/\bar{\rho} - 1$ ) of 80 and  $15\times$  at  $\delta = 8$ .

Despite some metals reaching cosmic mean densities, most of the volume remains unenriched, especially the voids. The cumulative volume filling factors of metals in the bottom panel of Figure 4 show this, as even regions with  $Z > 10^{-3} Z_{\odot}$  fill only about 1% of the simulation volume at  $z = 5$ . Filling factors increase only modestly to lower  $z$  (OD08), which is somewhat remarkable given that these models can match most available IGM metal-line data. Hence the presence of diffuse IGM metal absorbers does not necessarily indicate widespread metal distribution. We will return to this point, and the inhomogeneous enrichment it implies, later.

Regions of galactic overdensities ( $\rho/\bar{\rho} \gtrsim 10^3$ ) are generally enriched rapidly to  $Z \sim 0.1 Z_{\odot}$  or higher. The metal-

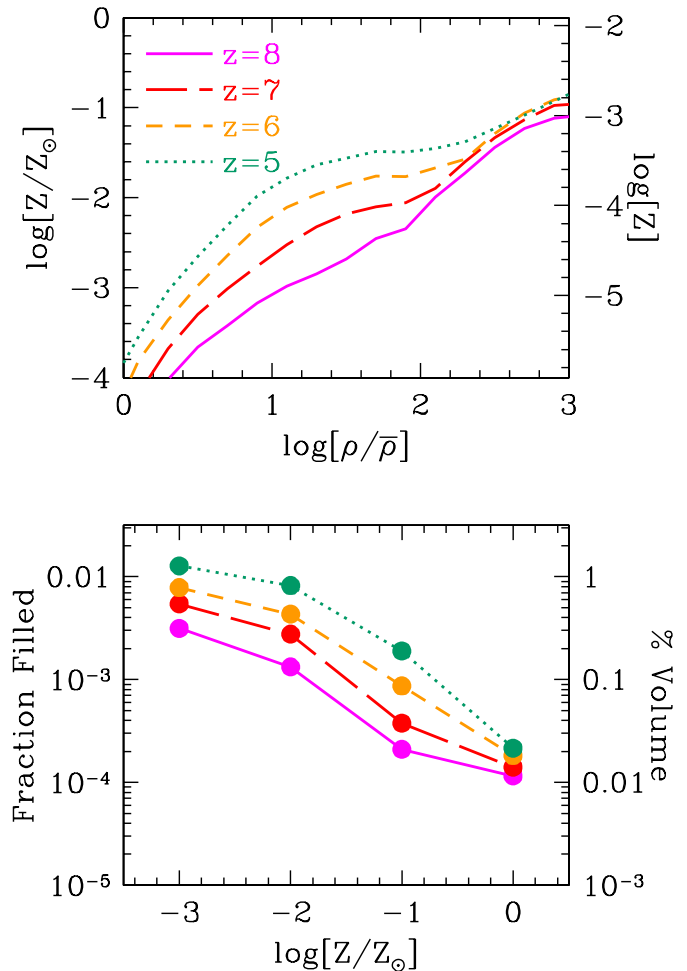


**Figure 4.** *Top:* The average metallicity-density relationship at  $z = 8, 7, 6, 5$  from the d16n512vzw simulation.  $Z$  is the total mass fraction of metals;  $Z_{\odot} = 0.0122$ . A clear gradient is established early on, and as time passes the diffuse IGM is enriched more quickly than high-density regions. *Bottom:* The cumulative volume filling factor of metals versus metallicity, indicating an inhomogeneous distribution of metals with only 1% of the Universe enriched to  $10^{-3} Z_{\odot}$  by  $z = 6$ , despite some metals spreading to near the cosmic mean density.

licity does not grow much at such overdensities, which is reflected in the lack of predicted evolution in the mass-metallicity relation from  $z = 8 \rightarrow 6$  in DFO08 (see their Figure 5). The fraction of cosmic volume enriched to  $Z = Z_{\odot}$  is 0.01-0.02%, which is actually a factor of 1.5-3 $\times$  higher than that at  $z = 0.25$  (Oppenheimer & Davé 2009). It is astounding to consider that the volume fraction of the Universe enriched to around solar metallicity may change very little between  $z = 8 \rightarrow 0$ ; the key difference is the corresponding regions at low redshift contain orders of magnitude more baryons. This is a result of our momentum-driven wind model based on locally observed outflows. Davé & Oppenheimer (2007) showed these winds efficiently enrich IGM overdensities at high- $z$ , some to  $\geq Z_{\odot}$ , while by  $z = 0$  most of these metals recycle back into galactic environments and later winds often cannot escape out of galactic haloes (OD08).

Many of the trends noted above can be seen in Figure 5,

which shows the locations of galaxies in the upper left and the metallicity-density distribution in the upper right in a  $25 \text{ km s}^{-1}$ -thick slice extending across the d16n512vzw simulation box. Gray indicates zero metallicity in these frames, which corresponds to the vast majority of the IGM, and shows the nascent cosmic web. Most of the volume remains unenriched at these redshifts, while regions within early galaxies become enriched up to a tenth solar or more. Clustering between early galaxies and enriched portions of the IGM is strong. This illustrates that the galaxy-absorber connection at high- $z$  is extremely tight, as we investigate further in §6.3.

#### 4 IONIZATION BACKGROUNDS

To make predictions for observable metal-line absorbers, we must obtain ionization corrections for relevant metal ions. This requires that we have a model for the photoionization rate at each point in the simulation volume. Ideally, we would like to self-consistently track the local ionization spectrum in these simulations. But this must await a full time-dependent, non-equilibrium radiative transfer implementation, which we are in the process of developing (Finlator et al. 2008, 2009) but do not yet have. Hence for this work, we will consider three ad hoc cases for the ionization background (dubbed *No Field*, *HM2001*, and *Bubble*) that span a plausible range.

Note that our simulations are originally run with a uniform Haardt & Madau (2001) ionizing background, and we are only imposing these backgrounds in post-processing. This obviously does not properly capture the dynamical effects of different pressure forces in our three cases. However, since dark matter is dynamically dominant in the relatively low-density regions giving rise to IGM absorbers, post-processing the background to obtain ionization corrections is a good approximation.

##### 4.1 Ionization Cases

**No Field:** Our first case assumes a fully neutral IGM, where no ionizing background exists at wavelengths below the Lyman limit, while lower energy photons stream freely. This extreme case may be applicable if metal injection precedes ionization fronts, or more realistically if the IGM recombines in regions enriched and ionized at earlier times. Oxygen remains in its ground state due to the O I ionization potential (13.618 eV) being barely higher than the H I ionization potential, while C I (11.260 eV) and Si I (8.151 eV) are completely ionized to the second level.

**HM2001:** Our second case assumes reionization is complete and a spatially-uniform background applies everywhere. We use the Haardt & Madau (2001) background assuming a contribution from quasars and 10% of photons above the Lyman limit from star forming galaxies generated by their Cosmic Ultraviolet Background (CUBA) program; at  $z > 6$ , star-forming galaxies dominate the ionizing flux. We divide the total flux by a factor of 1.6 as we did in OD06 in order to match the summed flux decrement of the Ly $\alpha$  forest down to  $z = 2$ . An assumption of a spatially-uniform ionization background is probably far from correct at

$z > 6$ , but this is intended to represent another extreme case like *No Field*. Ionization fractions for metal lines are calculated using CLOUDY-generated (Ferland et al. 1998) ionization tables as a function of density and temperature, as described in OD06.

**Bubble:** The last case assumes that the ionizing flux of the nearest galaxy dominates, which may be the most realistic scenario during reionization. This is applicable if metals remain near enough to their parent galaxies to be dominated by the local ionizing intensity, which we will show is often true since metals typically reside within 30 kpc of the originating galaxy. Of course, detailed radiative transfer effects of escaping ionization and subsequent recombinations will play a critical role, so this scenario should be considered a crude proxy for a patchy reionization model.

To implement the *Bubble* field, we consider the ionizing field from only the nearest galaxy, weighted by the inverse square law. We assume an average SED per stellar mass by taking the average Bruzual & Charlot (2003) stellar synthesis spectrum of *all* the stars in the simulation box for a given redshift, accounting for their ages and metallicities. We then calculate the impinging flux using the stellar mass and distance of the nearest galaxy, which is identified for each SPH particle. Note that the same ionizing flux per unit stellar mass is assumed to emanate from each galaxy at a given epoch; we do not account for variations in nearest galaxy SEDs, which is another approximation required to make the problem computationally tractable.

We attenuate the emission from galaxies by dust extinction. The assumed extinction has a fixed value of  $E(B-V) = 0.069$ , as shown in Figure 2 to broadly match the observed rest-UV LF. To calculate how the emergent SED is attenuated, we use the theoretical dust absorption curve from the X-ray to the far-IR of Weingartner & Draine (2001), using their grain size distribution of silicate and carbonaceous grains found to fit the Small Magellanic Cloud (SMC) bar. We use this curve because  $z \sim 3$  LBGs exhibit the smaller grain size distributions of SMC-like dust (Vijh et al. 2003). Note that we cannot directly apply the empirical Calzetti et al. (2000) extinction law because it extends only down to 1200 Å, while we are especially interested in the attenuation at energies where C IV and Si IV are ionized (i.e.  $< 400 \text{ Å}$ ). For each SPH particle, the impinging flux is then the dust-attenuated emission divided by the distance from the nearest galaxy squared. We then use CLOUDY to generate the resulting metal ionization fractions, which is then used to obtain the optical depth for any ion along the LOS as described in OD06.

We plot the *HM2001* field at  $z = 8$  and 6 in Figure 6, along with the *Bubble* field, where we assume a  $M_* = 10^7 M_\odot$  galaxy at 10 kpc (typical values) for concreteness. The difference between the solid and dotted orange lines for the *Bubble* case at  $z = 6$  illustrates the effects of dust attenuation. Dust absorption in all of the Weingartner & Draine (2001) models sharply peaks at 600-900Å, causing a dip. There is a clear Lyman break, which in our cases arises mostly from stellar atmospheres, and secondarily from dust. We note that this break is not nearly as strong as that observed by Shapley et al. (2006) in Lyman break galaxies at  $z \sim 3$ , perhaps indicating that there is a fairly small escape fraction of ionizing photons; for instance, Haardt & Madau

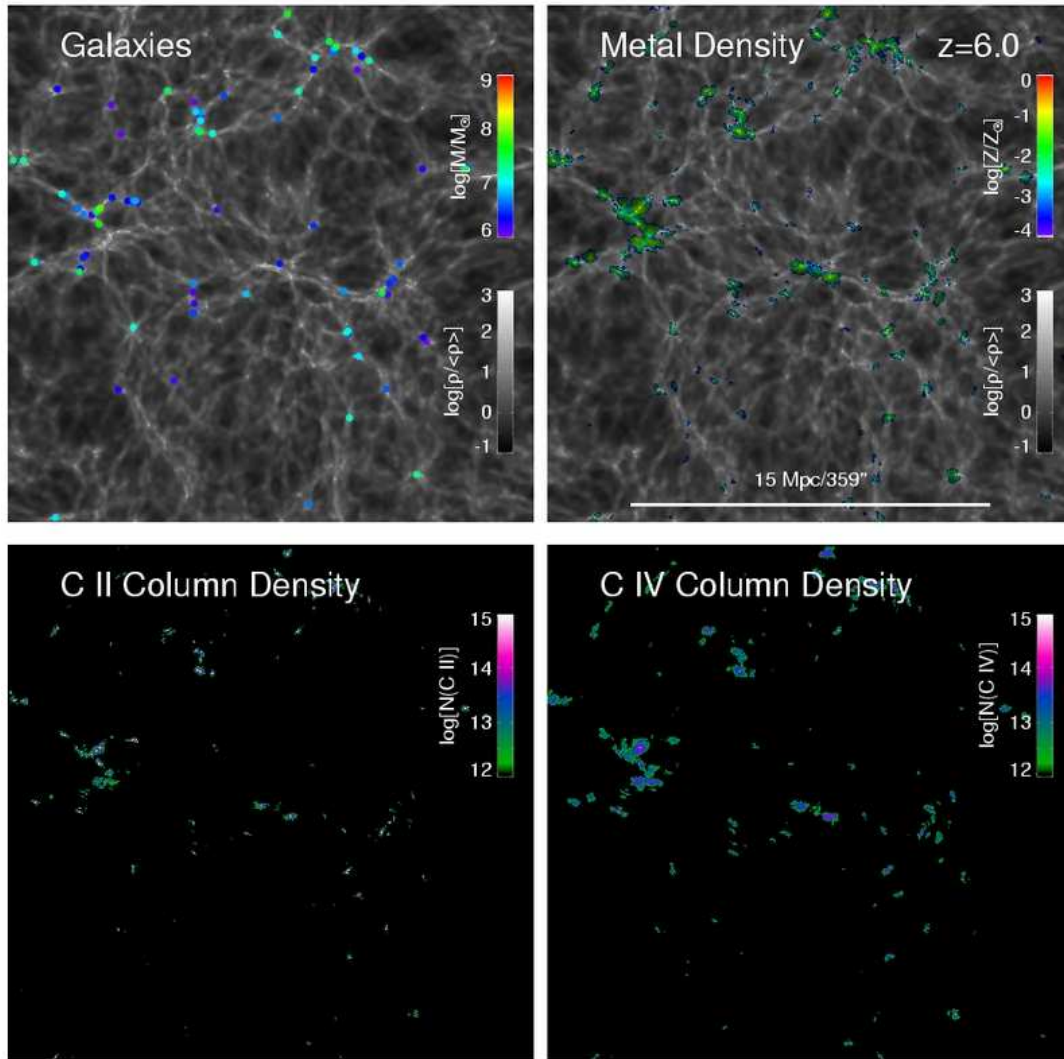


**Figure 5.** A  $25 \text{ km s}^{-1}$  slice of IGM spanning the  $16 \text{ comoving } h^{-1} \text{ Mpc}$ s of the d16n512vzw simulation at  $z = 6$ . *Upper left:* The locations of galaxies are shown as colored points, where the color corresponds to stellar mass, overlaid on the gas overdensity represented in greyscale. *Upper right:* Color indicates the enrichment level; the vast majority of the IGM remains unenriched, and metals are close to galaxies. The scale bar indicates the arcsecond scale on the sky using the Wright (2006) on-line calculator. *Bottom panels:* C II (left) and C IV (right) column densities in this  $25 \text{ km/s}$  slice, assuming a uniform Haardt & Madau (2001) ionization background. C II traces denser regions compared to C IV, which traces the volume distribution of metals extremely well.

(2001) assume a global 10% escape fraction. However, because these data are from lower- $z$  and higher- $M_*$  galaxies, it may not be applicable here. For simplicity, we do not assume an overall escape fraction.

Comparing the *Bubble* and *HM2001* fields at  $z = 6$ , the strength of the Lyman break is much less in the *Bubble* case. This is mostly because our typical galaxy is younger and more metal-poor than that assumed by Haardt & Madau (2001) ( $0.2 Z_\odot$ , 0.5 Gyrs), which leads to a harder ionizing source. Two secondary reasons for greater hardness are: (i) the *Bubble* Lyman-break attenuation due to dust is less than the *HM2001* attenuation applied ( $\sim 3$  vs. an overall 10% escape fraction); and (ii) the dust attenuation declines at the ionization potentials of C IV and Si IV (shown). This leads to greater ionization fractions at these higher states in the *Bubble* field, which has observable implications as we will show throughout §5.

## 4.2 Ionization Fraction Behavior

Before delving into the observables, we present here a primer for understanding metal-line observations resulting from our two assumed ionization backgrounds, the *HM2001* and the *Bubble* fields. The *No Field* case is straightforward (i.e. ionization fractions of unity for C II, O I, and Si II), but the often nuanced behavior of the other two fields has some perhaps unexpected consequences. We consider metals in  $\rho - T$  phase space exploring both low and high-ionization species at two redshifts that span the redshift range we consider.

Figure 7 plots colored contours corresponding to the *HM2001* (left panels) and the *Bubble* (right panels) backgrounds in  $\rho - T$  phase space for C II (solid blue) and C IV (dot-dashed red) at  $z = 8$  and  $z = 5$  (upper and lower panels, respectively). Each contour step represents an increase of 20% in the ionization fraction for the corresponding ion.

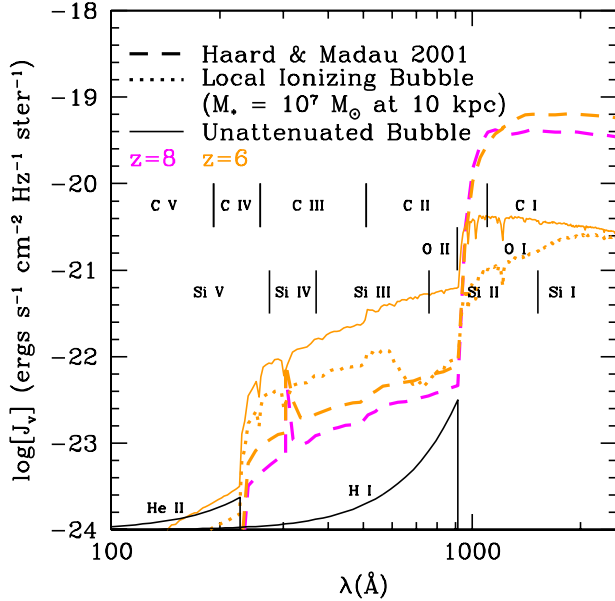


**Figure 6.** Ionizing background spectra: The *HM2001* (dashed) ionization background at  $z = 8$  (magenta) and  $z = 6$  (orange) are compared to the *Bubble* field arising from a  $z = 6$   $M_* = 10^7 M_\odot$  galaxy at 10 kpc. The thin solid orange line represents the unattenuated Bruzual & Charlot (2003)-computed SED at  $z = 8$  to compare with the dust-attenuated (thick dotted orange line) SED. For reference, ionization potentials for carbon, oxygen, and silicon are indicated, and the relative cross-sections from H I and He II as a function of wavelength are shown along the bottom.

Overlaid are thick gray logarithmic metal density contours (darker contours indicate higher metal densities) at the respective redshifts. Overlapping color and gray contours represent regions of phase space where absorption in that ion will arise for a given ionization field.

The *HM2001* contours are the same at all spatial locations within the simulation box at a given redshift, so the resulting behavior is simpler to understand. The corresponding contours for both C II and C IV move to higher overdensity by almost a factor of 10 from  $z = 8 \rightarrow 5$ , owing to the ionization parameter  $U$  increasing.  $U$  is defined in this paper as the number density of photons capable of ionizing to a particular state (e.g. ionizing C III to C IV) divided by the number density of a particular atomic species (carbon in this case).  $U$  increases  $\sim \times 10$  because the physical densities decline by a factor of 3.4 from Hubble expansion, and the ionization intensity increases by  $\sim \times 3$  between  $z = 8 \rightarrow 5$ . C II evolves to trace a smaller fraction of phase space at higher densities; however the metal density is greater at these higher densities and at later times, so the total amount of C II is expected to be fairly stable from  $z = 8 \rightarrow 5$ . The contours extending to higher densities at  $T \sim 10^5$  K in Figure 7 correspond to C IV in collisional ionized equilibrium (CIE). This overlaps few metals, because C IV is an efficient coolant and SPH particles evolve rapidly through this region, much like we find for O VI at  $z < 0.5$  (Oppenheimer & Davé 2009).

As most IGM metals remain near  $T = 10^4$  K, we plot the C II/C and C IV/C ionization fractions ( $f(\text{C II})$ ,  $f(\text{C IV})$ ) at this temperature in Figure 8 (top panels), showing the *HM2001* curves moving upward in overdensity by the factor

of 10 from  $z = 8 \rightarrow 5$ . C IV should dramatically increase as the  $z = 8$  field is too weak to ionize C IV, while by  $z = 5$  the gray and C IV contours move to overlap as more metals enrich lower overdensities while  $U$  increases. A second effect illustrated in Figure 8 is that the maximum  $f(\text{C IV})$  grows as a result of the harder background with more quasar contribution at  $z = 5$  relative to  $z = 8$ ; more photons exist at the ionization potential of C III (47.9 eV or 259 Å) to create C IV relative to the C I potential (11.3 eV or 1101 Å) to make C II, resulting in a larger density range where C IV resides. We define and plot in Figure 8 (bottom panel) the ratio  $J_{259\text{Å}}^\circ / J_{1101\text{Å}}^\circ$ , which we call the “carbon spectral ratio”. This has significant implications for C II and C IV observations. The carbon spectral ratio is  $200\times$  greater for the *Bubble* versus the *HM2001* field at  $z = 8$ .

We now focus on the *Bubble* field behavior. The example fields signified by the right panels in Figure 7 demonstrate the expected ionization in  $\rho - T$  phase space at 10 physical kpc from a  $10^7 M_\odot$  galaxy. These contours shift right as  $M_*$  increases and left as  $d_{gal}$  increases due to the inverse square law; e.g. the contours are equivalent to the ionization field from a  $10^9 M_\odot$  galaxy at 100 kpc. We choose this field strength because this is the representative of where our simulated metals typically reside. Like the *HM2001* field, our implementation of the *Bubble* field depends on only two variables:  $U$  and  $T$ . The difference is that  $U$  depends on a combination of density, stellar mass, and galaxy distance.

If we consider the *Bubble* case shown in Figure 7 at  $z = 8$ , there exists moderate overlap with the metal contours between  $1 - 10\times$  mean overdensity, which are reasonable densities at 10 physical kpc from our simulated  $10^7 M_\odot$  galaxies. But note that the calculated incidence of intersecting at least this close to one of  $332 M_* \geq 10^7 M_\odot$  galaxies in the d16n256vzw box is  $0.22\Delta z^{-1}$ , so a high- $z$  quasar spectrum would be lucky to intersect one such region. The contours move to higher overdensity for larger galaxies (or at closer distances), but these are even less likely. Meanwhile, by  $z = 5$ , the space density of  $M_* \geq 10^7 M_\odot$  galaxies is  $\times 8$  higher and more metals have enriched IGM overdensities while the ionization contours have not evolved too much. This is why we obtain an increase in C IV absorption from  $z = 8 \rightarrow 5$ , as we show in §5.2.2.

The greater carbon spectral ratio in the *Bubble* field leads to greater  $f(\text{C IV})$  at photo-ionized temperatures, as shown in Figure 8. At  $T = 10^4$  K,  $f(\text{C IV})$  maximizes at 0.67 at  $z = 8$  and extends over 3.2 decades of density where  $f(\text{C IV}) \geq 0.1$ , compared to  $f(\text{C IV}) = 0.27$  and 1.6 decades with  $f(\text{C IV}) \geq 0.1$  for the *HM2001* field. The *Bubble* hardness declines as stars age and grow more metal rich by  $z = 5$ , (maximum  $f(\text{C IV}) = 0.57$ ), and rises for *HM2001* as the quasar density increases ( $f(\text{C IV}) = 0.37$ , cf. the carbon spectral ratio evolution in the bottom of Figure 8). The greater *Bubble* hardness allows significantly more C IV, especially at the highest redshifts we explore. Simcoe (2006) also finds  $f(\text{C IV})$  increases at  $z > 4.5$  at  $\rho/\bar{\rho} = 10$  when the dust attenuated flux from a  $10^8 M_\odot$  galaxy at 100 kpc is included. In the end, this results in less evolution for C IV absorption in the *Bubble* model relative to *HM2001*, as we show in §5.2.2. Our *Bubble* evolution is greater than the Simcoe (2006) example, because the metals are 5-50 kpc from ionizing galaxies.

A key point applicable to all metal-line IGM observa-

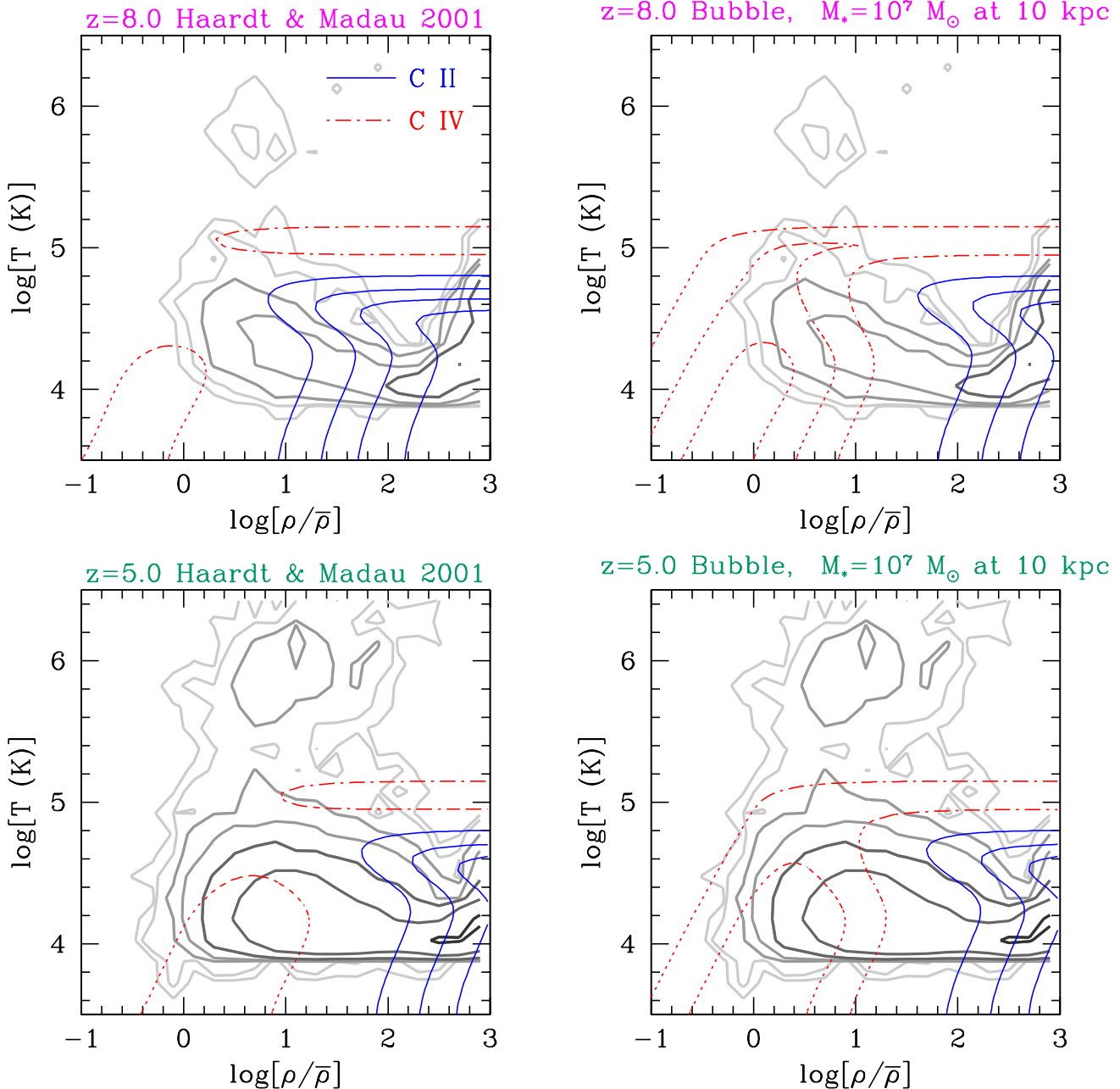


**Figure 7.** Metal phase space plots: Colored contours (solid blue for C II and red dot-dashed for C IV) correspond to the ionization fractions, while thick gray contours indicate the metal distribution in phase space. Overlapping regions give rise to absorption in that ion. The left panels assume the uniform Haardt & Madau (2001) background, and the right panels use the local ionizing *Bubble* field arising 10 kpc from a  $10^7 M_{\odot}$  galaxy; the contour spacings correspond to ionization fraction steps of 20% (i.e.  $f(\text{C IV}) = 0.2, 0.4$ , etc.). The gray metallicity contours are in logarithmic steps of 0.5 dex. At  $z = 8$  (top panels), C II should trace metals better than C IV for the *HM2001* field, while by  $z = 5$  (bottom panels) C IV should become a better tracer of metals in the diffuse IGM. The *Bubble* contours depend on galaxy size and distance: Contours move right as  $M_*$  increases and left as  $d_{gal}$  increases (i.e.  $U \propto M_* d_{gal}^{-2}$ ). C IV is always a good tracer of IGM metals from  $z = 8 \rightarrow 5$  in the *Bubble* case.

tions is that while it is well known that taking ratios of different photo-ionized species can determine spectral hardness (e.g. Schaye et al. 2003; Aguirre et al. 2004, 2008), a single species' ionization correction alone can vary dramatically due to the spectral shape. It is risky therefore to assign a fiducial ionization correction, especially considering we know so little about the ionization background for high-ionization species; as a result, an observable such as  $\Omega(\text{C IV})$

could easily change by a factor of a few, as we stress in §5.2.3.

To visualize the spatial distribution of metal absorbers, we illustrate the absorption column densities in two-dimensional maps of the  $25 \text{ km s}^{-1}$  slices in the bottom panels of Figures 5 assuming a uniform *HM2001* background. C II is confined to overdense regions close to galaxies, while C IV is a more capable tracer of the IGM volume enriched,

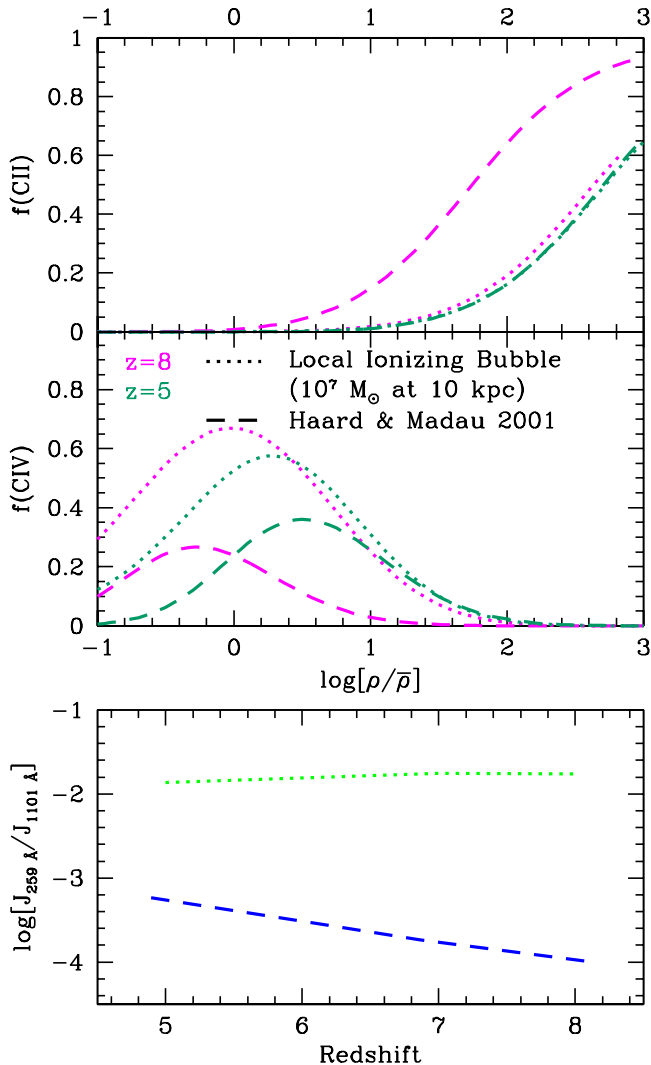


**Figure 8.** *Top panels:* C II (upper) and C IV (lower) ionization fractions as a function of overdensity at  $T = 10^4$  K for the *HM2001* (dashed lines) and *Bubble* (dotted lines) at  $z = 8$  (magenta) and  $z = 5$  (green). The *HM2001* field evolves more as quasars provide increasing intensity above 47.9 eV at later times. The *Bubble* field shows less evolution, and generally C IV traces lower overdensities. *Lower panel:* The mean carbon spectral ratio  $\equiv J_{259\text{\AA}}/J_{1101\text{\AA}}$  for our two ionization fields as a function of redshift. The star forming galaxy-dominated *Bubble* field is significantly harder than the *HM2001* field with quasars, because *HM2001* is dominated by galaxies at high- $z$  and the attenuation above 47.9 eV is greater than the *Bubble* attenuation due to dust. This results in overall lower values for  $f(\text{CIV})$  in the *HM2001* case.

albeit mostly at column densities that are below current observational limits. The scarcity of pink in the bottom right frame indicating column densities similar to those observed by Ryan-Weber et al. (2006) and Simcoe (2006) indicates just how rare detectable C IV is.

We demonstrate evolution using a zoom-in to the second most massive galaxy in our box in Figure 9. This visualization shows the evolution of the surrounding  $4 \times 4 h^{-1} \text{Mpc} \times 25 \text{ km s}^{-1}$  region using the same scales as Figure 5. A clear bipolar outflow emanates perpendicularly to a filament feeding the growth of a  $M_* = 10^9 M_\odot$  galaxy (at  $z = 6$ ).

Strong C II absorption traces the overdense regions around the galaxy at all epochs, while C IV evolves to trace the extended IGM enrichment; observed C IV evolves faster than C II between  $z = 8 \rightarrow 5$ . The smaller galaxies in the bottom right of this frame,  $M_* \sim 10^{7-8} M_\odot$ , are the most prolific IGM enrichers at high- $z$  due to their large numbers and high mass loading factors.

## 5 OBSERVATIONAL PREDICTIONS

Observations of the high- $z$  IGM are leaping forward with the advent of near-IR spectroscopy, along with the discovery of quasars at  $z > 6$ , with an eye to the tantalizing possibility of using gamma-ray bursts (GRBs; Kawai et al. 2006) to briefly illuminate IGM absorbers at very high redshifts. We present here predictions for high- $z$  metals line transitions occurring redward of Ly $\alpha$ , where the quasar continuum is free of H I absorption. We consider five species already observed at  $z \geq 5$  with rest wavelengths ( $\lambda_0$ ) redward of Ly $\alpha$ : C II (1334.5 Å), C IV (1548.2, 1550.8 Å), O I (1302.2 Å), Si II (1260.4 Å), and Si IV (1393.8, 1402.8 Å) at our four chosen redshifts:  $z = 8, 7, 6$ , and 5. Three ionization fields introduced in §4.1 are considered: *No Field*, *HM2001*, and *Bubble*.

We use our quasar absorption line spectral generator *specexbin* (see §2.5 of OD06 for details) to produce continuous angled LOSs through our simulation volume, each covering  $\Delta z = 0.9$  for each of the four redshifts. We make an “ideal”-quality sample of 70 LOSs, assuming a high  $S/N$  ratio of 50 for each  $R = 50,000$  resolution element, and a moderate instrumental resolution of  $15 \text{ km s}^{-1}$ . This is comparable to what is achievable on current optical spectrographs on 8 – 10 meter class telescopes, which can trace C II out to  $z \sim 6.5$  (e.g. BSRS). At higher redshifts, near-IR data will be required. The current generation of near-IR spectrometers have resolutions of  $R = 5000 - 10,000$  and a  $S/N = 10 - 20$  per resolution element for  $z \sim 6$  quasars (R. Simcoe, private communication). The next generation should achieve  $R = 20,000$  with much higher  $S/N$  using 20-30 meter class telescopes, e.g. the near-Infrared Multi-Object Spectrograph (IRMOS) on the Thirty Meter Telescope (TMT) (Eikenberry et al. 2006). Our simulated spectra can be used both to compare to current optical spectra, as well as make predictions for future instruments.

We first consider column density distributions for three of the five ionization species. We fit Voigt profiles using the automated fitter AutoVP (Davé et al. 1997), generally with little uncertainty since metal lines are typically unsaturated and unblended. Then we sum column densities into a cosmic mass density as a function of redshift for each species. We present predictions for equivalent widths next, for comparisons with large samples of  $z > 6$  metal absorbers that may be obtained in the near future. We then consider some simple absorber ratios, emphasizing what can be inferred about the ionizing conditions. Lastly, we show some sample absorption line profiles and explain the velocity profiles of systems. Along the way, we compare to published  $z \gtrsim 5$  metal absorber data, and offer some interpretations based on our models. We consider the observed completeness limits assuming  $S/N=10$  and 20 per resolution element at  $R = 5000$ , and we confirm that the results we show in our high quality spectra hold at lower resolution and  $S/N$ .

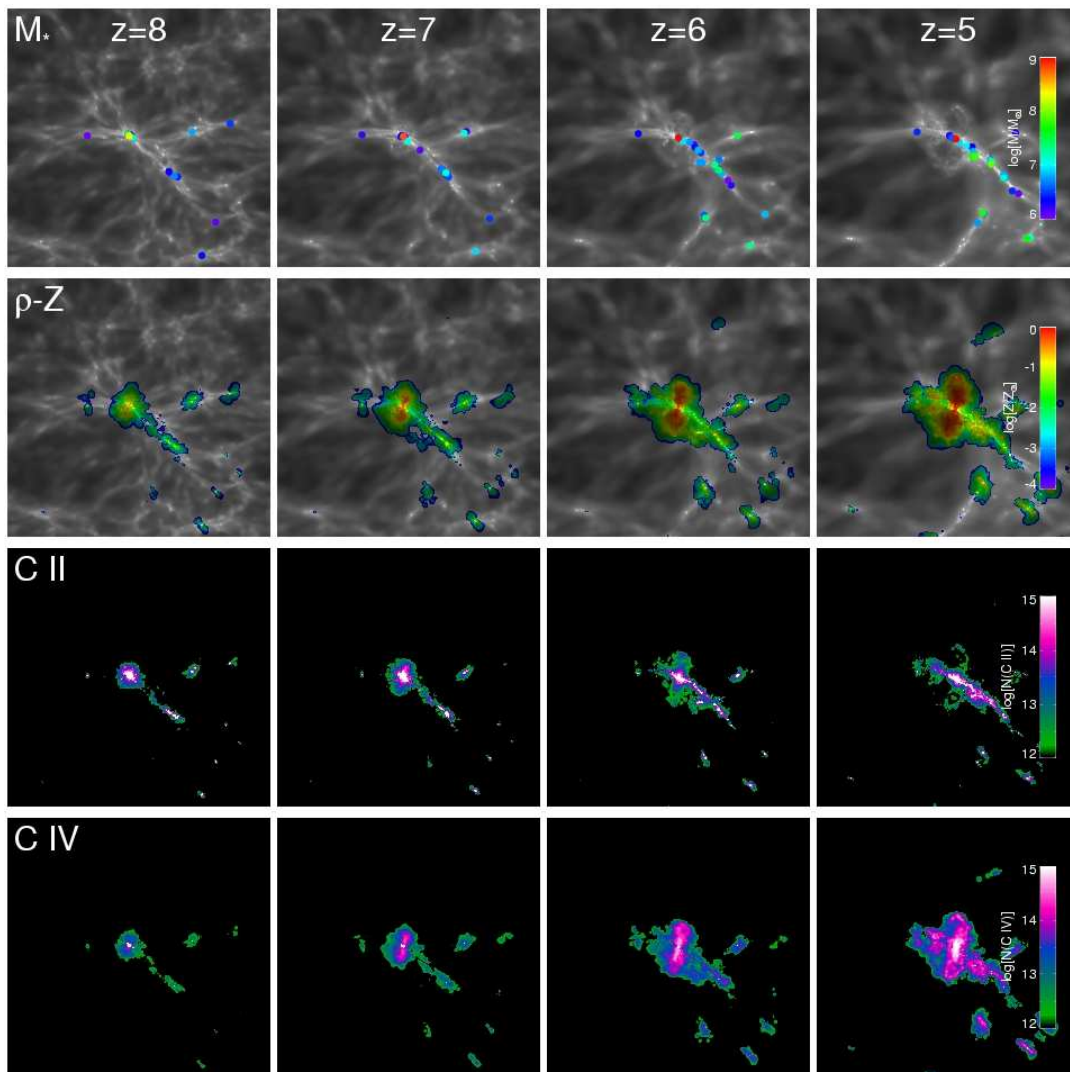


**Figure 9.** The evolution of a  $4 \times 4h^{-1}\text{Mpc} \times 25 \text{ km s}^{-1}$  slice, centered on a galaxy that grows from  $2.4 \times 10^8 M_{\odot}$  to  $1.8 \times 10^9 M_{\odot}$  from  $z = 8 \rightarrow 5$ . The global metal volume filling factor increases by  $\sim \times 10$  from  $z = 8 \rightarrow 5$ , but this slice shows less growth owing to early enrichment from the massive galaxy at the center. C II traces higher overdensities in the proximity of galaxies, while C IV evolves to trace the more diffuse IGM by  $z = 5$ , including the bipolar outflow.  $M_{*} = 10^{7-8} M_{\odot}$  galaxies such as those in the bottom right of the frame represent the most prolific enrichers of the  $z = 6$  IGM, since they exist in greater numbers and have higher mass loading factors. Visit <http://luca.as.arizona.edu/~oppen/IGM/hiz.html> for simulation movies.

### 5.1 Column Density Distributions

The column density distribution (CDD),  $d^2n/dXdN(\text{ion})$ , is the most basic metal absorber counting statistic. Here  $n$  is the number of lines with column density between  $N(\text{ion})$  and  $N(\text{ion})+dN(\text{ion})$ , and  $dX$  is absorption pathlength. Following general practice among observers, we sum together all individual Voigt profile *components* within  $100 \text{ km s}^{-1}$  of each other into *systems*. This minimizes differences due to vagaries of Voigt profile fitting, and allows more straightforward comparisons among data sets with varying resolution and signal-to-noise. For  $dX$  we use

$$X(z) = \frac{2}{3\Omega_M} \sqrt{\Omega_M(1+z)^3 + \Omega_{\Lambda}}. \quad (5)$$

$dX$  for our adopted  $\Omega_M = 0.25$  cosmology is almost double that in an Einstein-deSitter universe (the  $\Omega_{\Lambda}$  term is negli-

gible at these redshifts). We scale other observations to our assumed cosmology where necessary.

Figure 10 shows CDDs for oxygen and carbon using different choices for the ionizing field at  $z = 8$  (left) and  $z = 6$  (right). The first ion considered is O I in the top panels, which has a unique association with H I because these two species remain in charge-exchange equilibrium (Osterbrock 1989) due to their neutral ionization potentials being only 0.15% apart in energy. Oh (2002) and Furlanetto & Loeb (2003) hypothesize the existence of an ‘‘O I forest’’ tracing the neutral metals that have enriched dense IGM regions via early enrichment. Higher ionization states easily recombine at the high densities of the early Universe. Dozens, even hundreds of lines with  $N(\text{O I}) > 10^{14} \text{ cm}^{-2}$  should be detectable if the IGM is neutral and enriched with a large filling factor of metals, but BRS find very few O I lines. No O I systems

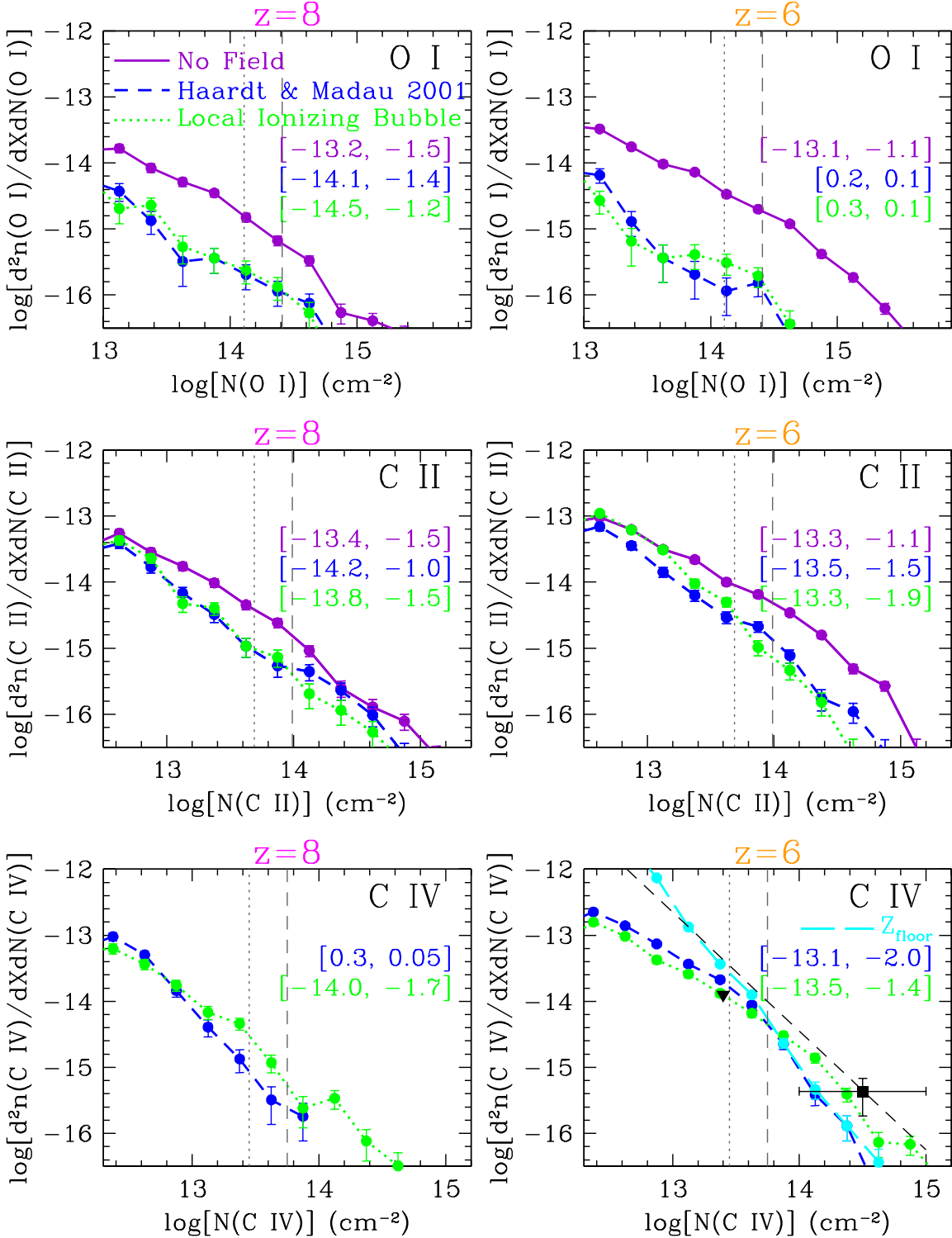


**Figure 10.** Predicted differential column density distributions for O I, C II, and C IV systems at  $z = 8$  (left) and  $z = 6$  (right), for our three ionization field cases. 50% detection thresholds are indicated by gray lines for  $S/N = 10$  (dashed) and 20 (dotted) per resolution element in an  $R = 5000$  spectrum. The two values on the right side of each panel are  $\log[B]$  and  $\alpha$  from Equation 6 if both numbers are negative, or if there are too few lines for a power law fit the line frequencies per  $\Delta z$  in the lower and upper column density bins if both numbers are positive. O I (upper panels) shows frequent strong lines and a shallow decline toward high  $N(\text{O I})$  if all oxygen is neutral, while significantly less arises in the ionized cases. C II, middle panels, is assumed to have no ionization correction in the *No Field* case, showing much the same CDDs as neutral O I. C II is more prevalent in the *Bubble* than O I due to this state's higher ionization potential. C IV, bottom panels, shows more strong absorbers for the *Bubble* field, while the *HM2001* uniform field predicts much stronger evolution. The long dashed cyan CDD at  $z = 6$  is the case where a metallicity floor of  $Z = 10^{-3} Z_{\odot}$  is added, resulting in appreciably more lines below  $10^{13.5} \text{ cm}^{-2}$ . The black square in the bottom right panel correspond to the total number of components (3) with  $N(\text{C IV}) = 10^{14.2-15.0} \text{ cm}^{-2}$  in the combined sample of Becker et al. (2009) & Ryan-Weber et al. (2009) over a pathlength of  $\Delta X = 27.4$ . The black upside-down triangle is the upper limits from the Becker et al. (2009) null detection at  $N(\text{C IV}) = 10^{13.4} \text{ cm}^{-2}$

above  $10^{15} \text{ cm}^{-2}$  are found either, despite such predictions by Oh (2002).

Our *No Field* case (upper panels of Figure 10) shows that O I lines should be common at  $z = 8$ , despite our metal filling factors being under 1%. We predict line frequencies of 1.9 and  $0.6 \Delta z^{-1}$  for  $10^{14} \leq N(\text{O I}) < 10^{15} \text{ cm}^{-2}$  and  $10^{15} \geq N(\text{O I})$  respectively at  $z = 8$ . The corresponding frequencies rise to 5.4 and  $1.9 \Delta z^{-1}$  by  $z = 6$ . O I provides the clearest contrast of any species between a neutral and ionized IGM; the *Bubble* field yields frequencies of 0.4 and  $0.3 \Delta z^{-1}$  above  $N(\text{O I}) = 10^{14} \text{ cm}^{-2}$  at  $z = 8$  and 6 respectively. This clear contrast may already have been observed by BSRs, as all of their O I absorbers detected at  $z > 6$  are along one of their three LOSs probing these redshifts. This could suggest a patchy reionization scenario (e.g. Furlanetto & Oh 2005; Iliiev 2006; Lidz et al. 2007) where individual LOSs probe large-scale structures at different ionization states.

We fit a power law of the form

$$d^2n/dXdN(\text{ion}) = B \times \left( \frac{N_{\text{ion}}}{N_0} \right)^\alpha \quad (6)$$

to the O I distribution by summing systems into two bins ( $N(\text{O I}) = 10^{13.7-14.45}$  and  $N(\text{O I}) = 10^{14.45-15.2} \text{ cm}^{-2}$ ) and finding the best-fit line. We list  $\log[B]$  and  $\alpha$  for each CDD in Figure 10 if there are at least 10 systems in each bin; otherwise we list system frequencies per  $\Delta z$  of the lower and upper bins (positive numbers). We set  $N_0 = 10^{13.0} \text{ cm}^{-2}$  for the normalization. The *No Field* O I  $z = 6$  CDD has  $\alpha = -1.1$  over these column densities, which translates to 85% as many systems in the upper O I bin compared to the lower bin. A power law where  $\alpha > -2$  indicates more metals at higher column densities, meaning this power law must turn over so that the summed O I is finite. Power law slopes can yield information about the nature of the metallicity distribution and ionizing source, and provide an easy way to compare datasets to simulations. Not only does the *Bubble* field create fewer O I lines at every column density, it has a much steeper power law, which we cannot calculate accurately as there are too few absorbers in the higher bin. Oxygen and hydrogen are easily ionized out of their neutral states by any ionizing background above 1 Rydberg.

C II CDDs shown in the middle panels of Figure 10 recreate similar behavior to O I for the *No Field* case, but has a much higher frequency for the ionization field cases since the C I ionization potential lies below 1 Ryd, unlike O I. The  $z = 6$  frequency of the lines with  $N(\text{C II}) > 10^{14.0} \text{ cm}^{-2}$  is 4.5, 0.8, and  $0.4 \Delta z^{-1}$  for the *No Field*, *HM2001*, and *Bubble* fields, respectively. Furthermore, the slopes of the CDDs between  $N(\text{C II}) = 10^{13.2-14.7} \text{ cm}^{-2}$  may help constrain the ionization field, being  $\alpha = -1.1$ ,  $-1.5$  and  $-1.9$ , respectively. The *Bubble* field produces fewer strong C II lines than *HM2001*, because the metals at  $z = 6$  still reside close enough to the local ionizing source that carbon is ionized to higher states by the greater intensity above the Lyman limit.

C IV has a higher frequency of lines with  $N(\text{C IV}) \geq 10^{14.2} \text{ cm}^{-2}$  ( $0.9$  vs.  $0.2 \Delta z^{-1}$ ) and a shallower slope ( $\alpha = -1.4$  vs.  $-2.0$  over  $N(\text{C IV}) = 10^{13.0-14.5}$ ) for the *Bubble* field compared to the *HM2001* field in the bottom panels of Figure 10. There is no C IV in the *No Field* case, as shocks from structure formation rarely heat the gas to temperatures where C IV is collisionally ionized at these

early epochs. We plot a black square from the three observed C IV absorbers of Ryan-Weber et al. (2009) where  $N(\text{C IV}) = 10^{14.0-15.0} \text{ cm}^{-2}$  and include the additional pathlength from the SDSS J0002+2550 LOS observed only by Becker et al. (2009) (total  $\Delta X = 27.4$ ). We find an observed frequency of  $0.5 \pm 0.3 \Delta z^{-1}$  for these absorbers averaging  $\langle z \rangle = 5.75$ . To compare directly to our models, we (i) multiply the frequency of our C IV absorbers by the Ryan-Weber et al. (2009) sensitivity function (their Figure 6), and (ii) estimate the  $z = 5.75$  C IV frequency by taking a log-weighted average of our  $z = 6$  and 5 model frequencies, because strong C IV absorbers rapidly increase in number from  $z = 6 \rightarrow 5$  (especially for *HM2001*). Our  $N(\text{C IV}) = 10^{14.0-15.0} \text{ cm}^{-2}$  frequencies are 1.2 and  $0.4 \Delta z^{-1}$  for the *Bubble* and *HM2001* models respectively. The uniform field is consistent with the observed frequency, while the local ionizing bubble actually over-predicts strong C IV absorbers. We actually prefer the *Bubble* model, because we will argue IGM metals are not completely ionized and that a significant fraction of them are in lower ionization species, either recombined or shielded from UV flux.

We also plot the maximum allowed frequency of  $N(\text{C IV}) = 10^{13.4} \text{ cm}^{-2}$  systems from the null Becker et al. (2009) detection (upside-down triangle); this is the column density where they calculate they have 50% completeness. We appear to over-predict the amount of these weaker absorbers in either model, although by how much will have to wait for future observations. The long dashed cyan line is the case where a  $10^{-3} Z_\odot$  metallicity floor is added to the simulation; we discuss this more in §5.3. The fact that Becker et al. (2009) finds no weak C IV lines in the largest pathlength yet sampled at  $z > 5.5$  indicates a large volume of the IGM is not enriched much above  $Z > 10^{-3} Z_\odot$ .

For comparison with lower  $z$ , we plot Songaila (2001) power law fit to C IV absorbers at  $z = 2.90 - 3.54$ . There exists less C IV at all column densities in our simulations, which agrees with our reproduction of a declining  $\Omega(\text{C IV})$  at  $z > 5$  as we discuss next.

## 5.2 Metal Mass and Ion Densities

We now consider the summed mass densities as a way to illustrate the evolutionary differences between ionization fields. The evolution of C IV for the two fields differs since the weak *HM2001* field at  $z = 8$  is incapable of ionizing overdensities containing carbon up to C IV, creating very few strong absorbers, while the *Bubble* field has a harder spectrum early on (cf. red contours in upper panels of Figure 7).

An ion's global mass density may be obtained by integrating the total column density of their systems and dividing by pathlength, as follows:

$$\Omega(\text{ion}, z) = \frac{H_0 m_{\text{species}} \Sigma N(\text{ion}, z)}{c \rho_{\text{crit}} \Delta X(z)}. \quad (7)$$

where  $H_0$  is the Hubble constant,  $c$  is the speed of light,  $\rho_{\text{crit}}$  is the critical density of the Universe, and  $m_{\text{species}}$  is the atomic weight of the given species.

For comparison to the data, we count systems over two decades of column density chosen to correspond to the species' detectability. We count lines for C IV over  $N(\text{C IV}) = 10^{13.0-15.0} \text{ cm}^{-2}$ , and scale other species' column density range using the ratio of the oscillator strength

of a line ( $g$ , the strongest of a doublet) times its rest wavelength ( $g \times \lambda_0$ ) for the considered species versus that of C IV. For example, the range considered for O I works out to be  $N(\text{O I}) = 10^{13.7-15.7} \text{ cm}^{-2}$ , because the resulting C IV : O I ratio is 4.6; O I has a  $\times 3.9$  weaker oscillator strength and a  $\times 1.2$  smaller wavelength. O I is harder to observe due to its weaker oscillator strength, so the column densities considered are higher. Conversely, silicon species have high oscillator strengths, meaning that column densities below  $10^{13} \text{ cm}^{-2}$  are achievable for Si II ( $N(\text{Si II}) = 10^{12.4-14.4} \text{ cm}^{-2}$ ) and Si IV ( $N(\text{Si IV}) = 10^{12.6-14.6} \text{ cm}^{-2}$ ). The range for C II is  $N(\text{C II}) = 10^{13.2-15.2} \text{ cm}^{-2}$ . Nature creates a convenient conspiracy whereby greater oscillator strengths make up for lower Type II SNe yield abundances, leading to similarly strong lines for our five considered ionic species.

Error bars are calculated using the Storrie-Lombardi et al. (2005) method (their Equation 4), and do not include systematics such as cosmic variance. We also apply this error estimation method to the BSRs dataset, which results in much larger error bars than they published as a result of them including only the uncertainty in their summed column densities.

### 5.2.1 Low Ionization Species

The resulting  $\Omega$ 's for the five species and different fields are plotted in Figure 11. We also plot the total metal density of the corresponding element, summed by counting the gas phase mass of that species in the entire simulation box at the given redshift ( $\Omega(\text{species})$ , black dash-dot line).

With no ionization correction in the *No Field* case, the ions C II, O I, and Si II directly trace the increase seen in metal density of  $\sim \times 8$  from  $z = 8 \rightarrow 5$ . Note, however, that the ion density should be identical to the metal density if absorption lines of all column density are counted, yet the ion density is  $\times 4 - 6$  less than the metal density. Where are the unaccounted metals? The answer is that since the CDDs have slope  $\alpha > -2$ , they are in high-column systems that are extraordinarily rare. Hence using a volume-weighted method as quasar LOSs to obtain a handle on a mass-weighted quantity such as ion density is challenging, more so for low ionization species, which preferentially trace high overdensities.

The  $\Omega(\text{O I})$  determined by BSRs favors the *No Field* case over either ionization field, considering their sample from  $z > 6.2$  quasars. This suggests that at least some of the  $z \sim 6$  metal-enriched IGM is neutral. That BSRs found four O I systems (all with  $N(\text{O I}) > 10^{13.7} \text{ cm}^{-2}$ ) toward SDSS J1148+5251 and not more than one in any of the other 8 high- $z$  LOSs; this is unlikely to be a statistical fluctuation (0.18% chance according to BSRs). The *No Field* case produces a frequency of  $9.2 \Delta z^{-1}$  of such O I lines, which is in agreement with the J1148 LOS and at least  $\times 20$  higher than either of our simulated ionization fields. Hence our simulations agree with BSRs's interpretation that the J1148 LOS possibly probes a long stretch of IGM with incomplete reionization, while the other LOSs of BSRs are consistent with being completely reionized. How one obtains a relatively neutral LOS along the 200 comoving Mpc spanned by the J1148 LOS while most LOSs are reionized is not easy to understand, but we cannot address this directly with our

current simulations owing to lack of volume. If reionization proceeds across such metal-enriched regions extending below  $z = 6$ , a dramatic decline in  $\Omega(\text{O I})$  is expected by  $z = 5$ .

The *No Field* case is barely favored by the  $\Omega(\text{Si II})$  data of BSRs, but  $\Omega(\text{C II})$  appears closer to predictions of an ionized IGM. The fact that observed C II, Si II, and O I arise together with similar profile shapes suggests that each of these ionic species may be dominant, consistent with the *No Field* assumption. If so, the lack of consistency among the three low ions may be a result of metal yields differing those of Chieffi & Limongi (2004) we employ, which is one reason we provide alternative yields in Table 1.  $\Omega(\text{C II})$  and  $\Omega(\text{Si II})$  show less difference between the *No Field* and two ionizing cases than  $\Omega(\text{O I})$  in Figure 11, because the first two species have higher ionization potentials that are not as easily ionized by the addition of a field.

Overall, the low ionization species paint a scenario in which there are still significant patches of neutral IGM gas at  $z \sim 6$  along at least some LOSs. Hence in principle one could use such ions to trace the patchiness of reionization. We plan to investigate this possibility using simulations that more accurately track the ionization field using radiative transfer (Finlator et al. 2009).

### 5.2.2 High Ionization Species

$\Omega(\text{C IV})$  has been measured in several studies at  $z > 4.5$ , with differing results. Songaila (2001) finds  $\Omega(\text{C IV})$  is consistent with remaining constant from  $z = 2 \rightarrow 5.5$ , which was extended by the measurements of Simcoe (2006) out to  $z = 5.4 - 6.2$ . Conversely, the null detections by Becker et al. (2009) of C IV in the highest  $S/N$  data at  $z = 5.3 - 6.0$  supports a significantly declining  $\Omega(\text{C IV})$  at  $z > 4.5$ . The measurements of Ryan-Weber et al. (2009) over the largest pathlength ( $\Delta X = 25.1$ ) centered at  $\langle z \rangle = 5.76$  also finds a similar  $\Omega(\text{C IV})$  value.

Exploring a range of wind models, OD06 explained the near constancy in  $\Omega(\text{C IV})$  at  $z = 2 - 4.5$  by a decreasing global ionization fraction of C IV counterbalancing the increasing enrichment of the IGM. Therefore, the stability of  $\Omega(\text{C IV})$  does not indicate that the IGM must be enriched at  $z > 6$ . Instead, the ionization fraction decreases with time for several reasons: (i) Decreasing physical densities due to Hubble expansion, and (ii) the increasing *HM2001* ionization field strength from  $z = 5 \rightarrow 2$  result in C IV tracing higher overdensities and less of the carbon in the diffuse IGM; while (iii) increasing energy input into the IGM primarily from galactic outflows at later times push metals to hotter temperatures where C IV does a poor job of tracing carbon (see Oppenheimer et al. (2007) for a simple breakdown of this evolution).

OD06 predicted  $\Omega(\text{C IV})$  rises by a factor of two from  $z = 6 \rightarrow 4.5$  using the *HM2001* field, although the new cosmology we now use with a reduced  $\sigma_8$  significantly curtails high- $z$  SF resulting in a greater rise that agrees better with Becker et al. (2009) and Ryan-Weber et al. (2009). Figure 11 shows that  $\Omega(\text{C IV})$  continues this growth trend between  $z = 8 \rightarrow 5$ , for both ionization fields we consider. For the *HM2001* field, the C IV ionization correction falls by a factor of 10 (from 220 to 21) between  $z = 8 \rightarrow 5$ . This is a stunning drop and occurs because of the ionization behavior explored in §4.2: the uniform background grows stronger while phys-

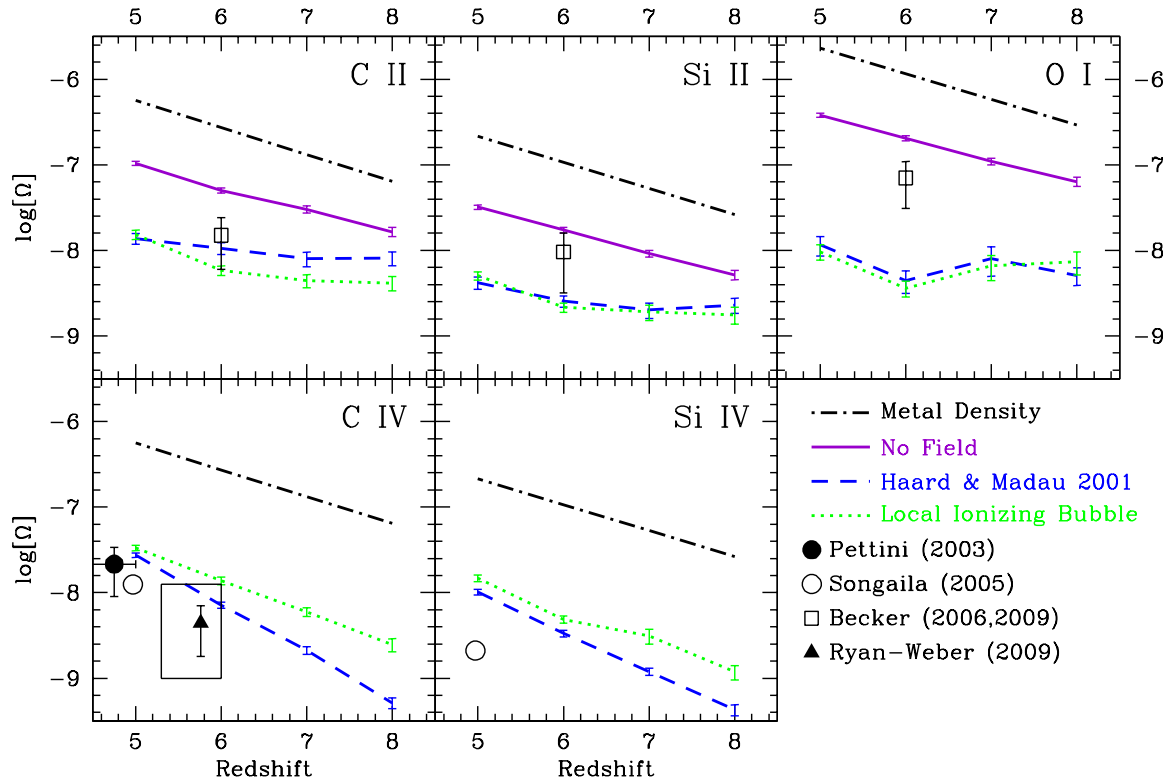


**Figure 11.** The evolution of the global ion mass densities, determined from simulated quasar LOSs for the three ionization cases, compared to the metal density summed for the corresponding atomic species calculated by summing over all the SPH particles in the simulation box; the difference between the two represents a global ionization correction for that ion. We sum absorbers over 2 decades of column density corresponding to the range the given transition is observable and unsaturated. The *No Field* case assumes no ionization correction, but falls below the total metal density because most of the absorption lies in extremely rare saturated lines, which are not in the included column density range when summing  $\Omega$ . The observations of BSRs in quasars at  $z > 6.2$  appear to favor a partially neutral IGM. Most C IV observations cannot distinguish between the *HM2001* and *Bubble* models, although the rapid evolution observed by Becker et al. (2009) and Ryan-Weber et al. (2009) at  $z > 5.3$  relative to  $z < 4.5$  supports the former.

ical densities decline resulting in a greater ionization parameter allowing metals to be ionized to C IV by  $z = 5$ . In essence, some of the same trends that cause the C IV ionization correction to increase from  $z = 5 \rightarrow 2$  (OD06), cause it to decrease from  $z = 8 \rightarrow 5$ .

The *Bubble* model predicts a slower evolution in  $\Omega(\text{C IV})$  at  $z > 4.5$ , because this field does not evolve as much as the *HM2001* uniform field. Metals around galaxies are ionized by a nearly unevolving field between  $z = 8 \rightarrow 4$ , so an increase of  $\Omega(\text{C IV})$  is more likely to reflect an actual increase in IGM metallicity near galaxies. From  $z = 8 \rightarrow 5$ ,  $\Omega(\text{C IV})$  increases by  $\times 14$  while  $\Omega(\text{C})$  increases by  $\times 9$ . As future  $\Omega(\text{C IV})$  observations achieve higher redshift above 6, we predict to see a decline corresponding to the evolution in the global metal density if the *Bubble* field is correct. Meanwhile, the physical and ionization conditions make  $z \sim 4 - 6$  the ideal time for C IV to trace metals in the IGM for either field, as the ionization correction reaches a minimum at these epochs.

$\Omega(\text{Si IV})$  mirrors the behavior for  $\Omega(\text{C IV})$  for the two fields we consider, with smaller differences. The lower ionization potential of Si III causes Si IV to trace higher overdensities, which can track some of the metals already injected into the IGM at  $z = 8$  with the *HM2001* field. The evolution of  $\Omega(\text{Si IV})$  is nearly identical to that of  $\Omega(\text{C IV})$  for the *Bubble* field for the reasons mentioned above.

The trends in our simulated high-ionization  $\Omega$ 's appear consistent with those that are observed. Our predicted  $\Omega(\text{C IV})$  values with either ionization field over-estimates the most recent observations at  $z > 5.3$ ; however we argue that not all metals are ionized by such a field, and that the observed value falling between the extremes of the *Bubble* field and the *No Field* case (i.e. no  $\Omega(\text{C IV})$ ) is encouraging.

### 5.2.3 Systematic Uncertainties in $\Omega(\text{C IV})$

While the above agreement with  $\Omega(\text{C IV})$  data for our ionizing field models is nice, it is worth pointing out that there are many possible systematics in the modeling that can impact predictions. Here we point out some of the ways our predictions of  $\Omega(\text{C IV})$  may be uncertain.

**Ionization background:** Besides the possibility that not all metals are ionized, there is the uncertainty about the nature of the ionization field where it exists. The intensity of the ionization background at the C III ionization potential is unobservable and uncertain, yet is vital for the correct determination of the C IV ionization correction, as we stress in §4.2. The carbon spectral ratio of the *Bubble* field makes  $\Omega(\text{C IV})$  higher than the *HM2001* field; in fact, the *Bubble* field produces a nearly optimally high value of  $\Omega(\text{C IV})$  at  $z = 6$ . On the other hand, Madau & Haardt (2009) notes

that reprocessing of radiation between 3 and 4 Ryd by resonant line absorption of the He II Lyman series could reduce by  $>\times 2$  the photons capable of ionizing C III to C IV. Becker et al. (2009) suggests this could be an explanation for the strong evolution they find in  $\Omega(\text{C IV})$  ( $\times 4.4$  increase between  $z = 5.3 - 6.0$  and  $z = 2.0 - 4.5$ ) if He II reionization proceeds over this redshift range, increasing C III ionizing radiation, and resulting in a lower ionization correction for C IV at  $z < 4.5$ .

**Wind model:** While we have investigated a plausible wind model for enriching the IGM, based on momentum-driven wind scalings, this may not be the only possible outflow scenario that can reproduce observations. Varying wind speeds and mass loading factors in OD06 led us to some useful intuition when compared to C IV absorption data: too high wind speeds overheat the IGM while too low wind speeds do not sufficiently enrich filaments; also, too high mass loading suppresses SF so much that too few metals are produced while too low mass loading results in insufficient metals in the IGM. But while constraints at  $z \lesssim 5$  are fairly tight, at higher  $z$  the possibility of more exotic processes such as Pop III stars or the lack of dust may impart fundamental changes to outflows. Without a more detailed physical understanding of the physics of outflow driving, it is difficult to ascertain the systematic uncertainties in our wind model.

**Mini-halos and Population III stars:** The very first stars and galaxies are not resolved in our simulation, as they likely form within mini-halos having virial temperatures below  $10^4\text{K}$  (e.g. Abel et al. 2002). If such systems dominate the early enrichment or ionization budget, our modeling will be incomplete. However, Wise & Abel (2008) suggests that they do not dominate the ionization budget, and Bromm et al. (2004) estimated that they increase the global gas metallicity by only  $\sim 10^{-4} Z_{\odot}$ , which is  $\times 30$  less than the global gas metallicity at  $z = 6$  in our simulations. Hence unless they have much higher yields than expected, it seems unlikely that metal production in mini-halos should be important at  $z = 5 - 8$ .

**Unresolved galaxies:** For galaxies in halos with virial temperatures above  $10^4\text{K}$ , our simulation nearly resolves the Jeans mass at  $z \lesssim 10$ . Using the formula for Jeans length from §6 of OD06, we find a Jeans mass of  $9 \times 10^7 M_{\odot}$  at  $z = 10$  assuming  $\delta = 50$  and  $T = 10^4\text{K}$ , which is nearly the dynamical mass limit of a resolved galaxy in our simulation. The flattening of the stellar mass function at  $M_* \lesssim 10^7 M_{\odot}$  reflects the effect of the photoionization of regions containing forming galaxies (i.e. the filtering mass). For this reason, our resolution-converged fit to the stellar mass function (Equation 3) suggests that we are not missing a large population of lower mass galaxies in the d16n512vzw box.

**Yields:** Another uncertain factor that could alter  $\Omega(\text{C IV})$  is the SNe yields. We use the yields of Chieffi & Limongi (2004), which do not change much at low- $Z$  for carbon. In our simulations the SFR efficiency is so high in early galaxies that the average stellar metallicity in star particles reaches  $0.1 Z_{\odot}$  by  $z = 7$ , which minimizes the importance of low- $Z$  yields. It has been suggested, however, that patches of low-metallicity SF persist to late epochs (e.g. Tornatore et al. 2007; Cen & Riquelme 2008), which if true means our simulations are over-mixing metals. Integrating the carbon yields over the various stellar IMFs listed in Ta-

ble 1 does indicate as much as a factor of two difference with the yields we use at the higher end. Note also that the yields calculated by Hirschi (2007) for rotating stars at solar metallicity can more than double the total carbon yield versus non-rotating models.

**Initial mass function:** Even if metal-free stars are unimportant, it is possible that there is an overall shift towards a more top-heavy IMF at high redshifts. Davé (2008) finds the evolution in the  $M_*$ -SFR calibration could be explained by an increasingly top-heavy IMF from  $z = 0 \rightarrow 2$ , which suggests very few low-mass stars if extrapolated to  $z \sim 6$ . Tumlinson (2006) presents constraints indicating a top-heavy IMF at early epochs that explain the frequency of Galactic carbon-enhanced metal poor stars<sup>4</sup>. IMF variation concerns are mitigated in large part by noting that our simulations match the observed UV LF, which indicate that they are producing roughly the correct number of massive stars. Hence to first order the amount of carbon produced will be correct. But depending on the nature and form of an IMF variation, it remains possible that the overall carbon yield per unit high-mass SF could still vary somewhat. As an example, the Portinari et al. (1998) yields using a contribution only from 30-120  $M_{\odot}$  stars produces half as much carbon as the Chieffi & Limongi (2004) yields (Table 1).

**Cosmological parameters:** Given the uncertainties on cosmological parameters in the 5-year WMAP results Hinshaw et al. (2008), the measurement of  $\sigma_8$  ( $0.820 \pm 0.028$ ) imparts the greatest uncertainty in regards to high- $z$  SF. As mentioned in §3.1, the primary difference causing the factor of two increase in stellar mass density at  $z = 6$  in the w-series used in DFO06 over the d-series used here is  $\sigma_8$  (0.90 compared to 0.83). Similarly, we find  $\times 1.8$  fewer  $z = 6$  stars in a  $16h^{-1}\text{Mpc} \times 2 \times 256^3$  test run where we reduce  $\sigma_8$  from 0.83 to 0.75 holding all other parameters constant. Given the error bars on  $\sigma_8$ , a factor of two difference in SF and chemical nucleosynthesis at  $z \geq 6$  is possible, which will lead to similar uncertainty in  $\Omega(\text{C IV})$  if the metals are injected into the IGM the same way. This is the main reason why the d-series results in a larger increase in  $\Omega(\text{C IV})$  from  $z = 6.0 \rightarrow 4.5$  compared to the published w-series predictions in OD06.

To summarize, a number of possibilities exist to alter  $\Omega(\text{C IV})$  by a factor of a couple. An important constraint is the number of weaker lines ( $N(\text{C IV}) < 10^{14} \text{cm}^{-2}$ ), which our models may be over-predicting given the comparison to the largest sample from Becker et al. (2009) that can detect such absorbers at  $z > 5.3$ ; this could be a sign that superwinds have a smaller filling factor in the IGM than our simulations predict, or that more diffuse metals are less ionized (see §6.3.2). Lower carbon yields, possibly from a top-heavy IMF, could potentially lower  $\Omega(\text{C IV})$ , while a different ionization background is more likely also to decrease  $\Omega(\text{C IV})$  compared to the *Bubble* field. The determination of  $\sigma_8$  also can potentially alter  $\Omega(\text{C IV})$  by a factor of two. The good agreement seen in  $\Omega(\text{C IV})$  evolution should be taken as an encouraging but not definitive demonstration of the validity of our models.

<sup>4</sup> This itself is not a carbon yield constraint, and only an IMF constraint.

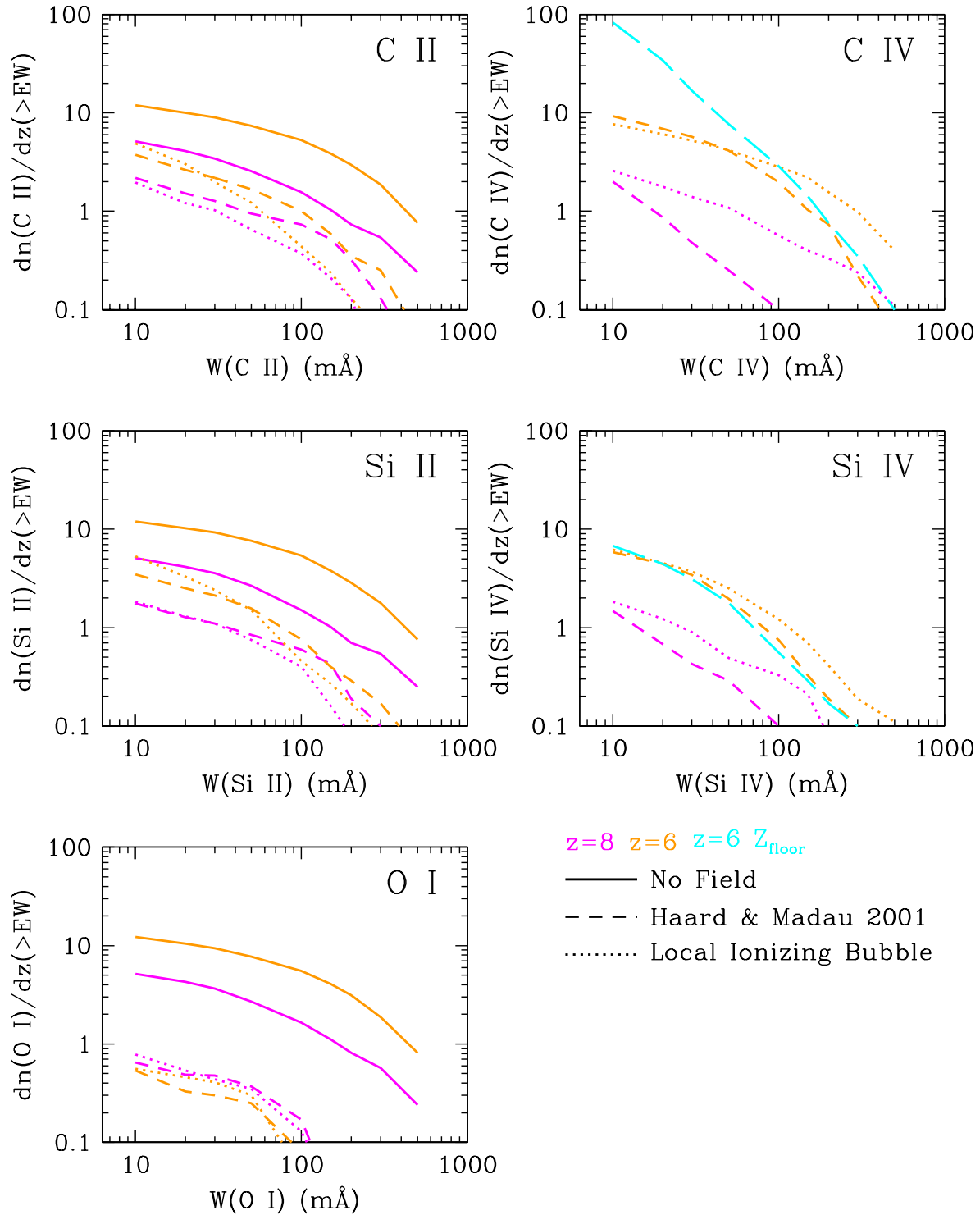


**Figure 12.** Predicted cumulative equivalent width distributions for absorber systems of five species at  $z = 8$  (magenta) and  $z = 6$  (orange). The three ionization cases are shown, along with long dashed cyan lines for C IV and Si IV corresponding to the case where a uniform metallicity floor of  $10^{-3} Z_{\odot}$  is applied to the entire volume at  $z = 6$  using the *HM2001* field. The *HM2001* field makes more strong C II and more weak C IV systems compared to the *Bubble* field at  $z = 6$ . O I is the best tracer of the *No Field* case. C IV is ideal to trace a larger volume filling factor of metals, while this is not true for its sister ion Si IV, which is mostly ionized to Si V in the same volume.

### 5.3 Equivalent Width Distributions

We present cumulative rest equivalent width (EW) distributions at  $z = 8$  and  $6$  for all five species in Figure 12<sup>5</sup>. This is intended to facilitate future observational comparisons, as well as present a more realistic assessment of the discriminatory power of high- $z$  metal absorber statistics from lower resolution near-IR spectrographs.

Many of the trends already discussed earlier in this section are reproduced here. The average weaker ionizing flux of the *HM2001* field at  $z = 6$  results in more strong C II absorbers and fewer strong C IV absorbers compared to the *Bubble* field; the opposite is true for weak absorbers. The same trends are apparent in Si II and Si IV, and also at  $z = 8$  for C IV, although the *Bubble* field produces more high ionization absorbers at all equivalent widths here. O I best distinguishes neutral and ionized gas.

We note that EWs, particularly at the high end, may be influenced by the phenomenon of turbulent broadening. In Oppenheimer & Davé (2009) we found turbulent broadening necessary to reproduce the observed low- $z$  O VI  $b$ -parameter distribution. The purported turbulence occurs far below the mass scale resolved by our simulation, and could be associated with energy injection by outflows (Oppenheimer & Davé 2009). Since high- $z$  absorbers are universally young and associated with recent outflows, turbulence may result in a higher EW (for saturated lines), which would affect the high end EW distribution. Rauch et al. (2001) observed velocity differences in  $\langle z \rangle \sim 2.7$  C IV profiles from lensed quasar LOS pairs at sub-kpc scales, which indicate more turbulence than we expect in most low- $z$  O VI absorbers. Fortunately, turbulence should not much affect the weak end, since turbulent broadening will leave EWs mostly unaltered. The other observables we have considered such as  $\Omega(\text{C IV})$  all deal with column densities, which should remain unaffected by turbulent broadening as long as lines are not saturated.  $b$ -parameters are the observable most likely affected by turbulent broadening, and may explain some of the broad C IV profiles seen by Ryan-Weber et al. (2006) and Simcoe (2006), although Becker et al. (2009) suggests that these may be multi-component systems with smaller line widths if observed at higher resolution.

We also consider the case of a metallicity floor of  $10^{-3} Z_{\odot}$  added everywhere in the simulation box with the uniform *HM2001* ionization field at  $z = 6$  for C IV (long dashed cyan line in the upper panel of Figure 12). Note that for a Chabrier IMF and Chieffi & Limongi (2004) yields, obtaining this metal floor would involve turning 0.05% of baryons into stars, equivalent to all the stars formed by  $z = 7.5$ , and distributing this uniformly among all baryons, which seems implausible. Hence this scenario requires a more exotic origin, possibly resulting from very early fast winds powered by high-yield VMSs. Such a scenario is similar to that assumed in semi-analytical enrichment models of Madau et al. (2001) & Scannapieco et al. (2002). Madau et al. (2001) calculated a complete filling factor of metals from pre-galactic outflows in their most extreme cases, while Scannapieco et al. (2002) found as much

as 40% of the  $z = 6$  volume is enriched to  $\geq 10^{-3} Z_{\odot}$  primarily by SN-driven outflows from early galaxies.

The observational signature of such a metal floor is dramatic at the weak end of the C IV equivalent width distribution. Today's instruments should be able to integrate down to  $\text{EW} = 30 \text{ m\AA}$  to statistically distinguish between our standard simulation and a metal floor:  $16.9 \Delta z^{-1}$  versus  $5.7 \Delta z^{-1}$ . We also show this scenario in the CDD plot in the bottom left of Figure 10 (long dashed cyan line). The highest  $S/N$  observations yet at  $z > 5.5$  (Becker et al. 2009) find no weak components, indicating that a significant fraction of the IGM is not enriched far above  $10^{-3} Z_{\odot}$ . Data is currently inconclusive as to the extent of volume enrichment at these low levels, but sitting on the brightest quasar at  $z > 6$  for several nights on an 8-10 meter telescope should produce the necessary  $S/N$  of  $\sim 40 - 50$  to adequately test this scenario. C IV is by far the best species for testing such a scenario, because it is the most effective tracer of metals around mean overdensity at  $z = 6$ ; Si IV is ionized to Si V at the same overdensities and the metallicity floor does affect the weak absorber frequency.

Finally, we note a contrast in the C IV distributions at high- $z$  to the  $z = 0 - 0.5$  EW distribution for O VI. The faint end turnover of the latter shows very little sensitivity to the volume filling factor of metals (Oppenheimer & Davé 2009). Part of the difference is that O VI is not tracing the lowest overdensities where metals reside at low- $z$ ; the C IV contours overlap the metals at the lowest overdensities as shown in Figure 7. This is precisely the reason why C IV holds so much potential for mapping the true extent of high- $z$  metals.

### 5.4 Aligned Absorber Ratios

Another observationally-accessible statistic is aligned absorber fractions. We consider absorbers of different ions to be aligned if both *components* are stronger than  $50 \text{ m\AA}$  and are within  $15 \text{ km s}^{-1}$  of each other ( $\delta v \leq 15 \text{ km s}^{-1}$ ). We examine the *No Field* first in Figure 13. The alignment fractions are listed in the corners, where the percentage corresponds to the likelihood of finding an absorber of the species on the opposite axis aligned with the absorber species of the near axis. For the neutral case, the alignment percentages are above 95% in every case. This lends support to the idea that the low ionization species observed by BSRS, which appear aligned in every case for O I observed above  $z = 5.8$ , are tracing metals where there is no ionizing flux above the Lyman limit. These systems occur far too frequently to be arising within the ISM of intervening galaxies according to BSRS. This could be evidence that patchy reionization is still occurring at these redshifts, or alternatively that dense cloudlets entrained in winds are self-shielded from the ionizing background. The latter scenario would predict that there be high ionization species in the same systems, possibly offset, indicating multi-phase outflows as observed locally (e.g. Strickland et al. 2002; Martin 2005b) and seen in galactic-scale simulations (e.g. Fujita et al. 2008). Therefore C IV and Si IV could be very useful additional constraints.

The high alignment fractions are helped by the fact that these three species have similar EWs for typical Type II SNe yields. Aligned absorbers fall along the linear relations in each subplot of Figure 13, where the ratios in column densities equal the ratios in Type II SNe Chieffi & Limongi

<sup>5</sup> Please contact the author for the tabular form of the predictions in these or any other figures. We have EW and CDD distributions for any other desired redshift as well.

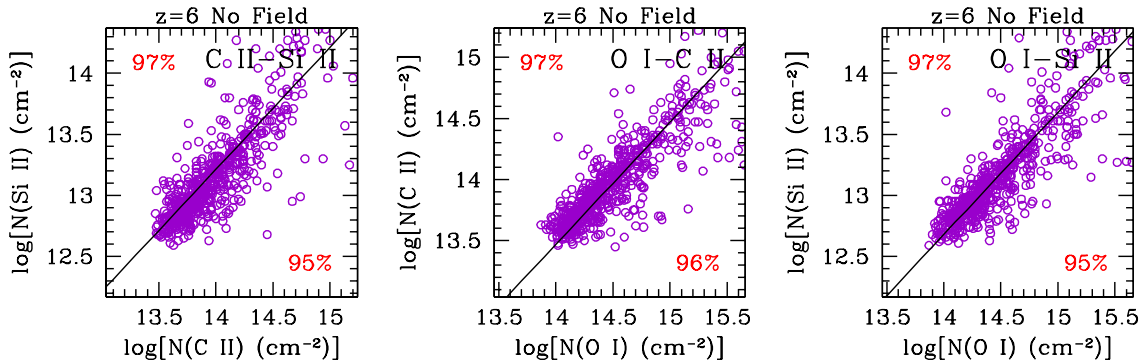


**Figure 13.** Aligned absorbers of different ions are defined as having both components above  $50 \text{ mÅ}$  and a velocity difference less than  $15 \text{ km s}^{-1}$ . Here we present the *No Field* case, which at  $z = 6$  shows absorbers fall along a linear relation with some scatter; the lines show the expected relation if Type II SNe yields (Chieffi & Limongi 2004,  $Z = 10^{-3}$ ) with no ionization corrections assumed. Alignment fractions are listed in the corners, where the percentage corresponds to the likelihood of finding an absorber of the species on the opposite axis aligned with the absorber species of the near axis. The percentages exceed 95% in every case, and remain similarly high when the velocity tolerance is reduced to  $8 \text{ km s}^{-1}$ , because they are tracing metals in the same neutral gas.

(2004) yields. Although we use a component separation criterion of  $\delta v \leq 15 \text{ km s}^{-1}$ , the alignment statistics are nearly identical when  $\delta v = 8 \text{ km s}^{-1}$  and  $\delta v = 32 \text{ km s}^{-1}$ . This is generally the case in all alignment statistics considered here, which indicates that the species are tracing the same underlying gas. This contrasts with, for instance, low- $z$  O VI – H I alignment fractions which are markedly larger at higher  $\delta v$  (Tripp et al. 2008; Thom & Chen 2008a), because O VI traces physically distinct gas from the Ly $\alpha$ -forest (Oppenheimer & Davé 2009).

The alignment between low and high ionization species in Figure 14 indicate many fewer aligned absorbers. C II is aligned with C IV 45-62% of the time, while C IV is found aligned 11-23% of the time with C II. Finding C II where C IV exists should occur much less frequently than the other way around according to the visualizations in Figures 5 and 9; the small filling factor of C II is more often coincident with C IV, while C IV can also trace the more extended metals. This is an ideal ratio to measure the shape of the ionization background, since abundance ratios are irrelevant and the carbon spectral ratio that is measured covers a large ionization range from 11.3 to 47.9 eV. There exist stronger C IV components aligned with C II for the *Bubble* field relative to the *HM2001*, due to the greater hardness of the former field. In the one component Ryan-Weber et al. (2006) could measure both at  $z = 5.7239$  in SDSS J1030+0524, they found no aligned C II. A sample size of at least a dozen strong C IV components exploring aligned C II should begin to build enough statistics to constrain the shape and intensity of the ionizing background.

Si II and Si IV alignment provides a similar opportunity as the carbon species to measure the shape of the background, and the alignment fraction is even higher than for carbon due to the lower ionization potential of Si III (33.5 eV) compared to C III. BRSR actually does find aligned Si IV in three of their components lying close together in the  $z = 5.3364$  system of SDSS J0231-0728. This system indicates possible non-uniform ionization, because the very aligned profiles of C II, O I, and Si II in components about  $100 \text{ km s}^{-1}$  away from the aligned Si II – Si IV is a strong indicator of the *No Field* case, while Si IV requires an ionizing field. BRSR mentions that aligned C IV is also present ac-

ording to Barth et al. (2003), but the low resolution of that observation makes it difficult to determine the component alignment; we expect it to be aligned to the components exhibiting the Si IV. The presence of low and high ions nearby suggests a galactic ISM as might be seen in a damped Ly $\alpha$  system, as forwarded by BRSR.

C II is usually found with O I, but the reverse is not true if there is an ionization field above the Lyman limit. The bluest component of the  $z = 5.3364$  BRSR system mentioned above is consistent with a non-detection of O I with the observed C II and Si II, supporting some sort of ionization field. Finding the fraction of C II absorbers with aligned O I is one of the most sensitive indicators of the three different ionizing cases we explore.

Finally, we do not show the incidence of O I aligned with C IV, because this case rarely occurs under an ionizing field due to the large difference in ionization potentials. This is apparent in SDSS J1148+5251 as Becker et al. (2009) finds no C IV despite the 4 O I absorbers (BRSR).

Overall, the alignment fractions offer another way to constrain the nature of the ionization field. Current data are in line with expectations from our models, though this is not highly constraining. Larger samples will elucidate the nature of individual absorbers, and possibly allow one to measure the carbon spectral ratio which could give clues as to the nature of ionizing sources.

## 5.5 System Profiles

Finally in this section, we consider the appearance of systems in absorption line spectra. As an illustration, we choose a series of LOSs through the region indicated in Figure 15, which is the same region shown evolving in Figure 9 centered on the second most massive galaxy in the simulation box. We choose two LOSs that go exactly through the center of this  $M_* = 10^{9.1} M_\odot$  galaxy and show the system profiles for our five ions and our three fields in Figure 16. The  $x$ -direction spectrum is more along the direction of the local filament, while the  $y$ -direction is nearly along the axis of the bipolar outflow. Both show extremely strong systems, but the  $y$  spectrum is remarkably wide ( $800 \text{ km s}^{-1}$ ) owing to pecu-

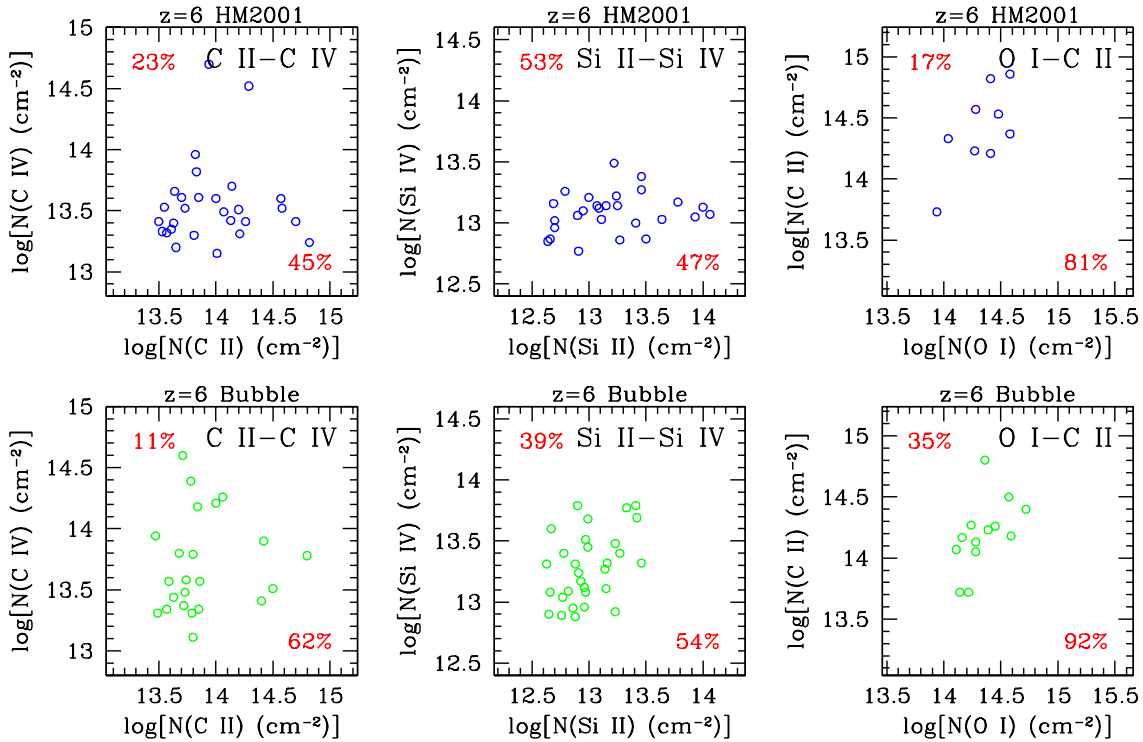


**Figure 14.** Aligned absorber ratios and percentages displayed analogously to Figure 13 for the *HM2001* and *Bubble* ionization fields. Symbols indicate components where both absorber species are  $> 50 \text{ mÅ}$  and  $\delta v < 15 \text{ km s}^{-1}$ , while percentages correspond to the likelihood of finding an absorber over  $50 \text{ mÅ}$  of the species on the opposite axis aligned with the  $> 50 \text{ mÅ}$  absorber species of the near axis. Aligned ratios can help distinguish the shape and magnitude of the ionization field, especially in the case of C II – C IV. The alignment fraction of C II with O I is one of the best ways to distinguish the three ionization cases, although these are rare if the IGM is ionized.

liar velocities imprinted by the enriching outflows. Comparing the physical parameters of the gas in the bottom three panels without peculiar velocities (cyan) and with peculiar velocities (red) shows that the velocity structure dominates the system profiles of both LOSs. This galaxy has a maximum  $v_{\text{wind}}$  just over  $500 \text{ km s}^{-1}$ , therefore  $\delta v \sim 400 \text{ km s}^{-1}$  on each side of the  $y$  spectrum is sensible as winds are launched with an intentional spread of velocities, plus the LOS is slightly offset from the outflowing axis.

None of the observed systems in the data (or in our 70 LOSs) have profiles as strong and as wide as the systems in Figure 16, because not surprisingly lines of sight directly through the centers of galaxies are rare. If we assume similar profiles arise within 3 kpc of the 10 galaxies in our simulation box over  $M_* = 5 \times 10^8 M_\odot$ , then the frequency of intersecting such a system occurs once in  $\Delta z = 2000!$  A more relevant consideration for the spectra in Figure 16 is to take the blue-shifted half and model the outflows in the spectra of LBGs at lower redshift ( $z \sim 2 - 3$ ), where such galactic superwinds have been observed to be common and observations are more obtainable (Pettini et al. 2001; Shapley et al. 2003); this is beyond the scope of this paper. We note that the faster moving materials absorb more in the lower ionization species with the weaker *HM2001* background.

More typical examples of quasar absorption line systems are shown in Figure 17 where two LOSs have impact parameters,  $b$ , of 30 kpc to the same galaxy. Velocity profiles of absorbing ions are still dominated by peculiar velocities, and the LOS closest to the outflow axis ( $y$  direction) produces

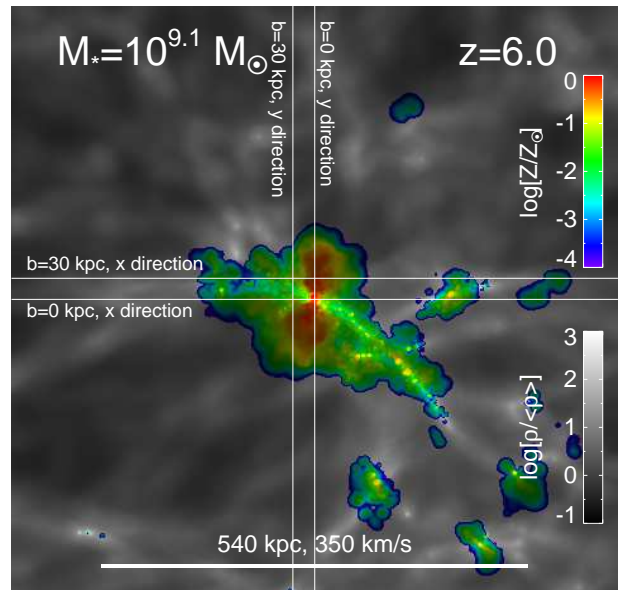


**Figure 15.** The  $4 \times 4 h^{-1} \text{ Mpc} \times 25 \text{ km s}^{-1}$  region shown in Figure 9 at  $z = 6$  with intersecting LOSs, of which we show the absorption line profiles in Figures 16 and 17. This snapshot spans 950 physical kpc, and the Hubble parameter is  $651 \text{ km s}^{-1} \text{ Mpc}^{-1}$ .

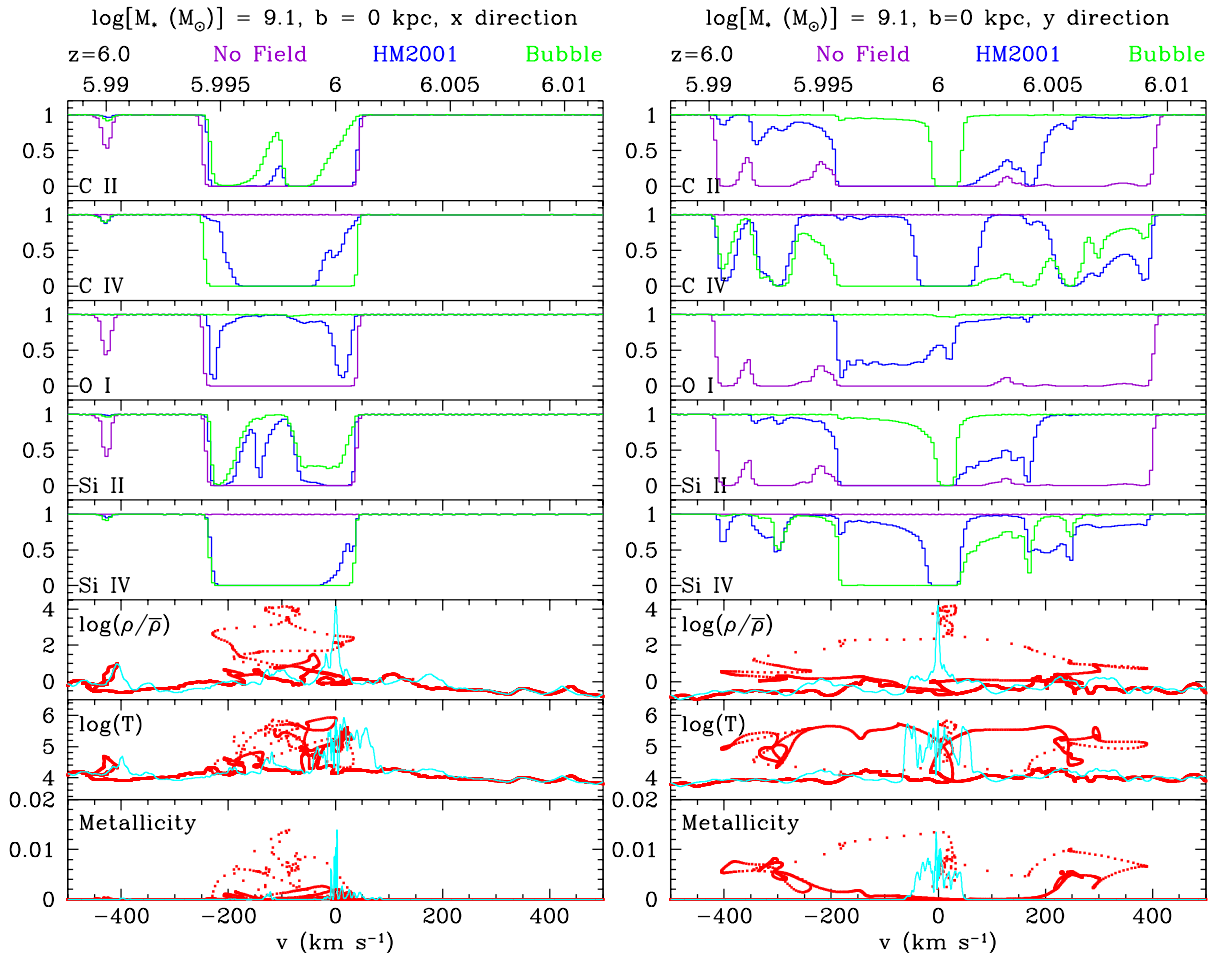


**Figure 16.** The LOSs in Figure 15 intersecting the center of the  $M_* = 10^{9.1} M_\odot$  galaxy. The  $y$  LOS (right) shows more extended absorption line profiles ( $\delta v \sim 800 \text{ km s}^{-1}$ ), because it is along the bipolar outflow axis, while the  $x$  LOS (left) follows more closely the local filament. No systems in the data or in our 70 simulated LOSs match such profiles, because intersecting such regions is extremely rare when considering quasar LOSs, which probe a volume-weighted sample. The blue-shifted side of these profiles may be more appropriate when considering the absorption of the outflows and galactic ISM in the spectra of LBGs and high- $z$  galaxies. Lower ionization species show broader profiles in the *HM2001* case versus the *Bubble* case.

a wider system. This system is perhaps most qualitatively similar to the two wide systems observed in low ionization species by BRS where C II, Si II, and in one case O I show a total velocity spread of  $\delta v \sim 250 \text{ km s}^{-1}$ . This supports the idea of neutral/low-ionization gas entrained in outflows, self-shielded from the ionization background; this probably makes more sense for the  $z = 5.3364$  system than patchy reionization extending to this redshift. A similar velocity spread is observed by Simcoe (2006) in his C IV  $z = 5.829$  system.

Although an alignment within 30 kpc occurs once in  $\Delta z = 20$  (if we count the ten most massive galaxies in the d16n256vzw box), we will argue in §6.3 that such systems are qualitatively similar to systems observed around lower mass galaxies at lower impact parameters. The frequency of intersecting such qualitatively similar systems as those shown in Figure 17 is  $\Delta z \sim 2.8$  if we consider all galaxies  $M_* > 10^7 M_\odot$ , and  $d_{gal} < 30 \sqrt{\frac{M_*}{10^9}}$ . Two such systems should have been intersected by now given the combined pathlength of Becker et al. (2009) & Ryan-Weber et al. (2009), which compares well to three strong C IV systems being observed.

Three differences when scaling to lower stellar mass are (i)  $\delta v$  of systems are smaller as the outflow velocities are smaller, (ii) metallicities will be lower due to the mass-metallicity relation, and (iii) the mass loading factors should be higher at lower mass, which counterbalances (ii).

In Figure 18 we show how median  $\delta v$  varies as a function of column density in our 70 LOS  $z = 6$  sample. Here  $\delta v$  is defined as the difference between the central velocities of the two furthest components in a system ( $\delta v = 0$  when there is a one component system). One  $\sigma$  boundaries (dashed lines) show the range of velocity spreads in each case. This can be compared to a sample of the same spectra without peculiar velocities, shown as long dashed orange lines. While this is not strictly a fair comparison as systems without peculiar velocities will not necessarily fall into the same column density bin, this nevertheless clearly illustrates that the stronger observed systems are dominated by peculiar velocities. At high column densities, greater than 50% of a system's width owes to the peculiar velocities from outflows. With future samples, such a plot can be used to infer conclusions about the imprints of outflows on high- $z$  metal-line profiles. We do

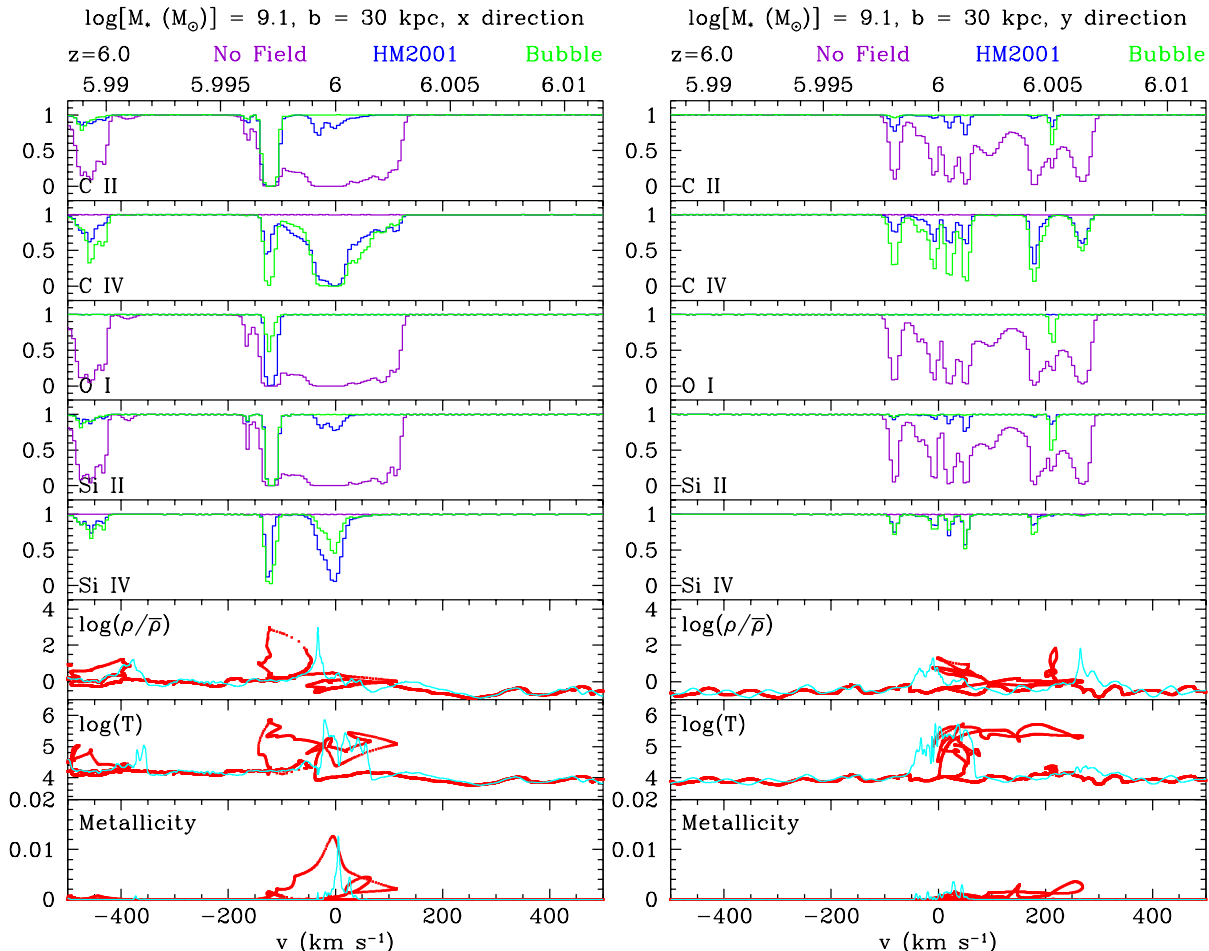


**Figure 17.** The two LOSs illustrated in Figure 15 with impact parameters of 30 kpc. As in Figure 16 peculiar velocities dominate the system width, and the  $y$  LOS (right) exhibits a more extended profile as this is close to the axis of the bipolar outflow. These systems are more similar to those observed in quasar LOSs, and could be analogous to some of the broader systems observed by BSRs and Simcoe (2006).

not make a direct comparison now, because of the paucity of observed systems and differences in both  $S/N$  and resolution, which may affect such a comparison.

The main points here are that (i) we produce systems qualitatively similar to those observed in the data at a frequency that seems reasonable; and (ii) the velocity widths of the strongest observed systems are likely to be dominated by peculiar velocities associated with outflowing gas. The latter suggests that plots of  $\delta v$  vs. column density may provide constraints on outflow kinematics from high- $z$  galaxies.

## 6 THE PHYSICAL ENVIRONMENT OF ABSORBERS

As our simulations form galaxies and enrich the IGM together, we are able to explore the relationship between galaxies and metal absorbers, along with their physical and environmental properties. `specexbin` tracks for each absorber the physical properties of density, temperature, and metallicity; the environmental properties of the distance and stellar mass of the nearest galaxy; plus the last time an SPH particle was launched in a wind (i.e. its “age”). We also track an SPH particle’s SFR if it is in a galaxy, or  $v_{\text{wind}}$  at which it was

launched if in an outflow. Unless otherwise mentioned, we use the *Bubble* model, because (i) the ionizing flux from the local galaxy should dominate at the distance of the metals given the reasonable assumptions for the transmission above the Lyman limit, and (ii) this field produces a shallower column density distribution, which seems to be supported by the data. Note, however, that the *No Field* approximation may best explain some absorbers, most notably those in the J1148+5251 LOS. This may help remedy the overestimated *Bubble*  $\Omega(\text{C IV})$  if more metals are at lower ionization states as we suggest in §6.3.2. We also address the physical environment of the *HM2001* field, which may be most appropriate at  $z < 6$ , in §6.3.1

We concentrate on C IV absorbers at  $z = 6$ , examining first their physical state and then their evolutionary status, and bring them together by exploring the high- $z$  galaxy-absorber connection. We consider an absorber’s connection to the stellar mass of its originating galaxy, which in our models is a good proxy for the more observationally-accessible SFR. This leads us to a suggestion of possibilities of why we may produce too many weak absorbers at high- $z$ . We then switch to lower ionization species represented by C II, and lastly extend our analysis back to  $z = 8$ .

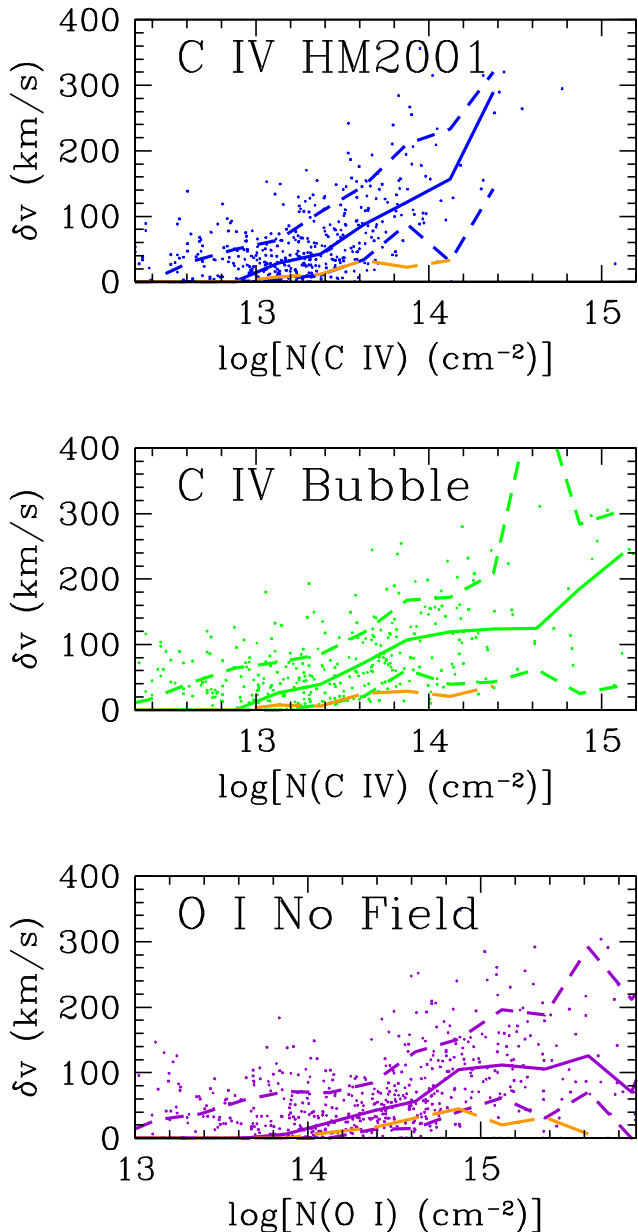


**Figure 18.** System width ( $\delta v$ ) versus column density for C IV *HM2001* and *Bubble* fields (top and middle), and the O I *No Field* case (bottom). Solid lines indicate the median and dashed lines show  $1\sigma$  dispersions.  $\delta v$  is defined as the velocity difference between the central velocities of the two furthest components in a system. The orange long-dashed lines show  $\delta v$  if we make our LOSs without peculiar velocities (i.e. the spatial distribution contributes to the system width). The majority of the system width is due to peculiar velocities, where outflowing metals broaden the profile.

### 6.1 Physical Conditions

Figure 19 shows four absorber properties plotted against each other for  $z = 6$  C IV absorbers in the *Bubble* field. In the upper left panel are the same type of logarithmic metallicity contours considered in Figure 7. C IV has the smallest global ionization correction at  $z \sim 5 - 6$ , because the ionization fractions of this species are ideally aligned with the range of densities at which metals reside at this redshift ( $\delta \sim 0 -$

100). Histograms in the bottom left panel show that stronger absorbers trace higher overdensities.

Temperatures indicate predominantly photo-ionized C IV. Outflows typically heat gas to  $10^{5-6}$  K around galaxies, but the gas quickly cools to warm IGM temperatures due to efficient cooling in this range. This appears to contradict our previous work in OD06, where we claimed a significant fraction of  $z \sim 6$  C IV (43%) is collisionally ionized, but the difference arises because in OD06 we quoted a mass-weighted fraction (from particles), while here we are computing a volume-weighted quantity (from spectra). For  $\delta < 200$ , our present models agree well with OD06, comparing Figure 9 in OD06 with the upper left of Figure 19. Regions with  $\delta > 200$  are mostly forming stars at  $z = 6$ , and the frequency of metal systems where  $N(\text{C IV}) \geq 10^{13} \text{ cm}^{-2}$  includes SPH particles above the SF threshold is  $0.4\Delta z^{-1}$ . Of the 54 components with  $N(\text{C IV}) > 10^{14} \text{ cm}^{-2}$ , only 12 have any traces of SF. Ironically, only one of these 12 lines has its line center density at  $\delta > 200$ ; even when LOSs probe galactic environments, the C IV absorbing gas is primarily intergalactic<sup>6</sup>. Hence our models clearly predict that the vast majority of typical C IV absorbers are primarily intergalactic at  $z = 6$ , and the rest mostly trace halo outskirts.

The average carbon metallicities at  $N(\text{C IV}) = 10^{13.0}$  and  $10^{14.0} \text{ cm}^{-2}$  are 0.05 and 0.10  $Z_{\odot}$  respectively. This is about  $\sim \times 15 - 20$  the IGM metallicities at the corresponding overdensities, using the simulation-averaged metallicity-density relation in Figure 4. Hence C IV absorbers are tracing a clumpy, inhomogeneous distribution of metals with a very low volume filling factor,  $\lesssim 0.1\%$ . This is generic in our models, and is even seen at the present day for O VI absorbers (Oppenheimer & Davé 2009). The metallicity inhomogeneity is even more extreme at  $z = 8$ : 0.06  $Z_{\odot}$  for  $N(\text{C IV}) = 10^{13.5-14.0} \text{ cm}^{-2}$ , while the simulation-averaged metallicity is  $9 \times 10^{-4} Z_{\odot}$  (a factor of  $\sim 70$ ). This shows that metal-line absorbers trace an increasingly clumpy distribution of metals at early times going back from  $z = 6 \rightarrow 8$ , a trend that extends to low- $z$  IGM metals as traced by O VI (Oppenheimer & Davé 2009).

In summary, C IV absorbers seen at  $z \sim 6$  are mostly expected to be true intergalactic absorbers, not gas within galaxies or galactic halos. Galaxy outflows reach a larger comoving volume at early times (OD08), but in actuality they are enriching a small fraction of the volume in a highly patchy fashion.

### 6.2 Origin of IGM Metals

We now consider how an absorber's age relates to its environment, as a way of characterizing in which regions IGM metals originate. An age-density anti-correlation exists in  $z = 6$  C IV, with a significant spread, as shown in the bottom left panel of Figure 19. This is the same trend we see in

<sup>6</sup> The one absorber tracing primarily galactic gas has  $\delta \sim 1000$  and  $N(\text{C IV}) = 10^{17.5} \text{ cm}^{-2}$ ! This may be an unphysical amount of C IV, but this one absorber comprises 88% of the total  $\Omega(\text{C IV})$  along all LOSs. This example illustrates the reason for the discrepancy between the volume-derived  $\Omega(\text{C IV})$  of  $N(\text{C IV}) = 10^{13.0-15.0} \text{ cm}^{-2}$  absorbers versus the mass-derived  $\Omega(\text{C IV})$ , as discussed in §5.2.

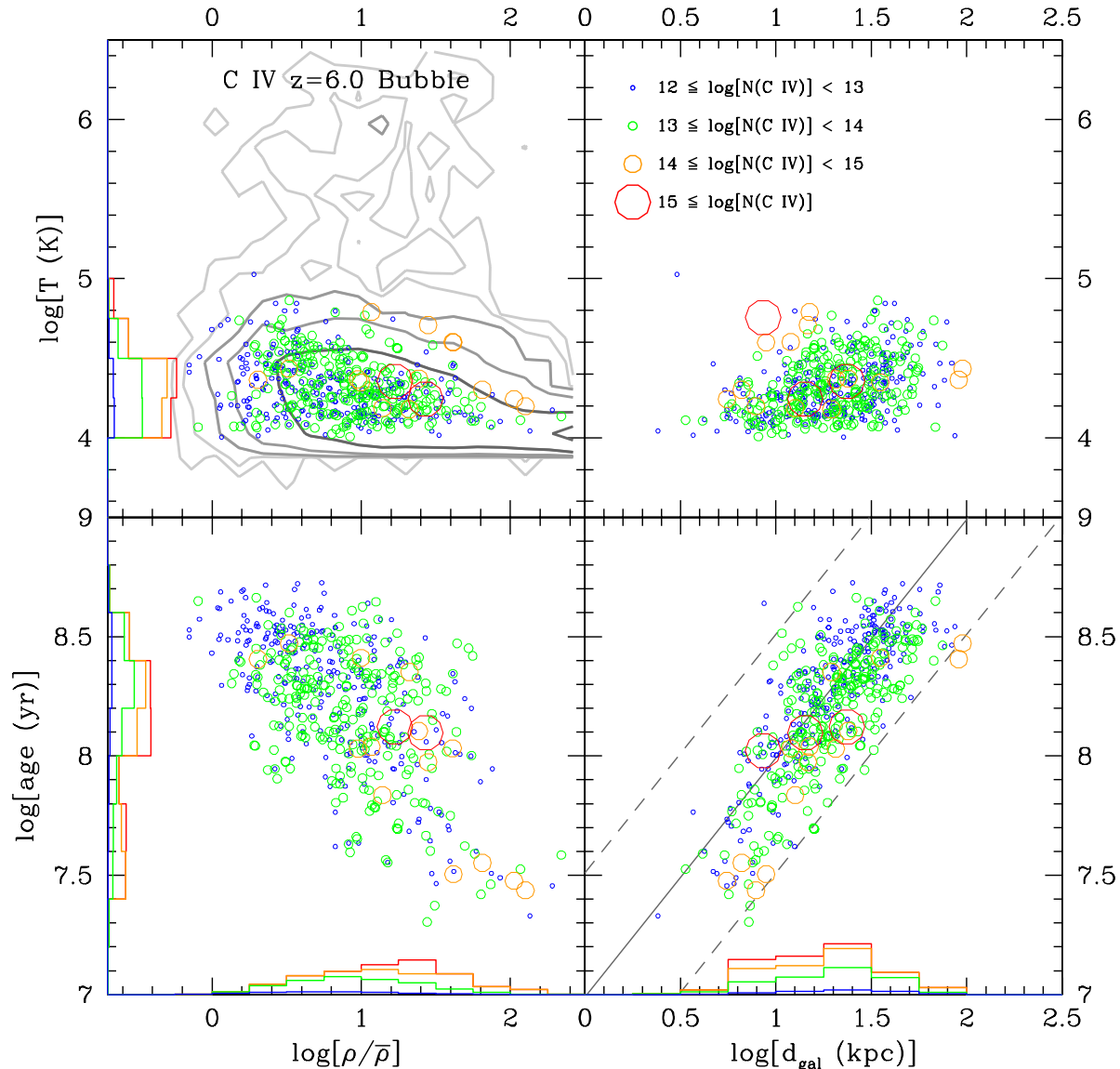


**Figure 19.** *Physical conditions of C IV:* C IV absorbers at  $z = 6$  with the variable *Bubble* field are plotted in planes of density, temperature, absorber age, and distance to the nearest galaxy. Logarithmic contours at 0.5 dex steps in the  $\rho - T$  phase space correspond to the metallicity-weighted density (darker contours are greater densities). In the  $d_{gal}$ -age plane, an effective outflow velocity can be calculated by dividing the two quantities; we show a solid gray line corresponding to  $v_{\text{eff}} = 100 \text{ km s}^{-1}$ , with the 30 and 300  $\text{km s}^{-1}$  indicated by the dashed gray lines to the left and right. Histograms along the side show the summed  $\Sigma N(\text{C IV})$ , with each color corresponding to the column density range indicated by the key in the upper right panel; all absorbers where  $N(\text{C IV}) > 10^{15} \text{ cm}^{-2}$  are counted as contributing only  $10^{15} \text{ cm}^{-2}$  to this sum due to these lines being saturated. Histograms show stats in 70 simulated LOSs, but points are plotted for absorbers in 30 LOSs.  $z = 6$  C IV is predominantly photo-ionized, tracing a range between  $\delta = 0 - 100$ . Stronger absorbers arise from higher overdensities and are generally younger. Most absorbers are 30–300 Myr old, lying 5–50 kpc from their parent galaxy. The average  $v_{\text{eff}} \sim 100 \text{ km s}^{-1}$  far from galaxies, which is half as much as the typical ejection speed  $v_{\text{wind}}$ .

low- $z$  O VI (Oppenheimer & Davé 2009) where stronger absorbers trace higher densities that have been enriched more recently. In the case of C IV, absorbers over  $10^{14} \text{ cm}^{-2}$  are more likely to trace metals ejected on average 100 Myr ago, while weaker absorbers trace metals 100–300 Myr ago from earlier galaxies when they were at lower mass and metallicity.

The age-density relation can be understood by considering the age-galaxy distance ( $d_{gal}$ , shown in physical kpc) relation in the bottom right panel of Figure 19. Older absorbers have had time to travel greater distances reaching

lower overdensities. Taking  $d_{gal}$  divided by age, we can plot the average velocity these winds need to travel to get as far as they do, which we call the effective wind speed,  $v_{\text{eff}}$ . The gray solid line shows  $v_{\text{eff}} = 100 \text{ km s}^{-1}$  and the dashed lines on the left and right sides are 30 and 300  $\text{km s}^{-1}$  respectively. Comparing this to the average wind speed at launch  $v_{\text{wind}} = 200 - 250 \text{ km s}^{-1}$  (cf. Figure 3), we see that outflowing gas typically slows 20–50% by the time it reaches the IGM. As argued in OD08, this slowing is primarily hydrodynamical as outflows run into a dense IGM, though gravity plays a non-trivial role.

The good age- $d_{\text{gal}}$  correlation indicates that these absorbers trace metals leaving galaxies for the first time. This also is expected from the evolutionary picture of feedback from  $z = 6 \rightarrow 0$  presented in OD08, where we found that metals more often than not recycle (i.e. return to a galaxy at later time and are shot out in another wind/form into stars). Metals recycle on a timescale of 1-3 Gyr reaching a median farthest distance of  $\sim 60 - 100$  proper kpc from their parent galaxies. C IV is tracing metals on their first journey into the IGM, because the ages and distances in Figure 19 are nearly all less than the recycling times and turn-around distances. These absorbers primarily reside in the IGM and not in halos, because the halo radius (from Navarro, Frenk, & White 1997) is  $\lesssim 5$  physical kpc for all  $z = 6$  galaxies in our simulation; nearly all absorbers are at distances above this value in Figure 19. Hence C IV absorbers are tracing IGM metals on their first journey outward from galaxies at  $z = 6$ .

As another way of considering absorber origin, we plot the ratio of the effective velocity to the launch velocity ( $v_{\text{eff}}/v_{\text{wind}}$ ) versus the distance from a galaxy (left panel) and the launch velocity (right panel) in Figure 20. This ratio should not exceed one, given that wind particles are slowed as they travel outward. A few absorbers at greater than one are mostly due to the rare instances when the neighboring galaxy is not the originating galaxy for a wind. The clearest trend is that  $v_{\text{eff}}/v_{\text{wind}}$  shows a general decline with  $d_{\text{gal}}$ . For absorbers with  $N(\text{C IV}) = 10^{13.5-14.5} \text{ cm}^{-2}$ , the strength of most components observed by Ryan-Weber et al. (2006) and Simcoe (2006), the median ratio is nearly unity at 3-5 kpc, 0.8 at 10 kpc, and 0.5 by 50 kpc. Note that our outflow prescription (following Springel & Hernquist 2003a) turns off hydrodynamic forces for a time that does not exceed that required to cover 4 physical kpc (at  $z = 6$ ) at  $v_{\text{wind}}$ . This shows that, as soon as hydro forces are turned on, outflows begin slowing down as they travel further from their parent galaxy.

Several other physically interesting trends are also evident in the right panel of Figure 20. First, stronger absorbers arise from more massive galaxies with greater  $v_{\text{wind}}$ ; more massive galaxies enrich the IGM with higher metallicity outflows due to the mass-metallicity relationship at high redshift ( $Z \propto M_{\text{gal}}^{0.3}$ ; DFO06). Second, winds from massive galaxies slow down quicker as indicated by lower  $v_{\text{eff}}/v_{\text{wind}}$  at higher  $v_{\text{wind}}$ ; this arises because massive galaxies tend to be surrounded by denser gas (OD08).

### 6.3 The Galaxy-Absorber Connection

While we have explored numerous relations between absorber physical and environmental parameters at  $z = 6$ , there is as of yet no over-riding correlation to explain C IV absorber strengths, as each parameter exhibits considerable scatter versus  $N(\text{C IV})$ . Here we argue that the *fundamental relation* governing metal absorbers is the stellar mass,  $M_*$ , of the neighboring galaxy versus the distance to that galaxy,  $d_{\text{gal}}$ , and most other correlations are merely a consequence. The neighboring galaxy is defined as the galaxy with the greatest impinging flux on an absorber (i.e. the nearest galaxy weighted by the inverse square law). Figure 21 shows the  $M_* - d_{\text{gal}}$  relation. As is evident, the relation between  $d_{\text{gal}}$  and  $N(\text{C IV})$  at a given  $M_*$  shows a strong correlation. We plot gray dotted lines corresponding to the rela-

tion  $d_{\text{gal}} \propto \sqrt{M_*}$  representing the constant flux levels resulting from the *Bubble* field due to the inverse square law. If all physical conditions are equal, absorbers along these lines should be identical. Indeed, this seems to hold reasonably well. Hence the key deterministic relation for absorber strength is distance from galaxy of a given stellar mass, more so than any of the physical parameters explored in the previous sections. The paucity of absorbers below the bottom-most gray dotted line is only a selection effect poorly sampling these regions in a volume-averaged measurement; very strong absorbers exist here if LOSs are fortunate enough to sample them (e.g. the extreme systems displayed in Figure 16).

Absorbers are closely related to galaxies at high- $z$  more so than any other time because (i) metals are on their first journey into the IGM, (ii) they are still in close proximity to their parent galaxies, and (iii) galaxy evolution is relatively simple to understand at high- $z$  as galaxies are mostly evolving in isolation. We use these assumptions to construct the solid gray “evolutionary tracks” that metals take into the IGM, assuming constant  $v_{\text{eff}} = 100 \text{ km s}^{-1}$  and an exponentially increasing  $M_*$  with time, which approximately falls out of the integration of Equation 4. Although both of these assumptions are not exactly true, this treatment reveals some important behaviors.

First, “isochrones” travel parallel to the x-axis of Figure 21 by construction if  $v_{\text{eff}}$  is assumed to be independent of  $M_*$ , meaning the absorbers of the same age are found at a similar distance. This of course an oversimplification, because  $v_{\text{eff}}$  slows down as time passes and winds with higher  $v_{\text{wind}}$  slows down faster. However, this explains why there are very few weak absorbers ( $N(\text{C IV}) < 10^{13} \text{ cm}^{-2}$ ) around  $M_* > 10^8 M_{\odot}$  galaxies; metals simply have not had time to travel far enough to the low-density regions where weak C IV absorbers would arise.

Second, tracing the evolutionary tracks back to the bottom reveals the mass of the launch galaxy for each metal absorber. DFO06 plotted the mass-metallicity relationship of  $z = 6$  and  $z = 8$  galaxies, finding that gas metallicity increases by  $\sim 0.3$  dex per decade of  $M_*$ . Although the overriding trend for absorber strength depends on the ionizing flux in the *Bubble* field, a more subtle trend (hardly visible) is that absorbers grow stronger rightward along the same dotted gray line primarily as a result of the mass-metallicity relationship. However, this effect is about half as strong as expected ( $\sim 0.15$  dex), and should be counter-balanced by increased mass loading factors of smaller galaxies. Also, consider that  $v_{\text{eff}}$  is not really constant, which limits us from over-interpreting this plot.

The only candidate observed high- $z$  galaxy-C IV absorber connection is along the J1030+0524 LOS, where Becker et al. (2009) notes the observed systems at  $z = 5.7 - 5.9$  may be related to an excess of *i*-band dropouts observed by Kim et al. (2008) along this quasar LOS. In our models, most absorbers between  $N(\text{C IV}) = 10^{13.0-15.0} \text{ cm}^{-2}$  are associated with galaxies where  $M_* = 10^{7.0-8.5} M_{\odot}$ , which have corresponding 1350 Å AB magnitudes ranging between  $-15.4$  and  $-18.9$  (see the luminosity range bounded by green dotted lines in Figure 2), and SFRs from  $0.05 - 1 M_{\odot} \text{ yr}^{-1}$ . The closest of the J1030 absorbers lies about 50 arcseconds away from a galaxy, i.e. an impact parameter of 300 kpc, which is too far for our winds to reach

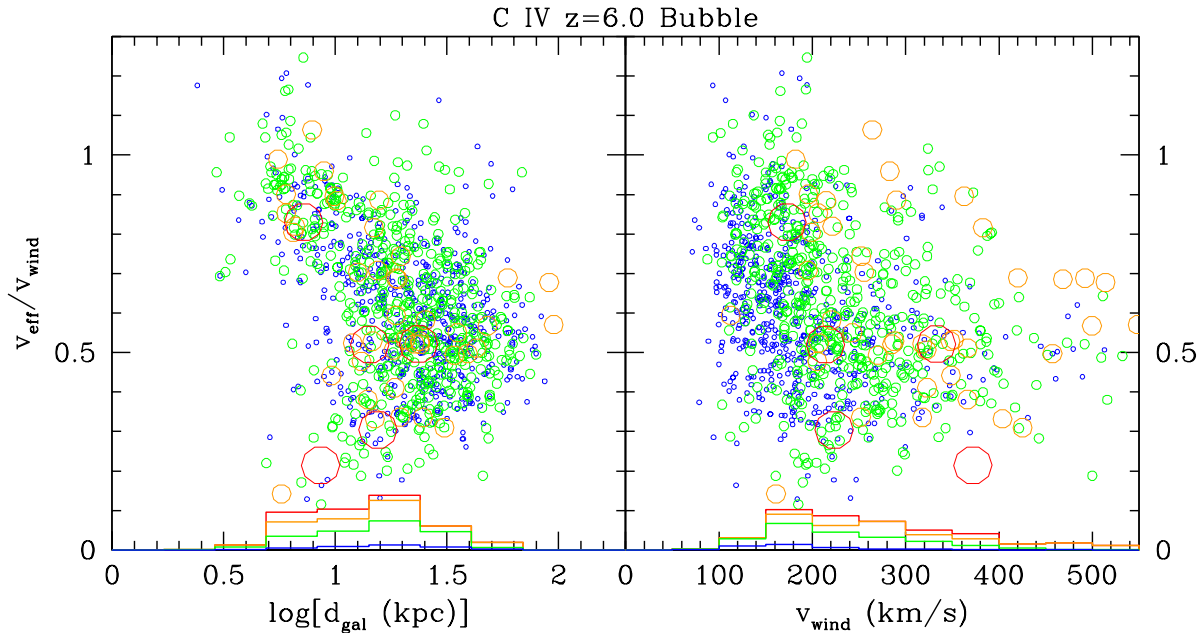


**Figure 20.** The ratio of a wind particle’s effective velocity ( $d_{gal}$  divided by age) and launch velocity  $v_{wind}$  is plotted against  $d_{gal}$  (left) and  $v_{wind}$  (right). This ratio generally declines the farther it travels from a galaxy as hydrodynamic and gravitational forces slow outflowing metals. Stronger absorbers arise from faster winds launched from more massive galaxies, but these winds are more likely to slow down faster as indicated by a declining  $v_{eff}/v_{wind}$  at higher  $v_{wind}$ . The color key for absorber strength in Figure 19 applies here.

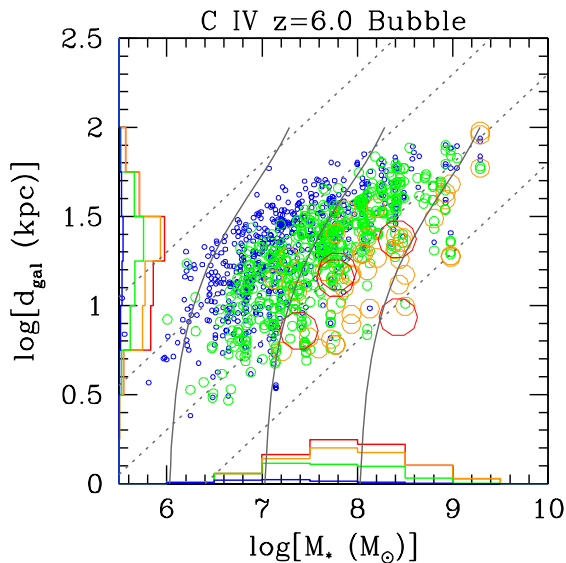


**Figure 21.** *Galaxy-absorber connection plot:*  $d_{gal}$  vs.  $M_*$  elucidates the fundamental and close connection between galaxies and absorbers at high- $z$ . It reveals a strong correlation between  $N(\text{C IV})$  and  $d_{gal}$  for a given mass galaxy. The ionizing conditions are identical in the *Bubble* field along the gray dotted lines, explaining much of this correlation. Evolutionary tracks (solid gray lines for winds emanating from a  $M_* = 10^6, 10^7, \& 10^8 M_\odot$  galaxy) tracing an absorber back to its parent galaxy assuming a constant  $v_{eff} = 100 \text{ km s}^{-1}$  and secular galaxy growth. Currently observable  $z = 6$  C IV absorbers are launched from galaxies between  $M_* = 10^{6.5-8.0} M_\odot$ , but are observed around galaxies with  $M_* = 10^{7.0-8.5} M_\odot$ . The color key for absorber strength in Figure 19 applies here.

(e.g.  $v_{eff} \gtrsim 1000 \text{ km s}^{-1}$  for 300 Myr); plus the magnitudes of these galaxies appear to be brighter than any of the galaxies in the d16n256vzw simulation box. This may be an extended overdense region of space where smaller, currently unobservable galaxies are primarily responsible for the enrichment.

### 6.3.1 *HM2001 Background Case*

The uniform *HM2001* background case may be more appropriate below  $z = 6$ , and actually better explains the observed frequency of strong C IV absorbers at  $\langle z \rangle = 5.75$ , although it is more discrepant in over-estimating weaker absorbers. We show the galaxy-absorber connection plot in Figure 22 for this field and note the following differences. First, the distance and mass of the neighboring galaxy matters less for the characteristics of these absorbers; the dotted lines do not have any meaning, but are shown for relative contrasts with Figure 21. As this field is weaker near galaxies, there are fewer strong absorbers because carbon is in lower ionization states. For the same reason, there are more weak C IV absorbers at greater distances from galaxies, because these metals are otherwise ionized to C V by the *Bubble* field.

A potentially accessible distinguishing characteristic of the two fields involves components with  $N(\text{C IV}) > 10^{14.0} \text{ cm}^{-2}$ , which are only found around  $M_* \sim 10^9 M_\odot$  galaxies in the uniform case. These absorbers arise in the situations like those illustrated in Figure 15, where a bipolar outflow copiously enriches the low density IGM outside of filaments where the *HM2001* C IV ionization correction is lowest. The strongest absorbers actually arise from overdensities less than 10, which is the opposite of the behavior in the *Bubble* model.

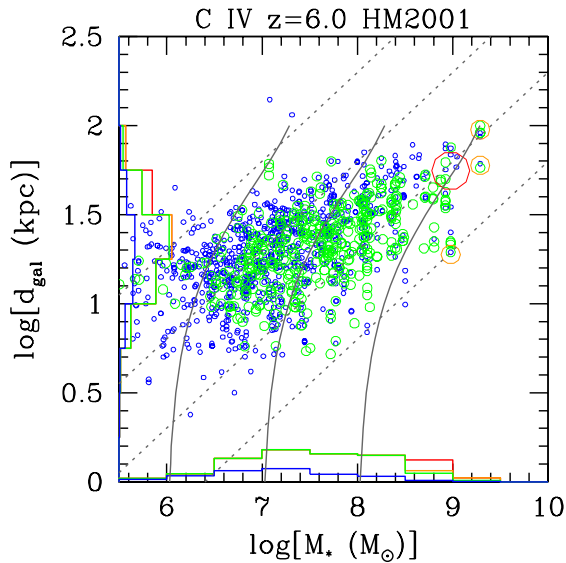


**Figure 22.** The galaxy-absorber plot for the uniform *HM2001* model, which is analogous to Figure 21 for the *Bubble* model. Here the gray dotted lines do not have any significance, but are shown for reference. Fewer strong absorbers exist near galaxies and more weak absorbers exist far from galaxies due to the weaker ionizing field in such environments. One important difference with the *Bubble* field is that strong absorbers are only associated with  $M_* \sim 10^9 M_\odot$  galaxies, and these absorbers trace enriched low-density regions further from galaxies. The color key for absorber strength in Figure 19 applies here.

### 6.3.2 Where Are The Weak $z = 6$ C IV Absorbers?

Both our backgrounds produce a significant amount of weak absorbers ( $N(\text{C IV}) = 10^{13.0-14.0} \text{ cm}^{-2}$ ), contributing non-trivially to  $\Omega(\text{C IV})$  (30% in the *Bubble* case and 70% in the *HM2001* case). The two observational  $z = 6$  C IV CDD constraints shown in Figure 10 (bottom right) suggest a possibly shallower distribution than either of our models produce, with the C IV mass density coming almost exclusively from strong systems. The Becker et al. (2009) data point is a conservative upper limit, and already provides a powerful constraint that we interpret as indicating a significant volume of the IGM is not enriched far above  $Z = 10^{-3} Z_\odot$ . However, if we consider that they observe no C IV absorbers between  $N(\text{C IV}) = 10^{13.5-14.0} \text{ cm}^{-2}$  and assume their completeness is 75% over this column density range (this seems reasonably conservative using their Figure 3), the difference with our models is even more stark. We predict 3.3 and 3.9 such absorbers should be detected at  $z = 5.65$  for the *Bubble* and *HM2001* fields respectively over the Becker et al. (2009) adjusted pathlength of  $\Delta z = 1.65$ .

A possible explanation is that the small galaxies in our simulation do not produce C IV absorbers for some reason. The evolutionary tracks in Figure 21 can be used as a stellar mass cut for which galaxies produce C IV systems. For example, if the originating  $M_*$  must be  $\geq 10^7 M_\odot$ , then only absorbers right of the middle evolutionary track contribute. Systems below  $N(\text{C IV}) = 10^{14} \text{ cm}^{-2}$  are more than halved, while leaving the stronger end unaffected if applying this cut. The power law slope now approaches  $\alpha = -1$  (i.e. equal numbers of absorbers in low and high density CDD bins).

Why would low-mass haloes not produce C IV ab-

sorbers? A possible explanation is that the highly mass-loaded outflows from small galaxies self-shield metals leading to them being observed in lower ionization states. Thus the over-excess of C IV absorbers and  $\Omega(\text{C IV})$  in either ionization background may be counter-balanced by the BSRS low-ionization systems, which are underestimated when applying these backgrounds to all metals.

A second possibility for us overestimating weak C IV absorbers is that our outflows are traveling too far into the IGM. For example, there exist few very weak,  $N(\text{C IV}) < 10^{13} \text{ cm}^{-2}$ , absorbers around galaxies  $M_* > 10^8 M_\odot$  in Figure 21 because winds have not had time to enrich regions at  $d_{gal} \gtrsim 100 \text{ kpc}$ . If wind speeds are even lower, metals will populate less of the  $M_* - d_{gal}$  phase space at large  $d_{gal}$ , where they otherwise would produce weaker C IV absorbers.

Our discussion in this section on the galaxy-absorber connection may be currently inaccessible to observations and somewhat speculative, as only a handful of absorbers at  $z \sim 6$  are known thus far and identifying the nearest galaxy may have to await a next-generation facility. Our purpose is to emphasize the  $M_* - d_{gal}$  relation as the key one for understanding the origin and subsequent evolution of high- $z$  metal-line absorbers. As these early galaxies push a majority of their metals into the IGM, the metals are still close enough that the high- $z$  galaxy-absorber connection tightly establishes the absorber properties. This is a fundamental prediction of our model, and if proved correct, offers a novel way to probe feedback processes in the reionization epoch.

### 6.4 Low Ionization Species

We now examine the physical conditions of C II absorbers, as a representative of lower ionization species. In §4.2 we showed C II traces higher overdensities closer to galaxies; therefore we might expect this species to trace metal-enriched outflows at an earlier stage. This turns out to be only partially true. In Figure 23 we plot C II absorbers in  $\rho - T$  phase space demonstrating that C II absorbers do not trace the same extent of this phase space as C IV. Our visualization in Figure 5 shows C II tracing less volume than C IV. Another difference is there is a stronger correlation with density for C II, much more so than for C IV. The reason for this is that the C II ionization fraction falls off rapidly toward lower overdensities as shown in Figure 7 while the C IV ionization fraction peaks at overdensities corresponding to intergalactic metals. C II absorption strength depends much more on the physical state (density) than C IV, which depends more on its environmental state (proximity to and mass & metallicity of its parent galaxy). The ionization field has little effect here, because density is the primary determinant for C II.

C II tracing higher overdensities translates into this species tracing regions closer to the launch galaxy, as the range in  $d_{gal}$  in Figure 23 is less than that for C IV.  $\Omega(\text{C II})$  arises from absorbers at the same ages traced by the C IV absorbers (compare y-axis histograms in the center panel of Figure 23 and bottom left panel of 19). C II is tracing older metals that remain closer to their parent galaxies by virtue of either lower  $v_{wind}$  or more hydrodynamic slowing. The primary reason is the lower  $v_{wind}$ : the average  $v_{wind}$  of a C II absorber is  $150 \text{ km s}^{-1}$  versus  $250 \text{ km s}^{-1}$ , while the  $v_{eff}/v_{wind}$  ratio is not different than that for C IV; Hence C II

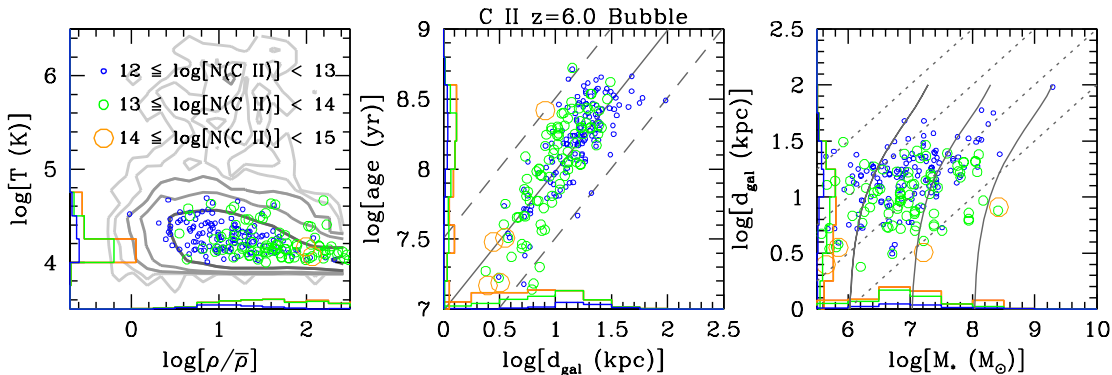


**Figure 23.** Physical conditions of C II absorbers at  $z = 6$ ; compare to corresponding panels for C IV in Figure 19 and Figure 21. C II is more dependent on density than C IV due to rapidly rising ionization fractions at higher densities. C II absorbers are more apt to trace metals immediately outflowing from galaxies, as well as the outflows that slow and stall closer to galaxies. Stronger C II absorbers are found closer to galaxies, and originate from galaxies having on average  $\times 10$  less stellar mass than that for C IV absorbers.

is arising from slower winds around less massive galaxies. Despite C II tracing a different set of winds, 62% of C II absorbers over  $50 \text{ m}\text{\AA}$  are aligned with C IV in the *Bubble* field. Rare strong C II absorbers trace some of the youngest outflows ( $10 - 30 \text{ Myrs}$ ), which are sometimes still within the galactic halos of  $z = 6$  galaxies.

In the right panel of Figure 23, C II strength is determined more plainly by  $d_{gal}$  independent of  $M_*$ , which is a result of this ion’s greater dependence on density compared to C IV. The galaxy-absorber connection is *not* as important for C II absorber strength. If  $N(\text{C II})$  is mostly independent of  $M_*$ , the selection effects of LOSs probing a random volume finds the average C II absorber around a smaller galaxy. The median  $M_*$  of the  $\Sigma N(\text{C II})$  histogram in the bottom of this panel is  $10^{6.9} M_\odot$ , corresponding to a SFR of  $0.03 M_\odot \text{yr}^{-1}$ . C II is probing a different set of metals than C IV, which itself is tracing faster winds arising from more massive galaxies ( $10^{7.9} M_\odot$ ) enriching a larger volume.

### 6.5 Evolution to $z = 8$

We are already delving into the hypothetical here by considering the physical and environmental parameters of absorbers and galaxies not even discovered yet, so we take it one step further by considering what C IV absorbers trace at  $z = 8$ . If our suggestion that C IV absorbers are tracing metals on their first journey into the IGM, metals should be observed even closer to galaxies at higher redshift. This indeed is the case in Figure 24 for  $z = 8$  absorbers; the absorbers occupy slightly higher overdensity (left panel) than at  $z = 6$  due to winds not reaching mean overdensities yet, while absorbers are closer to their parent galaxies as a consequence of having less time to travel (middle panel). These absorbers have  $v_{\text{eff}}$  more similar to  $v_{\text{wind}}$  signifying these outflows are just leaving their galaxy. In fact, the ratio  $v_{\text{eff}}/v_{\text{wind}}$  for the absorbers between with  $N(\text{C IV}) = 10^{13.5-14.5} \text{ cm}^{-2}$  for  $d_{gal} = 10 - 20 \text{ kpc}$  is 0.73 at  $z = 8$  versus 0.62 at  $z = 6$ . Such absorbers at  $z = 8$  trace outflowing gas more directly, whereas at  $z = 6$  some absorbers at this distance trace outflows that have already stalled or are returning to galaxies.

The right panel displays our galaxy-absorber connection plot with dotted lines corresponding to constant *Bubble* ionization flux, while gray lines are evolutionary tracks

assuming  $v_{\text{eff}} = 200 \text{ km s}^{-1}$  and the SFR is doubled from Equation 4 as in DFO6 at  $z = 8$  versus  $z = 6$ . The more rapid assembly of galaxies at this epoch is noticeable by greater curvature in these evolutionary tracks; more galactic evolution likely has occurred in an absorber’s associated galaxy despite the younger age of the Universe. The mass-metallicity holds at this redshift (DFO6) and appears to play a role in the increasing  $N(\text{C IV})$  for more massive galaxies.

## 7 SUMMARY

We explore high redshift metal-line absorbers using a state-of-the-art,  $2 \times 512^3$  particle GADGET-2 cosmological simulation enriching the IGM with star formation-driven galactic outflows. Our galactic outflows follow the predicted relations of momentum-driven winds, where outflow velocity scales with galaxy velocity dispersion and the mass loading factor scales inversely, leading to higher mass loading from small galaxies. Our purpose is to reproduce IGM metal-line observations at  $z \sim 5 - 6$  while providing predictions for future observations out to  $z = 8$ , as well as to investigate the physical nature of high- $z$  metal absorbers and its connection to galaxies. We explore five species (C II, C IV, O I, Si II, & Si IV) using three different ionizing backgrounds: fully neutral, fully reionized, and a patchy bubble model based on the flux of the nearest galaxy. Our key results and predictions are as follows:

(i) Metal lines already discovered at  $z > 5$  are primarily tracing the diffuse IGM, not gas in galaxies. Some C IV lines already discovered could be tracing metals at overdensities not much higher than the mean density of the Universe.

(ii) We can reproduce the observed trends of  $\Omega(\text{C IV})$  at  $z \sim 6 \rightarrow 4.5$  with steady enrichment of the IGM filling only 1% of the IGM with metals by  $z = 5$ . The recent samples of Becker et al. (2009) and Ryan-Weber et al. (2009) that find lower  $\Omega(\text{C IV})$ s suggests that the filling factor could be even less. We also propose that patchy ionization conditions where some metals are ionized by their local galaxy and others are not ionized may best explain the observed trends in both C IV and lower ionization absorbers. The determina-

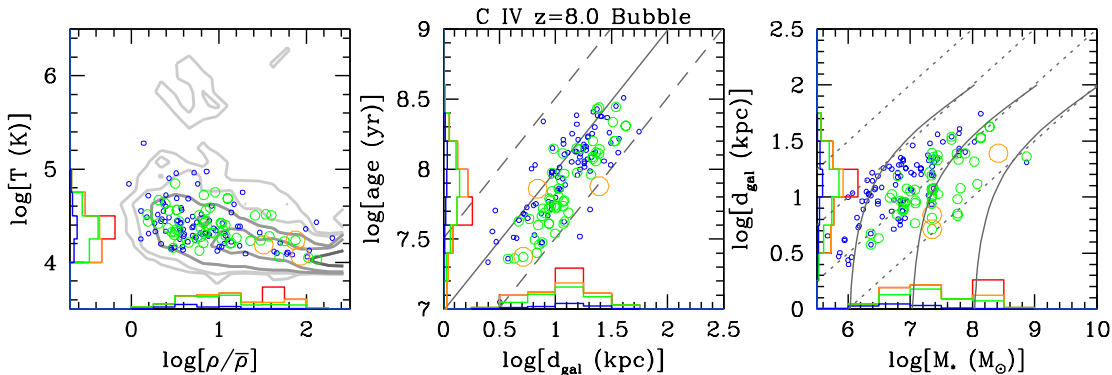


**Figure 24.** Similar to Figure 23, but for C IV at  $z = 8$ . The color key for absorber strength from Figure 19 applies here. See previous figure captions for an explanation of all contours and lines. We modify the evolutionary tracks in the right panel to reflect  $v_{\text{eff}} = 200 \text{ km s}^{-1}$  and double the SFR from Equation 4 reflecting galaxy evolution as found in DFO06. Absorbers still trace the location of metals well in this *Bubble* model, as shown by the overlap with metal contours in the  $\rho - T$  phase space of the left panel. The calculated  $v_{\text{eff}}$  is higher on average in the central panel than at  $z = 6$ . The evolutionary tracks in the right panel indicate that stronger absorbers arise from more massive galaxies, as at  $z = 6$ .

tion of  $\Omega(\text{C IV})$  is also highly dependent on the shape of the ionizing field (especially above 47.9 eV), SNe yields, the  $\sigma_8$  parameter, and the number of  $N(\text{C IV}) < 10^{14} \text{ cm}^{-2}$  absorbers.

(iii) The global gas-phase metallicity increases by a factor of 9 from  $z = 8 \rightarrow 5$ . The evolution of  $\Omega(\text{C IV})$  generally reflects this change, but the exact amount of evolution depends on the form of the ionization background. The uniform Haardt & Madau (2001) evolving background results in an increase in  $\Omega(\text{C IV})$  of  $\times 91$ , while the *Bubble* field shows only a  $\times 14$  increase reflecting the actual increase in gas-phase metals. The greater ionization intensity around 47.9 eV in the latter background, which is a result of the dust attenuation law we apply along with the proximity of metals to galaxies, results in  $\times 8$  greater  $\Omega(\text{C IV})$  at  $z = 8$ .

(iv) C IV is the ideal tracer for metals at low overdensities at  $z = 6$ , and its detection holds the best option at high- $z$  to determine the volume filling factor of metals. C IV has the lowest global ionization correction at  $z \sim 5 - 6$  (i.e.  $\Omega(\text{C IV})/\Omega(\text{C})$  is at its maximum). Adding a metallicity floor of  $10^{-3} Z_{\odot}$  will have dramatic effects on the numbers of weak C IV absorbers, just below thresholds of currently published results. Integrating for several nights on a single bright  $z > 6$  quasar could determine if a significant portion of the IGM volume is enriched to this level. The results of Becker et al. (2009) already indicate that a significant volume of the IGM is unlikely to be enriched much above  $10^{-3} Z_{\odot}$ , and possibly there exists too many weak C IV absorbers in our model without this floor.

(v) The velocity profiles of systems are dominated by the peculiar velocities of outflowing gas. We reproduce the large  $\delta v$ 's ( $> 200 \text{ km s}^{-1}$ ) observed in strong O I and C IV systems. The Hubble expansion of spatially distributed metals alone is far too small to create these observed system profiles.

(vi) The galaxies responsible for the enrichment of the IGM have stellar masses in the range of  $10^{7.0-8.5} M_{\odot}$  and corresponding rest-frame UV magnitudes of  $-15.4$  and  $-18.9$  (1350 Å AB) when considering C IV, and a factor of ten less when considering C II. Most absorbers should still be near their originating galaxies (5-50 physical kpc for  $z = 6$

C IV and 2-20 kpc for C II absorbers). We stress the need to identify such galaxies, which will require the likes of JWST and 30-meter telescope facilities, in order to study the high- $z$  galaxy-absorber connection. Identifying the environments of strong C IV components ( $\geq 10^{14} \text{ cm}^{-2}$ ) can constrain the ionizing source: within 30 kpc of  $M_{*} = 10^{7.0-9.0} M_{\odot}$  galaxies for the *Bubble* field, and at  $\geq 30$  kpc around  $M_{*} \sim 10^9 M_{\odot}$  galaxies for the *HM2001* field.

(vii) The abundance of O I absorbers observed by Becker et al. (2006) in the SDSS J1148+5251 sight line is consistent with metals residing in a neutral IGM (as also argued by those authors). We cannot produce such a frequency of O I within our models with ionization extending above the Lyman limit. The excellent alignment with C II and Si II in this dataset also strongly supports this. The fact that most sight lines show much less O I suggests the possibility that reionization is still inhomogeneous over large scales at  $z \gtrsim 6$ . It is unlikely to be an effect of inhomogeneous enrichment, since smaller galaxies with relatively low clustering lengths are primarily responsible for enriching the IGM at these epochs. Another possibility for broad O I systems observed down to  $z = 5.3$  are metals entrained in outflows, which remain shielded from the ionization background as they travel into the IGM.

(viii) Aligned absorber ratios are a powerful tool to determine the physical parameters of the metal-enriched IGM and the nature of the ionization field. Aligned absorbers with both components above 50 mÅ are rare at  $z = 6$ , unless the IGM is neutral. This makes the Becker et al. (2006) finding of frequent low-ionization aligned absorbers all the more supportive of either a neutral (probably recombined) portion of the IGM, or metals entrained in self-shielded outflows as they travel into the IGM.

Our analysis in OD08 indicated that most metals injected into the IGM recycle back into galaxies on a typical timescale of 1 – 2 Gyrs. Hence at  $z > 5$ , metals should primarily be on the outward leg of their first journey into the IGM. This indeed turns out to be the case when we look in detail at the evolutionary state of absorbers. This has consequences for the galaxy-absorber connection, in that this

relationship is closest at high- $z$  because metals are still in relatively close proximity of their parent galaxies. Absorbers trace gas on an outward trajectory still holding signatures of their galactic outflow origin, while possibly being primarily irradiated by their parent galaxy’s radiation field. The properties of C IV absorbers depend most on their evolutionary relation to their parent galaxy (proximity, mass, & metallicity), while lower ionization species depend more on the physical state of the gas (density, primarily). This is a result of the different  $\rho-T$  phase space traced by these ions.

Another tenet of OD08 is that metals travel a relatively constant physical distance ( $\sim 100$  kpc) from their parent galaxies, meaning early outflows have the greatest chance of enriching a large volume of the Universe. However this journey takes significant time as wind outflows travel at an average of  $\sim 100$  km s $^{-1}$  taking  $\sim 1$  Gyr to get to this distance, or more than the age of any stars at  $z = 6$ . Therefore, the volume of the Universe enriched to significant levels (i.e. 0.01-0.1  $Z_{\odot}$ ) grows by an order of magnitude over the relatively brief time (575 Myr) covered between  $z = 8 \rightarrow 5$ . This era can be called the “Age of Volume Enrichment.” However metals do not exhibit the expansionist zeal of the Mongol Empire when it comes to enriching the IGM; the vast majority of the IGM (as much as 90%) still remains unenriched in our simulations run to  $z = 0$  (Oppenheimer & Davé 2009).

The outlook for the study of very high- $z$  metal lines in the IGM looks promising as long as sources (quasars and GRBs) are discovered to provide light bulbs for the near-IR spectrometers that will be on-line in the near future. Relatively low resolution and  $S/N$  observations can provide key constraints as to the filling factors of metals, the velocities and mass loading factors of the winds that put the metals there, and of course the ionization state of the IGM. In contrast to metal lines between  $z = 5 \rightarrow 2$ , we expect significant evolution in metal-line properties between  $z = 8 \rightarrow 5$ , a prediction that may have already been observed by Becker et al. (2009) and Ryan-Weber et al. (2009). Further down the line is the study of the intriguing high- $z$  galaxy-absorber connection, as this relation is closer than at lower redshift. The JWST and 20-30 meter class telescopes are required to study this realm as galaxies at  $M_* < 10^8 M_{\odot}$  with SFRs below  $0.5 M_{\odot}\text{yr}^{-1}$ , which are primarily responsible for most IGM metal lines at  $z \geq 6$ . To sum it all up, absorption line spectroscopy applied to the early Universe should yield significant insights into early galaxy formation, and whether such galaxies enrich the IGM in a manner similar to lower redshift systems, or in some exotic fashions not considered here. We suspect the former.

## ACKNOWLEDGMENTS

Very useful and encouraging conversations with George Becker, Max Pettini, Emma Ryan-Weber, and Rob Simcoe were fundamental to this paper. We also thank them for reading over this paper and providing important improvements. We much appreciate the referee’s comments, which added significantly to the paper. We additionally thank Karl Gordon, David Fanning, and Berkeley Zych. The simulations were run on the Intel 64 Linux Cluster Abe Supercluster at the National Center for Supercomputing Applications. The authors thank R. Kennicutt for gracious hospitality at

the Institute of Astronomy in Cambridge, England where much of the work on this paper was done. Support for this work was provided by NASA through grant number HST-AR-10946 from the SPACE TELESCOPE SCIENCE INSTITUTE, which is operated by AURA, Inc. under NASA contract NAS5-26555. Support for this work, part of the Spitzer Space Telescope Theoretical Research Program, was also provided by NASA through a contract issued by the Jet Propulsion Laboratory, California Institute of Technology under a contract with NASA. Support was also provided by the National Science Foundation through grant number DMS-0619881.

## REFERENCES

- Abel, T., Bryan, G. L., & Norman, M. L., 2002, *Science*, 295, 93
- Adelberger, K. L., Steidel, C. C., Shapley, A. E., & Pettini, M. 2003, *ApJ*, 584, 45
- Adelberger K. L., Shapley A. E., Steidel C. C., Pettini M., Erb D. K., & Reddy N. A. 2005, *ApJ*, 629, 636
- Aguirre A., Schaye J., Kim T., Theuns T., Rauch M., & Sargent W. L. W., 2004, *ApJ*, 602
- Aguirre, A., Dow-Hygelund, C., Schaye, J., & Theuns, T. 2008, submitted to *ApJ*
- Asplund M., Grevesse N., & Sauval A. J., 2005, in Barnes T. G. III, Bash F. N., eds, *ASP Conf. Ser. Vol. 336. Cosmic Abundances as Records of Stellar Evolution and Nucleosynthesis*. Astron. Soc. Pac., San Francisco , p. 25
- Barth, A. J., Martini, P., Nelson, C. H., & Ho, L. C. 2003, *ApJ*, 594, L95
- Becker. G. D., Sargent, W. L. W., Rauch, M., & Simcoe, R. 2006, *ApJ*, 640, 69 (BSRS)
- Becker G. D., Rauch M., & Sargent W. L. W. 2007, *ApJ*, 662, 72
- Becker G. D., Rauch M., & Sargent W. L. W. 2009, *astro-ph/0812.2856*, submitted to *ApJ*
- Bouwens R., Illingworth G., Blakeslee J., & Franx M., 2006, *ApJ*, 653, 53
- Bouwens, R. J., Illingworth, G. D., Franx, M., & Ford, H. 2007, *ApJ*, 670, 928
- Bouwens, R. J., Illingworth, G. D., Franx, M., & Ford, H. 2008, *ApJ*, 686, 230
- Bromm V. & Larson R. B. 2004, *ARA&A*, 42, 79
- Bruzual, G. & Charlot, S. 2003, *MNRAS*, 344, 1000
- Bunker, A. J., Stanway, E. R., Ellis, R. S., McMahon, R. G. 2004, *MNRAS*, 355, 374
- Calzetti, D., Armus, L., Bohlin, R. C., Kinney, A. L., Koornneef, J., & Storchi-Bergmann, T. 2000, *ApJ*, 533, 682
- Cen, R., Nagamine, K., & Ostriker, J. P. 2005, *ApJ*, 635, 86
- Cen, R. & Riquelme, M. A. 2008, *ApJ*, 674, 644
- Chabrier G., 2003, *PASP*, 115, 763
- Chieffi, A. & Limongi, M. 2004, *ApJ*, 608, 405
- Dalla Vecchia, C. & Schaye, J. 2008, *MNRAS*, 387, 1431
- Davé, R., Hernquist, L., Weinberg, D. H., & Katz, N. 1997, *ApJ*, 477, 21
- Davé, R., Finlator, K., & Oppenheimer, B. D. 2006, *MNRAS*, 370, 273 (DFO06)
- Davé, R. & Oppenheimer, B. D. 2006, *MNRAS*, 374, 427

- Davé, R. 2008, MNRAS, 385, 147
- Davé, R., Oppenheimer, B. D., & Sivanandam, S. 2008, MNRAS, submitted
- Dickinson, M., et al. 2004, ApJ, 600, L99
- Eikenberry, S., et al. 2006, SPIE, 6269, 188
- Fan, X., et al. 2001, AJ, 122, 2833
- Fan, X., Narayanan, V. K., Strauss, M. A., White, R. L., Becker, R. H., Pentericci, L., & Rix, H.-W. 2002, AJ, 123, 1247
- Fan, X., et al. 2001, AJ, 125, 1649
- Fan, X., et al. 2006, AJ, 132, 117
- Ferland, G. J., Korista, K. T., Verner, D. A., Ferguson, J. W., Kingdon, J. B., & Verner, E. M. 1998, PASP, 110, 761
- Finlator, K., Davé, R., Papovich, C., & Hernquist, L. 2006, ApJ, 639, 672
- Finlator, K., Davé, R., & Oppenheimer, B. D. 2007, MNRAS, 376, 1861
- Finlator, K. & Davé, R. 2008, MNRAS, 385, 2181
- Finlator, K. Ozel, F., & Davé, R. 2008, astro-ph/arXiv:0808:3578, submitted to MNRAS
- Finlator, K. Ozel, F., Davé, R., & Oppenheimer, B. D. 2009, to be submitted to MNRAS
- Fontana, A., Poli, F., Menci, N., Nonino, M., Giallongo, E., Cristiani, S., & D'Odorico, S. 2003, ApJ, 587, 544
- Fujita, A., Martin, C. L., Mac Low, M.-M., New, K. C. B., & Weaver, R. 2008, astro-ph/arXiv:0803.2892, submitted to ApJ
- Furlanetto, S. R. & Loeb, A. 2003, ApJ, 588, 18
- Furlanetto, S. & Oh, P. 2005, MNRAS, 363, 1031
- Gnedin, N. Y. 2000, ApJ, 535, 530
- Greif, T. H., Johnson, J. L., Bromm, V., & Klessen, R. S. 2007, ApJ, 670, 1
- Gunn, J. E. & Peterson, B. A. 1965, ApJ, 142, 1633
- Haardt, F. & Madau, P. 2001, in "Clusters of galaxies and the high redshift universe observed in X-rays, Recent results of XMM-Newton and Chandra", XXXVIth Rencontres de Moriond, eds. D.M. Neumann & J.T.T. Van.
- Heger, A. & Woosley, S. E. 2002, ApJ, 567, 532
- Heger, A. & Woosley, S. E. 2008, submitted to ApJ
- Hinshaw, G. 2008 astro-ph/arXiv0803.0732
- Hirschi, R. 2007, A&A, 461, 571
- Hopkins, A. M. 2004, ApJ, 615, 209
- Iliev, I. T., Mellema, G., Pen, U.-L., Merz, H., Shapiro, P. R., & Alvarez, M. A. 2006, MNRAS, 369, 1625
- Iliev, I. T., Mellema, G., Shapiro, P. R., & Pen, U.-L. 2007, MNRAS, 376, 534
- Kawai N. et al., 2006, Nat, 440, 184
- Kennicutt, R. C. 1998, ApJ, 498, 541
- Kereš, D., Katz, N., Weinberg, D. H., & Davé, R. 2005, MNRAS, 363, 2
- Kereš, D., Katz, N., Fardal, M., Davé, R., & Weinberg, D. H. 2008, astro-ph/arXiv0809.1430, submitted to MNRAS
- Kim, S. et al., 2008, astro-ph/arXiv:0805.1412, submitted to ApJ
- Kneib, J.-P., Ellis, R. S., Santos, M. R., & Richard, J. 2004, ApJ, 568, L75
- Lidz, A., McQuinn, M., Zaldarriaga, M., Hernquist, L. & Dutta, S. 2007, ApJ 670, 39
- Madau, P., Ferrara, A., & Rees, M. J. 2001, ApJ, 555, 92
- Madau, P. & Haardt, F. 2009, astro-ph/arXiv:0812.0824, submitted to ApJ
- Martin, C. L. 2005a, ApJ, 621, 227
- Martin, C. L. 2005b, in ASP Conf. Ser. 331, Extra-Planar Gas, ed. R. Brown (San Francisco: ASP), 305
- Mo, H. J., Mao, S., & White, S. D. M. 1998, MNRAS, 295, 319
- Murray, N., Quatert, E., & Thompson, T. A. 2005, ApJ, 618, 569
- Navarro, J. F., Frenk, C. S., & White, S. D. M. 1997, ApJ, 490, 493
- Oh, S. P. 2002, MNRAS, 336, 1021
- Oppenheimer, B. D. & Davé, R. A. 2006, MNRAS, 373, 1265 (OD06)
- Oppenheimer, B. D., Davé, R., & Finlator, K. 2007 EAS, 24, 157
- Oppenheimer, B. D. & Davé, R. A. 2008, MNRAS, 387, 587 (OD08)
- Oppenheimer, B. D. & Davé, R. A. 2009, submitted to MNRAS
- Osterbrock, D. E. 1989, Astrophysics of Gaseous Nebulae and Active Galactic Nuclei. University Science Books, Mill Valley, p. 42
- Pettini M., Shapley A. E., Steidel C. C., Cuby J.-G., Dickinson M., Moorwood A. F. M., Adelberger K. L., & Giallongo M. 2001, ApJ, 554, 981
- Pettini, M., Madau, P., Bolte, M., Prochaska, J. X., Ellison, S. L., & Fan, X. 2003, ApJ, 594, 695
- Porciani, C. & Madau, P. 2005, ApJ, 625, L43
- Portinari, L., Chiosi, C., & Bressan, A. 1998, A&A, 334, 505
- Rauch, M., Sargent, W. L. W., & Barlow, T. A. 2001, ApJ, 554, 823
- Rupke, D. S., Veilleux, S., & Sanders, D. B. 2005, ApJS, 160, 115
- Ryan-Weber, E. V., Pettini, M., & Madau, P. 2006, MNRAS, 371, L78
- Ryan-Weber, E. V., Pettini, M., Madau, P., & Zych, B. 2009, astro-ph/arXiv:0902.1991, accepted to MNRAS
- Scannapieco, E., Ferrara, A., & Madau, P. 2002, ApJ, 574, 590
- Schaye, J., Aguirre, A., Kim, T.-S., Theuns, T., Rauch, M., & Sargent, W.L.W. 2003, ApJ, 596, 768
- Shapley, A. E., Steidel, C. C., Pettini, M., & Adelberger, K. L. 2003, ApJ, 588, 65
- Shapley A. E., Steidel C. C., Pettini M., Adelberger K. L., & Erb D. K., 2006, ApJ, 651, 688
- Simcoe, R. A., Sargent, W. L. W., & Rauch, M. 2004, ApJ, 578, 737
- Simcoe, R. A. 2006, ApJ, 653, 977
- Songaila, A. 2001, ApJ, 561, L153
- Songaila, A. 2005, AJ, 130, 1996
- Springel, V. & Hernquist, L. 2003, MNRAS, 339, 289
- Springel, V. & Hernquist, L. 2003, MNRAS, 339, 312
- Springel, V. 2005, MNRAS, 364, 1105
- Storrie-Lombardi, L. J., McMahon, R. G., & Irwin, M. J. 1996, MNRAS, 283, L79
- Strickland, D. K., Heckman, T. M., Weaver, K. A., Hoopes, C. G., & Dahlem, M. 2002, ApJ, 568, 689
- Tegmark, M. et al., 2004, Phys. Rev. D, 69, 103501
- Thom, C. & Chen, H.-W. 2008a, submitted to ApJ
- Thompson, R. I., Eisenstein, D., Fan, X., Dickinson, M., Illingworth, G., Kennicutt, R. C. 2006, ApJ, 647, 787
- Thou A. A. & Weinberg D. H. 1996, ApJ, 465, 608

- Tornatore, L., Ferrara, A., Schneider, R. 2007, MNRAS, 382, 945
- Tripp, T. M., Sembach, K. R., Bowen, D. V., Savage, B. D., Jenkins, E. B., Lehner, N., & Richter, P. 2008, ApJ, accepted to ApJS
- Tumlinson, J. 2006, ApJ, 641, 1
- Vijh, U. P., Witt A. N., & Gordon K. D. 2003, ApJ, 587, 533
- Weingartner, J. C., & Draine, B. T. 2001, ApJ, 548, 296
- Wise, J. H. & Abel, T. 2008, ApJ, 685, 40
- Woodsley, S. E. & Weaver, T. A. 1995, ApJS, 101, 181
- Wright, E. 2006, PASP, 118, 1711
- Yan, H., & Windhorst, R. A. 2004, ApJ, 612, L93